Experimental quantum non-Gaussian mechanical states of a trapped ion

Ph.D. thesis

by

Lukáš Podhora

Palacký University Olomouc

2024

Title:	Experimental quantum non-Gaussian mechanical states of a trapped ion
Author:	Mgr. Lukáš Podhora
Supervisor	prof. Mgr. Radim Filip, Ph. D.
Advisor:	Mgr. Lukáš Slodička, Ph. D.
Study programme:	Optics and Optoelectronics
Institution:	Department of Optics, Faculty of Science, Palacký University
Year:	2024
Pages:	121

Abstract

A single trapped ion has proved to be one of the most convenient physical systems to realize and experimentally control the quantum bit, which is implemented as a superposition of a two-level system between two distinct energy levels. Additionally, the perfect isolation from surrounding environment of a single ion in a Paul trap placed in vacuum chamber provides a way to experimentally realize the harmonic oscillator level scheme. Together, these two physical systems allow for experimental realization of Jaynes-Cummings and anti-Jaynes-Cummings interactions, which provide a deterministic control over the motional degree of freedom in means of atom-light interaction. Such experimental systems have already been proven useful for enhanced quantum sensing, quantum computation, quantum communication and other areas of recent scientific interest.

This thesis summarizes our experimental work devoted to generation and control over the non-classical quantum states of motion. The discrete building blocks of such states are the number states with exactly defined amount of energy. In the first presented experiment, we realize a generation of number states, with a main focus on characterization of their non-classical properties with respect to the controllable amount of added thermal energy. The crucial concept implemented to states' characterization is a 'quantum non-Gaussianity', which sets the limit on states achievable by application of any combination of coherent displacement or squeezing on a ground state. The results uncover that even for the sufficiently high amount of added thermal noise the crucial quantum non-Gaussian features are preserved, and such states can provide a significant enhancement of metrological sensitivity.

Additional two experiments present a novel method of non-classical states generation which takes advantage of the increasing initial thermal energy. The heart of the generation process lies in the repetitive application of Jaynes, or anti-Jaynes-Cummings interactions to the initial thermal state. The motional population eventually converges towards the determined mixture of discrete energy levels, a process which we denote as an 'accumulation'. By evaluation of criteria of non-classicality and quantum non-Gaussianity, we prove that the overall amount of the non-classical aspects in resulting states is clearly enhanced by the repetition of the deterministic interaction process and also by increasing energy of the initial thermal distribution.

Keywords: quantum state, quantum non-classicality and non-Gaussianity, Jaynes-Cummings and anti-Jaynes-Cummings interaction, trapped ion, mechanical oscillator

Název:	Experimentální kvantově ne-Gaussovské stavy chyceného iontu
Autor:	Mgr. Lukáš Podhora
Vedoucí práce:	prof. Mgr. Radim Filip, Ph. D.
Konzultant:	Mgr. Lukáš Slodička, Ph. D.
Studijní program:	Optika a Optoelektronika
Instituce:	Katedra optiky, Přírodovědecká fakulta, Univerzita Palackého v Olomouci
Rok:	2024
Počet stran:	121

Anotace

Jednotlivé atomy držené v Paulově pasti patří k nejvhodnějších fyzikálních systémům pro experimentální kontrolu kvantového bitu, který je realizován jako superpozice dvouhladinového systému mezi dvěma rozdílnými energetickými hladinami. Dokonalá izolace atomu od okolního prostředí v Paulově pasti umístěné ve vakuové komoře umožňuje také realizovat hladinové schéma harmonického oscilátoru. Vzájemným provázáním pohybového stuplně volnosti a dvouhladinového systému vzniká možnost realizace Jaynes-Cummings a anti-Jaynes-Cummings interakcí, které poskytují deterministickou kontrolu pohybového stupně volnosti s využitím principů interakce záření a látky. Tyto experimentální interakce se ukazují jako užitečné pro vývoj kvantových sensorů, kvantovém počítání, komunikaci a v dalších oblastech souvisejícího výzkumu.

Tato disertace shrnuje naši experimentální práci věnovanou tvorbě a kontrole neklasických kvantových stavů pohybu. Základem těchto stavů jsou číselné stavy pohybu s přesně definovanou energií. V prvním z prezentovaných experimentů realizujeme generaci těchto číselných stavů a zaměřujeme se především na charakterizaci jejich neklasických vlastností v souvislosti s množstvím přidané tepelné energie. Klíčovým konceptem použitým k charakterizaci vytvořených stavů je ”kvantová ne-Gaussovost”, která určuje, jestli je možné dané pohybové stavy vytvořit pomocí kombinace koherentních operací nebo stlačení aplikovaných na základní stav. Výsledky experimentu ukazují, že i při výrazném množství přidaného tepelného šumu jsou klíčové ne-Gaussovské vlastnosti zachovány, a vytvořené stavy mohou poskytovat významné zvýšení metrologické citlivosti.

Další dva experimenty představují novou metodu generace neklasických stavů pohybu, která využívá počáteční termální energii vstupního stavu oscilátoru. Základním principem generace je opakovaná aplikace Jaynes nebo anti-Jaynes Cummings interakce na počáteční termální pohybový stav. Populace pohybových stavů směřuje k přesně dané směsi diskrétních energetických hladin, což je proces, který definujeme jako ”akumulace”. Výpočtem kritérií neklasičnosti a kvantové ne-Gaussovosti se podařilo dokázat, že celkové množství neklasických vlastností ve vytvořených stavech se zvyšuje s množstvím opakování interakce a také s rostoucí energií počátečního termálního stavu.

Klíčová slova: kvantový stav, kvantová neklasičnost a ne-Gaussovost, Jaynes-Cummings a anti-Jaynes-Cummings interakce, chycený ion, mechanický oscilátor

Acknowledgements

First and most of all, I want to thank Lukáš Slodička for almost ten years of our mutual collaboration during my Master's and Ph. D. studies. I am grateful for his guidance, patient mentorship, and for that he taught me all the experimental and theoretical methods to work in field of trapped ion quantum optics. I also appreciated our bike trips together, and our philosophical discussions during the laboratory work as well. Second, I thank Radim Filip for overseeing my Ph. D. studies, providing motivation and course to our published articles and teaching me lots about theoretical quantum physics.

I thank all the friends from our laboratory group in Brno. I thank Minh Tuan Pham for teaching me how to handle lasers and electronics in the lab, Adam Lešundák for experiments that we worked on together, Martin Čížek for handling and fixing the electronics and Daniel Babjak for measurements on fluorescence from ions that we did together.

I am grateful to my colleagues in Olomouc as well. Particularly, I want to thank Jaromír Mika for his continuous support, Petr Obšil, Dung Tran, Tomáš Lamich and Antonín Bekárek for collaboration on new trapped ion experiments in newly built laboratory in Olomouc. But most of all, I am grateful to Artem Kovalenko, who regularly traveled with me from Olomouc to Brno during the last year of my work, and helped me significantly to implement some of the presented experiments.

My thanks also belong to Barium team at university of Innsbruck, where I was privileged to spend a half year of my studies. Namely, I want to thank Gabriel Araneda and Giovanni Cerchiari for our cooperation in lab, Yves Colombe for theoretical discussions, prof. Rainer Blatt for giving me the opportunity to stay in his group, Vojtěch Krčmarský and Pavel Hrmo for friendly discussions and fun.

The greatest thanks belong to my wife Veronika, for her never ending support in all the difficulties, for her patience and for all the happy moments that we have lived together during the time of my studies. Thank You a lot!

I declare that I wrote this Thesis myself under the guidance of my supervisor prof. Radim Filip and my consultant dr. Lukáš Slodička. I declare that I personally performed all the presented experimental measurements at the trapped ion apparatus, which is located in the joined laboratory at Institute of Scientific Instruments, The Czech Academy of Sciences, Brno. Some text parts and figures for this Thesis were directly taken from our original published articles, where I contributed as a main author.

Olomouc
March 2024
Lukáš Podhora

List of publications with abstracts

Publications covering results in this Thesis:

L. PODHORA, L. LACHMAN, T. PHAM, A. LEŠUNDÁK, O. ČÍP, L. SLODIČKA, AND R. FILIP, *Quantum Non-Gaussianity of Multiphonon States of a Single Atom*, Phys. Rev. Lett. **129**, 013602 (2022).

Quantum non-Gaussian mechanical states are already required in a range of applications. The discrete building blocks of such states are the energy eigenstates—Fock states. Despite progress in their preparation, the remaining imperfections can still invisibly cause loss of the aspects critical for their applications. We derive and apply the most challenging hierarchy of quantum non-Gaussian criteria on the characterization of single trapped-ion oscillator mechanical Fock states with up to 10 phonons. We analyze the depth of these quantum non-Gaussian features under intrinsic mechanical heating and predict their requirement for reaching quantum advantage in the sensing of a mechanical force.

L. PODHORA, T. PHAM, A. LEŠUNDÁK, P. OBŠIL, M. ČÍŽEK, O. ČÍP, P. MAREK, L. SLODIČKA, R. FILIP, *Unconditional Accumulation of Nonclassicality in a Single-Atom Mechanical Oscillator*, Advanced Quantum Technologies **3**, 2000012 (2020).

The robust experimental accumulation of nonclassicality of motion of a single trapped ion is reported. The nonclassicality stems from deterministic incoherent modulation of thermal phonon number distribution implemented by a laser excitation of nonlinear coupling between the ion's internal—electronic levels and external—motional states. It is demonstrated that the repetitive application of this nonlinear process monotonically accumulates the observable state nonclassicality. The output states converge to a phonon number distribution with high overlap with a particular Fock state and visible quantum non-Gaussian aspects including corresponding negative Wigner function. The resulting oscillator states prove deterministic transition in the hierarchy of quantum non-Gaussianity up to four phonons. This transition is very robust against experimental imperfections and produces increasing entanglement potential.

Other publications in collaboration with ÚPT AVČR Brno:

A. KOVALENKO, D. BABJAK, A. LEŠUNDÁK, L. PODHORA, P. LACHMAN, P. OBŠIL, T. PHAM, O. ČÍP, R. FILIP, AND L. SLODIČKA, *Emergence of super-Poissonian light from indistinguishable single-photon emitters*, Optica **10**, 456-463 (2023).

P. OBŠIL, A. LEŠUNDÁK, T. PHAM, K. LAKHMANSKIY, L. PODHORA, M. ORAL, O. ČÍP, AND L. SLODIČKA, *A room-temperature ion trapping apparatus with hydrogen partial pressure below* 10^{-11} *mbar*, Review of Scientific Instruments **90**, 083201 (2019).

Publications based on results of internship in Innsbruck:

G. CERCHIARI, G. ARANEDA, L. PODHORA, L. SLODIČKA, Y. COLOMBE, AND R. BLATT, *Measuring Ion Oscillations at the Quantum Level with Fluorescence Light*, Phys. Rev. Lett. **127**, 063603 (2021).

G. CERCHIARI, G. ARANEDA, L. PODHORA, L. SLODIČKA, Y. COLOMBE, AND R. BLATT, *Motion analysis of a trapped ion chain by single photon self-interference*, Appl. Phys. Lett. **119**, 024003 (2021).

Articles based on Diploma Thesis research, published during my Ph.D. studies:

J. MIKA, L. PODHORA, L. LACHMAN, P. OBŠIL, J. HLOUŠEK, M. JEŽEK, R. FILIP AND L. SLODIČKA, *Generation of ideal thermal light in warm atomic vapor*, New J. Phys. **20**, 093002 (2018).

L. PODHORA, P. OBŠIL, I. STRAKA, M. JEŽEK, AND L. SLODIČKA, *Non-classical photon pairs from warm atomic vapor using a single driving laser*, Optics Express **25**, 31230-31238 (2017).

Contents

1. Introduction

The quantum mechanical treatment of light and matter, as we know it today, dates back to beginning of the 20^{th} century. In 1905, Albert Einstein described the experimentally observed photoelectric effect in means that the energy exchanges only in discrete packets, where the energy itself is quantized with frequency [1]. Later in 1926, Erwin Schrödinger came up with his description of wave mechanics, describing the quantum states as wave functions having certain amplitudes and phases, which may mutually interfere in constructive or destructive way [2]. Although his equation is well capable to describe some of the light-atom interactions at the single-atom level, Schrödinger himself assumed that the experimental control over single atom will never be experimentally feasible, as he once proclaimed that 'We never experiment with just one electron or atom or (small) molecule. In thought-experiments we sometimes assume that we do; this invariably entails ridiculous consequences...' (1952) [3]. Just one year later in 1953, Wolfgang Paul proposed the way to confinement of charged particles with use of the electric fields, today well known as a Paul trap [4] capable of trapping single charged atoms. A later advent of the laser technology (1958) [5] provided the narrow frequency light sources that made it possible to employ the light atom interactions. In 1978, the first laser cooling techniques were successively experimentally demonstrated [6, 7]. The first observation of a single barium ion in a radio-frequency Paul trap was then reported in 1980 [8].

Since then, the ability of controlling single ion system has hugely extended, finding the practical implementation in broad range of scientific areas. A significant advantage of the trapped ion quantum systems, with respect to other broadly employed platforms such as quantum dots [9], superconducting [10] or photonic qubits [11, 12], is a good isolation from the surrounding environment and thus the partial resistance to the decoherence effects. Narrow linewidths of transitions within the electronic level structure provide that the ion is well addressable with conventional laser technology, and allows for various ways of manipulation with the internal states. Last but not least, the electronic level structure, as well as other physical properties, remain fixed for each single atom of the corresponding isotope, which guarantees the mutual

indistinguishability of employed quibits, being a fundamental condition to create entangled quantum states [13, 14].

A list of broad application of trapped ion systems contains optical atomic clocks [15], quantum computation [16], simulation [17], communication [18] and also fundamental research [19]. This involves, for example, the engineering of motional quantum states in mutually coupled two-level system of the ionic electronic level structure, and the oscillatory normal mode of motion corresponding to the pseudo-potential originating from the external electric potentials at the electrodes of the Paul trap [19]. The basic interaction limit takes into account the fact, that after performing the laser cooling, the motional energy is efficiently subtracted to the regime where the quantized energy structure of the harmonic oscillator has to be taken into account. In such a case, we can investigate the probability of population for each energy level separately. The amount of residual thermal energy is often expressed as the equivalent of temperature, which typically reaches the scales of 10^{-3} K, which is close to the limit of absolute zero. The mechanical oscillator state of a trapped ion can be conveniently coupled with the ion's internal electronic levels [19], forming a joined Hilbert space where the motion can be detected and manipulated as a frequency modulation in the spectrum.

The term 'non-classical' state of motion in this work refers to the discrete energy distribution of motion incompatible with any mixture of displaced ground states of the oscillator [20]. We present several approaches where such nonclassicality can be controllably engineered with non-linear interactions. The 'quantum non-Gaussian' states represent the subclass of non-classical states that is beyond all mixtures of squeezed displaced oscillator ground states [21]. High quality quantum non-Gaussian states are in most experimental scenarios hard to prepare and observe. A well known property of a subclass of quantum non-Gaussian states is the negativity of the Wigner quasi-probability distribution function, however, it is not the necessary condition for the state to be non-Gaussian. In experiments considering single photons or the quantized motion in trapped atom, a specifically derived criteria can be conveniently used to characterize non-classical and non-Gaussian properties from the reconstructed population and detect them even in the presence of processes which destroy the negativity of Wigner function, such as losses or addition of thermal noise [22, 23].

Physically, the non-classical states of atomic motion can be employed in applications focused on experiments involving quantum metrology and quantum enhanced sensing [24–26], and quantum error correction [27–30]. It also finds it's applications in treating quantum engines [31, 32], or in simulation of many body interaction models and corresponding phase transitions [33].

The presented work focuses on engineering, measurement, and

characterization of non-classical and quantum non-Gaussian states of motion, implemented on the mode of motion of single $^{40}Ca^{+}$ ion held in a Paul trap. The non-classical properties of generated quantum states are evaluated from the measured distributions of motional populations. The presented results originate from three experiments, where two of them are already published in [34, 35], and the last measurement is currently being prepared for publication.

The outline of this work goes as following. Chapter 2 summarizes the basic physical principles of ion trapping and light matter interactions at the level of single trapped ion interacting with coherent light. In the Lamb-Dicke regime, the coupling is limited only on carrier interaction, red and blue sideband transitions, where the last two are denoted as Jaynes and anti-Jaynes Cummings interactions. We also present there the fundamental definitions of mechanical non-classical and quantum non-Gaussian states and possibilities of their unambiguous witnessing. Chapter 3 then focuses on methods of the experimental control, describing mainly laser cooling, motional engineering and motional state readout. Each of the following three chapters is then devoted to a single experiment involving the manipulation with ion's motion in order to create and characterize mechanical non-classical states. In particular, Chapter 4 is based on the results published in the reference [35]. The measurement focuses on generation of number states of motion and characterization of their quality with respect to losses caused by recoil heating and experimental imperfections. Chapter 5, based on the article [34], focuses on creation of non-classical statistical mixtures by repetitive anti-Jaynes interaction, where we demonstrate that the amount of non-classicality can be enhanced with initial thermal energy present in the system. Chapter 6 presents measurements which are implemented with use of Jaynes-Cummings interaction. We prove that the subtraction of the single quantum may lead to enhancement of non-classicality, which is also being driven with thermal energy. Together, these results implicate that the non-classical states may not always suffer from high temperatures, but they can actually, under certain circumstances, benefit from them.

2. Mechanics with a trapped ion oscillator

The basic physical principles of the presented experiments consider coupling between the internal two-level system of the ion's electronic energy level structure, and the motional quantum oscillator scheme, which is induced externally by the electric field trap potentials. In this Chapter, we present and discuss the basic theoretical concepts, which are necessary to understand and discuss the physics of the implemented experiments and measured results.

We begin with discussion of the $^{40}Ca^{+}$ ion (Sec. 2.1) and energy level scheme of relevant low-lying valence electron energy levels. (Sec. 2.2). Further, we shift towards description of two-level system and mechanical quantum harmonic oscillator scheme, including the Lamb-Dicke approximation relevant for the presented experimental regimes (Sec. 2.7). Finally, we include the basic definition of state's non-classicality and quantum non-Gaussianity, which is important for understanding of the realized states of trapped ion mechanics.

2.1 Physical properties of $^{40}Ca^{+}$ ion

Calcium is the species which is commonly used for experiments in ion trapping community. Other elements also used for trapping experiments are Be, Mg, Ca, Sr and Ba, where the basic differences between the species lie in increasing atomic mass and also decreasing frequency differences between the transitions. All of these chemical elements belong to the group of alkali-earth metals. Additional elements, commonly used for the experiments of the similar type and not belonging to the alkali-earth group, are Aluminum (Al), Indium (Id), and Ytterbium (Yb). Typically, these species are being advantageously employed in experiments implementing atomic optical clocks [36, 37].

A particular choice of the calcium species is justified by simple accessibility of the energy transitions with use of the conventional laser technology. Especially, the electronic level structure provides the narrow linewidth dipole-forbidden

transition in the range of visible spectrum at wavelength 729 nm, which is commonly being used for experiments in quantum metrology and quantum motional manipulations with light. On the other hand, in the implementations limited by photon recoil, the relatively small mass of calcium increases its probability.

Another beneficial feature of calcium is it's high attainability in nature. Calcium as a chemical species is the fifth most abundant element in Earth's crust, and the third most abundant metal at the same time [38]. Considering the stable isotopes, the $^{40}Ca^{+}$forms the most common one, reaching the 96.94 % abundance [39, 40]. Another stable isotope is $^{44}Ca^{+}$, with the occurrence among the other isotopes reaching 2.09 %. All the other stable isotopes, particularly $^{42}Ca^{+}$,$^{43}Ca^{+}$,$^{46}Ca^{+}$ and $^{48}Ca^{+}$ are populated with the probability less than 1 %.

Basic physical quantities related to $^{40}Ca^{+}$ are as following. The standard atomic mass is the 40.078(4) amu [39], the nuclear spin of this particular isotope is zero, and so the hyperfine splitting does not occur. Since the number of protons and neutrons is equal, the isotope is observationally stable [40].

2.2 Electronic level structure

The Fig. 2.1 presents all optical transitions within the lowest lying electronic states relevant for the experiments presented in this work. We employ dipole transitions at wavelengths $\lambda = 397$, 866 and 854 nm and a quadrupole transition at 729 nm. In the following Sec. 2.3, we briefly describe the principles of coupling on the dipole and quandrupole transitions.

In Table 2.1, we summarize the wavelengths and lifetimes of $^{40}Ca^{+}$energy level transitions, which we implement in our experiment. The presented data are taken from references [41–44], and the values in brackets correspond to their uncertainties.

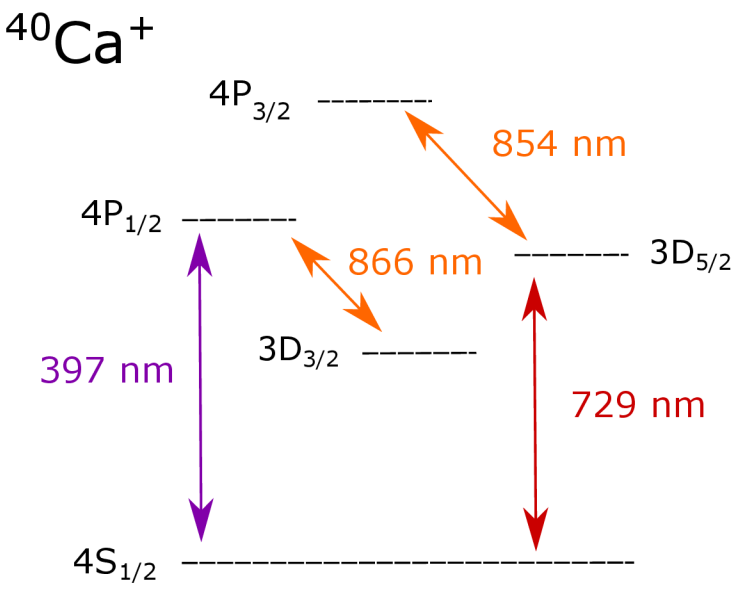

Figure 2.1: Energy level scheme of $^{40}Ca^{+}$ion, with transitions employed in the experiment. Transitions used for Doppler cooling (397 nm, 866 nm), qubit manipulation (729 nm) and population re-shuffling to ground state (854 nm). Exact values of wavelengths and also the lifetimes of energy levels are written in the Table 2.1 . Transitions at 397 nm, 866 nm and 854 nm are dipole transitions described with dipole vector d_e (Eq. 2.3) , and 729 nm is a quardupole transitions (Eq. 2.4).

2.3 Dipole and quadrupole transitions in $^{40}Ca^{+}$ atom

In order to describe the laser interaction with the atomic valence electron, we view the electronic transitions in terms of electric multipole expansion, which is in detail described for example in [45, 46]. The crucial part of the total interaction is the Hamiltonian describing the coupling between the atom and the electric field, denoted as H_{AE}. This can be expressed in terms of the electric field vector **E(r)** and the atomic polarization dipole vector **P(r)** as

$$H_{AE} = -\int d^3r \mathbf{P}^{\perp}(r) \cdot \mathbf{E}^{\perp}(r) + \frac{1}{2\epsilon_0}\int d^3r[\mathbf{P}^{\perp}(r)], \tag{2.1}$$

where $\mathbf{E}^{\perp}(r), \mathbf{P}^{\perp}(r)$ are transversal parts of the electric field and polarization vectors, and the center of mass of the system lies at point $r = 0$. The first term in Eq. 2.1 describes the mutual coupling with the atomic polarization density, and the second term describes the atomic self-energy from the polarization coupling

transition $\|e\rangle \rightarrow \|g\rangle$	dip/quad	λ (nm)	lifetime of $\|e\rangle$	transition rate (s^{-1})
$4P_{1/2} \rightarrow 4S_{1/2}$	dip	396.959(1)	6.904(26) ns	$1.3553(40) \cdot 10^8$
$4P_{1/2} \rightarrow 3D_{3/2}$	dip	866.452(5)	6.904(26)	$9.45(10) \cdot 10^6$
$4P_{3/2} \rightarrow 4S_{1/2}$	dip	393.478(1)	6.639(42) ns	$1.3923(41) \cdot 10^8$
$4P_{3/2} \rightarrow 3D_{3/2}$	dip	850.036(5)	6.639(42)	$9.834(36) \cdot 10^6$
$4P_{3/2} \rightarrow 3D_{5/2}$	dip	854.444(5)	6.639(42)	$8.752(32) \cdot 10^6$
$3D_{5/2} \rightarrow 4S_{1/2}$	quad	729.3478	1.163(11) s	0.8598(81)
$3D_{3/2} \rightarrow 4S_{1/2}$	quad	732.5905	1.194(11) s	0.8376(79)

Table 2.1: List of available transitions of $^{40}Ca^{+}$ ion in the energy level structure depicted in Fig. 2.1. The dipole transitions (dip) at 397 nm, 866 nm, 854 nm and quadrupole (quad) 729 nm transition are physically implemented in the experiments, while the other transitions at 393 nm, 850 nm and 732 nm are unused, and they are written here only to form a complete picture of transitions achievable within the experimental routine. Lifetime of the excited state defines the average time which it takes for an electron to spontaneously decay into the lower energy level which leads to a photon emission. Transition rate determines the probability of spontaneous emission at the particular transition.

to it's own field. The second self-interaction term in Eq. 2.1 can be omitted for further investigations, and the first term describing the atom-field interaction can be expanded with use of Taylor series. In this way, the Hamiltonian in the Eq. 2.1 can be expressed in the form of mutipole expansion as [45]

$$H_{AE} = -\mathbf{d}_\alpha E^\perp_\alpha(0) + \mathbf{Q}_{\alpha\beta}\partial_\alpha E^\perp_\beta(0) - \mathbf{O}_{\alpha\beta\gamma}\partial_\alpha\partial_\beta E^\perp_\gamma(0) + ... \tag{2.2}$$

where the terms denote dipole, quadrupole and octupole expansion elements, and d_α, $Q_{\alpha\beta}$ and $O_{\alpha\beta\gamma}$ are the corresponding moment vectors. The dipole moment

$$\mathbf{d}_\alpha = -e \cdot \mathbf{r}_{e,\alpha}, \tag{2.3}$$

defines the oscillation to be in linear axis denoted as α, proportional to the electric charge. The quadrupole moment can be expressed as a tensor in a form

$$\mathbf{Q}_{\alpha\beta} = -\frac{1}{2}e(\mathbf{r}_{e,\alpha} \cdot \mathbf{r}_{e,\beta} - \frac{\mathbf{r}_e^2}{3}\delta_{\alpha\beta}), \tag{2.4}$$

which also describes the oscillations in transversal directions denoted with vectors $\mathbf{r}_\alpha, \mathbf{r}_\beta$. For the considered transitions of the $^{40}Ca^{+}$ atom, the leading multipole terms are the dipole and quadrupole one, and the higher order parts of the Eq. 2.2 can be neglected.

In the lowest-order dipole interaction description, the incoming electromagnetic wave with the amplitude $E(r) = E_0 e^{kr-\omega t}$, with wavevector

k, maximal amplitude E_0 and the angular frequency ω drives the oscillation in the atomic electron, which has a charge e^- and the orientation $r_{e,\alpha}$. The oscillating dipole then decays through the emission of the single photon. In multilevel atoms, the polarization of the scattered photon is simultaneously dependent on the spatial orientation of the dipole and the polarization state of the incoming electromagnetic wave. The strength of the dipole interaction is directly proportional to the field amplitude, as described by the first term in Eq. 2.2. In the energy level scheme of the employed $^{40}Ca^+$ atom, all transitions except of the one at 729 nm can be described by the dipole approximation, because of the negligible contribution of the quadrupole and higher parts of the multipole expansion. The $3D_{5/2} \rightarrow 4S_{1/2}$ transition at 729 nm is denoted as quadrupole transition, because it has zero matrix elements of the dipole transition in the Eq. 2.36 (see Sec. 2.9) and the quadrupole term is the fist non-zero matrix element.

Fundamental difference between the dipole and quadrupole transition also lies in the excited state's lifetime, and consecutively the line width of the particular transitions and the overall experimental ability to achieve efficient atom-photon coupling. The average lifetimes of the employed transitions are written in Table 2.1. Due to the short lifetime of the excited level $4P_{1/2}$, which is in order of nanoseconds, transition at 397 nm becomes suitable for the fluorescence detection, and also the Doppler cooling routine, which is used to reduce the initial oscillation energy (see details in Sec 2.8). On the other hand, the slowly-decaying excited state of the $3D_{5/2} \rightarrow 4S_{1/2}$ quadrupole transition is suitable to realize the quantum bit and the coherent manipulations with mechanical states, as described in the following Sec. 2.4 and Sec. 2.10.

2.4 The two-level approximation

The two-level system approximation is an idealization of the electronic level structure, where only the single transition between two energy level is taken into account. The practical implementation in $^{40}Ca^+$atom can be approximated by considering particular Zeeman sub-level within the $4S_{1/2}$ ground state and the excited state $3D_{5/2}$. The fundamental condition to justify the two-level approximation is the frequency of the electromagnetic field inducing the interaction to be close to resonance, and that the corresponding Rabi frequency of the interaction is much smaller than detuning with respect to the neighboring off-resonant transitions.

We denote the ground state of the two-level system as $|g\rangle$ and the excited state as $|e\rangle$. In order to transfer the electron from $|g\rangle$ to $|e\rangle$, the energy has to be externally added into the system, while the opposite process can result

from spontaneous decay or stimulated transition back to the ground state. The spontaneous emission results in the emission with a statistics resembling that of ideal single photon state up to the attenuation, and the rate of its emission is corresponding to the parameter Γ. The system can also be driven in a coherent way, which requires the excited state lifetime and coherence of the interaction to be sufficient so that any interaction is not suppressed by the spontaneous emission. The two level system then exhibits a periodic development of the excited state population due to coupling to coherent light field, known as Rabi oscillation [19].

A coherently controlled two-level system can physically realize a quantum bit [47], however, in this work it rather corresponds to an internal atomic knob for control of its mechanical properties. The state vector of the two level system can be defined as

$$|\psi\rangle = \alpha\,|g\rangle + \beta\,|e\rangle\,, \tag{2.5}$$

denoting a superposition of the two base states $|g\rangle$ and $|e\rangle$, which represents the ground and excited energy levels. Here α, β are the probability amplitudes, satisfying the condition $|\alpha|^2 + |\beta|^2 = 1$. The corresponding two-level system Hamiltonian is defined as [19]

$$H^{(e)} = \hbar\frac{\omega_e}{2}(|e\rangle\langle e| - |g\rangle\langle g|) = \hbar\frac{\omega_e}{2}\sigma_z, \tag{2.6}$$

where the frequency difference ω_e defines the energy gap between the states $|g\rangle$ and $|e\rangle$ and $\sigma_z = (|e\rangle\langle e| - |g\rangle\langle g|)$. Generally, the lifetime of the excited state and the optical quibit coherence is given by the combination of bandwidth of applied laser light and magnetic field noise.

2.5 Motion of ion in a Paul trap

This section briefly discusses the basic physical principles of operation of the Paul traps. We follow the derivation by [48] and [19], which describes the physical origin of the harmonic motion in the linear trap. For technical details of the trap construction and operation, we refer to work [49–51].

In Paul trap, the charged particles are confined with electric potential Φ in three spatial dimensions x, y, z. The Laplace's equation $\Delta\Phi = 0$ requires that at least one of these spatial components of the potential Φ is negative, which would principally result into continuous loss of atoms in that particular direction. The issue can be overcome by inducing a time varying potential having both DC and radio-frequency (RF) electric potential implemented. The potential can be written as

$$\Phi_0(t) = U + V\cos(\Omega_{RF}t), \tag{2.7}$$

with Ω_{RF} being the frequency of the RF trap drive and U, V the amplitudes of the constant (DC) and time varying potentials (RF). For the time varying potential, we can further solve the equations of motion for a particle of mass m and charge Q and distance $\bar{r}$ leading to a differential equation for particle trajectory r_i

$$\ddot{r_i} + \frac{2\alpha_i Q}{m\bar{r}^2}(U + V\cos(\Omega_{RF}t))r_i = 0. \tag{2.8}$$

The Eq. 2.8 can be expressed in form of the Mathieu equation

$$\frac{d^2u}{d\zeta^2} + (a - 2q\cos(2\zeta))u = 0, \tag{2.9}$$

where we have used the substitutions

$$\begin{aligned} a_i &= -\frac{8\alpha_i QU}{m\bar{r}^2\Omega_{RF}^2}, \\ q_i &= \frac{4\alpha_i QV}{m\bar{r}^2\Omega_{RF}^2}, \\ \zeta &= \frac{1}{2}\Omega_{RF}t. \end{aligned} \tag{2.10}$$

The Eq. 2.8 defines regions of stability for ion trapping in terms of the substituted coordinates a_i and q_i. In the practically employed lowest region of stability, where $a_i \ll q_i \ll 1$ [19, 48], the ion trajectory obtains the form

$$r_i(t) = r_i^0\cos(\omega_i t + \phi)[1 + \frac{q_i}{2}\cos(\Omega_{RF}t)], \tag{2.11}$$

where r_i^0 is the distance from a potential minimum of $\Phi_0(t)$ and with ω_i defined as

$$\omega_i = \beta_i\frac{\Omega_{RF}}{2}, \tag{2.12}$$

and the parameter β_i resulting from a substitution

$$\beta_i = \sqrt{a_i + \frac{q_i^2}{2}}. \tag{2.13}$$

The first term in the Eq. 2.11, oscillating at the frequency ω_i, corresponds to the 'secular motion'. The second cosine term describes the 'micromotion' which is a fast oscillation of the particle around the trap center at the frequency of the

RF-drive. The micromotion is usually an unwanted effect in the experiments and we aim for it's minimization within the experimental routine. It is typically detected by experimental method of photo-correlation measurement, where the arrival times of detected photons are modulated with the trap frequency (see Sec. 3.2). The compensation of the excess micromotion is performed by applying additional DC potentials in order to place the atom to the RF potential minimum, where the effect is limited by the residual intrinsic micromotion due to finite motional wavepacket extension.

The secular motion can be decomposed into three geometrical directions, defining the main modes of the oscillation. In the case of the linear Paul trap with the axial symmetry, the conventional normal mode decomposition corresponds to the axial mode along the trap axis and radial modes which are in the plane orthogonal to the axial direction. Radial frequencies are dominantly determined by the potentials originating from the radio-frequency electrodes, according to the Eq. 2.8, while axial mode frequency results dominantly from the DC voltage applied to tip electrodes.

The classical description of the motion of the oscillator suffices only in the limit of large thermal motion of ions. The regime relevant for the experiments presented in this thesis, however, requires introduction of the quantum description of the mechanical oscillator - ion. The exact frequency and the relative strengths of the oscillation modes can be measured spectroscopically, which is described in detail in Sec. 3.6.

2.6 Single ion as a harmonic oscillator

The quantum mechanical harmonic oscillator can be described with the Hamiltonian

$$\hat{H} = \frac{\hat{p}^2}{2m} + \frac{m\omega^2\hat{x}^2}{2}, \tag{2.14}$$

where ω is an angular frequency of oscillation, m is the particle's mass and $\hat{x}$, $\hat{p}$ are the position and momentum operators obeying the commutation relation $[\hat{x}, \hat{p}] = i\hbar$ in single mode of oscillation, forming together the 'phase-space' figure of oscillation. Following the second quantization, it is possible to express the motion in terms of creation and annihilation operators, which are defined as [52]

$$\begin{aligned} \hat{a} &= \sqrt{\frac{m\omega}{2\hbar}}(\hat{x} + \frac{i\hat{p}}{m\omega}), \\ \hat{a}^\dagger &= \sqrt{\frac{m\omega}{2\hbar}}(\hat{x} - \frac{i\hat{p}}{m\omega}). \end{aligned} \tag{2.15}$$

The two operators are non-Hermitian and their commutator is equal to $[a, a^\dagger] = 1$. Together, they form a number operator $\hat{n} = a^\dagger a$, which can be used to further simplify and express the Hamiltonian in Eq. 2.14 as

$$\hat{H} = \hbar\omega(\hat{n} + \frac{1}{2}). \tag{2.16}$$

The Eq. 2.16 expresses the quantization of the energy levels, where the ground state level energy equals to $E_0 = \frac{1}{2}\hbar\omega$. Annihilation and creation operators $a, a^\dagger$ realize subtractions and additions of the single quantum

$$\begin{aligned} \hat{a}\,|n\rangle &= \sqrt{n}\,|n-1\rangle\,, \\ \hat{a}^\dagger\,|n\rangle &= \sqrt{n+1}\,|n+1\rangle\,. \end{aligned} \tag{2.17}$$

The eigenstates of the number operator $\hat{n}$ are states with $|n\rangle$ exact value of energy, corresponding to the energy level n. These states are also denoted as Fock states [52, 53], and together they form the Fock basis. In such a system, any quantum state with the discrete energy can be created by cumulative application of the creation operator on the ground energy level $|0\rangle$

$$|n\rangle = \frac{(a^\dagger)^n}{\sqrt{n!}}\,|0\rangle\,. \tag{2.18}$$

In trapped ion system, nonlinear gates similar to the creation and annihilation operations in ladder scheme are implemented in the joint Hilbert space with the two-level system, on red and blue frequency motional sidebands, described theoretically by Jaynes and anti-Jaynes Cummings interactions.

2.7 Interaction of light with two-level atom in a harmonic potential

The fundamental principle of the motional state engineering lies in the interaction of the valence electron of an ion with light, which s sensitive to a motional state of an atom. In the Paul trap, the transition frequency of the two-level system is modulated by the frequency of the secular motion forming

the modulation sidebands. These sidebands can be conveniently addressed with laser light while stabilizing, narrowing and fine-tuning the laser frequency, and in this way the motional energy can be added or subtracted. The complete Hamiltonian of such an interaction has a form

$$H = H_m + H_e + H_i, \tag{2.19}$$

where H_m defined with the Eq. 2.16 describes the motional degree of freedom, H_e defined in Eq. 2.6 is the Hamiltonian of the two-level system, and the last part H_i describes the mutual interaction with light.

The light field providing the interactions between two-level and harmonic oscillator system can be treated as traveling electromagnetic wave, with the wavevector k, angular frequency ω and initial phase ϕ. Each interaction can be assigned with the physical quantity describing it's strength denoted as a Rabi frequency Ω [19, 54]. For the traveling light field and considering the electric dipole or quadrupole interaction, the interaction Hamiltonian can be found to be described by unified form, where we consider interaction with a single motional mode along x [19]

$$H^{(i)} = \frac{\hbar}{2}\Omega(|g\rangle\langle e| + |e\rangle\langle g|) \times [e^{i(kx-\omega t+\phi)} + e^{-i(kx-\omega t+\phi)}], \tag{2.20}$$

where the second bracket includes the electric field component of the laser propagating along the direction of the motional mode x. Here, the ω and ϕ are the frequency and phase of the excitation laser beam at the position of atom.

The transformation into the interaction picture is then expressed as

$$H_{\text{int}} = U_0^{\dagger} H^{(i)} U_0, \tag{2.21}$$

where $U_0 = \exp[-(i/\hbar)H_0 t]$ is the unitary transformation and H_0 denotes free Hamiltonian $H_0 = H_m + H_e$. In the rotating wave approximation where the rapidly oscillating frequency components are dropped [19], the H_{int} becomes

$$H_{\text{int}}(t) = \frac{\hbar}{2}\Omega_0\sigma_+ \exp[i\eta(ae^{-i\nu t} + a^{\dagger}e^{i\nu t})]e^{i(\phi-\delta t)} + H.c., \tag{2.22}$$

with δ being the detuning from the transition frequency, H.c. is the Hermitian conjugate and Rabi frequency Ω_0 [19]

$$\Omega_0 = \frac{\Omega}{1 + q_i/2}, \tag{2.23}$$

where q_i is the stability parameter of the trap as defined in Eq. 2.10.

Here, we have used the raising and lowering operators $\sigma_+ = |g\rangle\langle e|, \sigma_- = |e\rangle\langle g|$, having the physical meaning of adding and subtracting energy in the

two-level system. Additionally, we have defined the Lamb-Dicke parameter η as

$$\eta = \frac{2\pi}{\lambda}\sqrt{\frac{\hbar}{2m\omega}}, \tag{2.24}$$

which defines the ratio of the size of mechanical oscillation wavepacket with frequency ω with respect to the wavelength of the involved two-level system transition. Physically, the Lamb-Dicke parameter describes the relative interaction strength of coupling of the light to motional modes compared with its coupling to the carrier two-level transition where the motional change is not involved. Additional step towards simplification of the Hamiltonian 2.22 takes advantage of the Lamb-Dicke regime, where

$$\eta^2(2\overline{n}+1) \ll 1. \tag{2.25}$$

Here, $\overline{n}$ stands for the mean value of the energy distribution of involved motional mode. Physically, in the Lamb-Dicke regime, all the transition involving transfer of more than single quantum in the motional mode are strongly suppressed. The interaction Hamiltonian can be expanded into the first order of η as

$$H_{\mathrm{LD}}(t) = \frac{\hbar}{2}\Omega_0\sigma_+[1 + i\eta(ae^{-i\nu t} + a^\dagger e^{i\nu t})e^{i(\phi-\delta t)}] + H.c., \tag{2.26}$$

containing only three resonances for the values of $\delta = -\nu, 0, \nu$. For the case of $\delta = 0$ after the rotating wave approximation [19] the Eq. 2.26 results into 'carrier' transition, with the Hamiltonian

$$H_{\mathrm{car}} = \frac{\hbar}{2}\Omega_0(\sigma_+ e^{i\phi} + \sigma_- e^{-i\phi}), \tag{2.27}$$

describing coupling to two-level system without affecting the motional degree of freedom, with ϕ denoting the phase factor corresponding to the laser phase. The detuning of laser from the carrier transition gives the second case, with $\delta = -\nu$, as

$$H_{\mathrm{rsb}} = \frac{\hbar}{2}\Omega_0\eta(a\sigma_+ e^{i\phi} + a^\dagger\sigma_- e^{-i\phi}). \tag{2.28}$$

This interaction at the lower frequency is conventionally denoted with the term 'red sideband'. From the Eq. 2.28, it is apparent that the motional state is addressed simultaneously with the two-level system, where Lamb-Dicke parameter η plays the role of the 'coupling efficiency', defining the fraction of the original Rabi frequency Ω_0. Based on the initial state of the two-level system, the finite application of the interaction corresponding to H_{rsb} results in either

subtraction of the single motional quantum while the two-level system being in state $|g\rangle$, or oppositely addition of quantum when the system is in $|e\rangle$.

The complementary regime, where $\delta = +\nu$ in Eq. 2.22, is described as

$$H_{\mathrm{bsb}} = \frac{\hbar}{2}\Omega_0\eta(a^\dagger\sigma_+ e^{i\phi} + a\sigma_- e^{-i\phi}). \tag{2.29}$$

The H_{bsb} is denoted as anti-Jaynes-Cummings Hamiltonian, and the corresponding transition as a 'blue sideband'. We can denote the Rabi frequencies for couplings to higher and lower motional modes as $\Omega_{n,n+1}$ and $\Omega_{n,n-1}$, where the scaling is quantized with carrier Rabi frequency and the Lamb-Dicke parameter as

$$\begin{aligned} \Omega_{n,n+1} &= \Omega_0\eta\sqrt{n+1}, \\ \Omega_{n,n-1} &= \Omega_0\eta\sqrt{n}, \end{aligned} \tag{2.30}$$

which results from the properties of the annihilation and creation operators.

The dependence of the Rabi frequency on the motional distribution provides a key feature for engineering of the motional states and consequently for their readout. The Fig. 2.2 shows the visualizations of carrier, blue and red sideband interactions, as they result from the Eq. 2.26. The engineered interaction at blue sideband can be naturally employed to append the motional quanta into the oscillator, for the case that two-level system is in the ground state. On the contrary, the red sideband coupling provides a way for energy subtraction.

2.8 Laser cooling

The ability of laser light to cool the atoms is hardly imaginable from a point of view of the classical physics. The usual applications of lasers involve laser cutting, ablations, heating, or generally, external addition of the energy into some systems. Taking into account the physics of semi-classical light-atom interaction, the laser light can actually realize both. It may either add or remove the energy on the very precise basis, even on the scale of the single motional quanta.

The conventional scheme of the laser cooling employed in ion trapping experiments consists of two stages, however, recent experiments with many ions develop and apply new schemes for simultaneous cooling of many motional modes close to a motional ground state [55, 56].

The Doppler cooling [7] leads to the subtraction of motional energy down to the scale where the quantum effects start to play role. The Doppler cooling is followed by a sideband cooling [57], which takes advantage of the coupling between two-level system and the harmonic oscillator ladder in a sideband

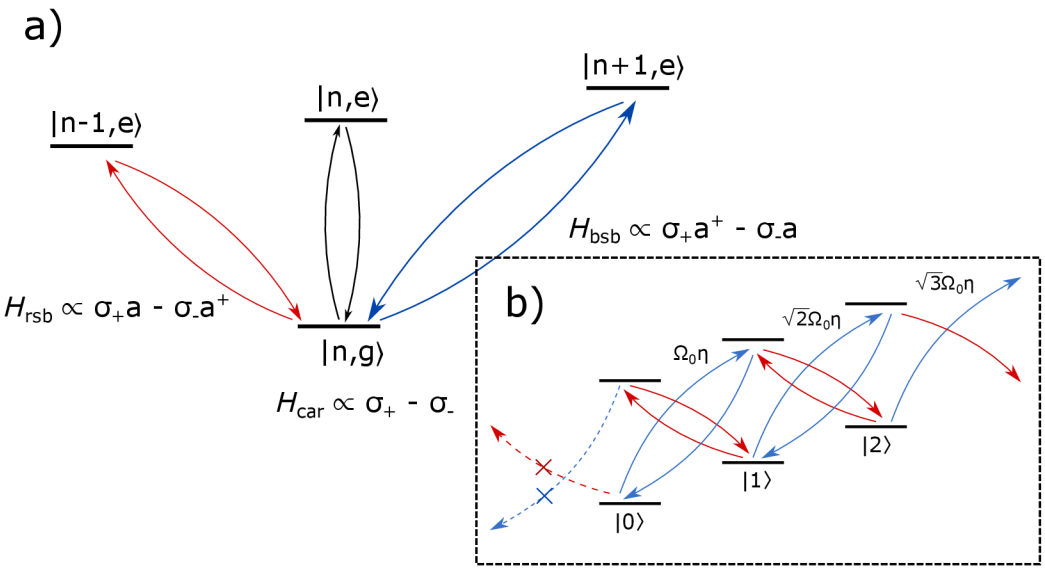

Figure 2.2: a) Visualization of the interactions for carrier (black), red sideband (red) and blue sideband (blue) for two-level system being initially in the $|g\rangle$ state. Hamiltonian H_{rsb} realizes the quantum subtraction between states $|n\rangle|g\rangle \leftrightarrow |n-1\rangle|e\rangle$, H_{car} does not affect the motional number, so that $|n\rangle|g\rangle \leftrightarrow |n\rangle|e\rangle$, and finally the blue sideband realizes transitions at $|n\rangle|g\rangle \leftrightarrow |n+1\rangle|e\rangle$. b) shows same two spin-motional coupling interactions, also pictured for additional higher energy levels. With the increasing energy, the initial Rabi frequency scales with the factor $\sqrt{n+1}$ for blue sideband and $\sqrt{n}$ for the red.

resolved regime. The red-sideband of motion is directly addressed in the pulsed sequence, which possibly leads, after some time of interaction, to the subtraction of thermal energy down to the minimal level. In this case, the motion is said to be 'ground-state' cooled.

The simplest description presented here considers the absence of micromotion, and simplifies the treatment to only single secular motional mode. [19]. In case that the radiative lifetime of the excited state is much shorter than the period of oscillation ($\omega \ll \Gamma$, where Γ is the transition natural linewidth), the single absorption or emission process does not significantly affect the average ion's velocity. At this point, the cooling can be treated as continuous force causing the radiation pressure. The ion thus behaves like a free particle, which is able to sense the motionally induced Doppler shifts. We can write the radiation force

$$\frac{dp}{dt} = F = \hbar k \Gamma \rho_{ee}, \tag{2.31}$$

where ρ_{ee} is the excited state probability [58]

$$\rho_{ee} = \frac{s/2}{1 + s + (2\delta_{eff}/\Gamma)^2}. \tag{2.32}$$

Here $s = 2|\Omega|^2/\Gamma^2$ is the saturation parameter, Ω the Rabi frequency, $\Delta = \omega - \omega_0$ the detuning from resonance, which is contained in effective detuning $\delta_{eff} = \Delta - kv$, including the Doppler shift kv.

The cooling mechanism can be also well understood in terms of momentum conservation and classically treated Doppler effect. In frame of the atom moving towards the laser beam, the actual transition frequency is higher due to the Doppler shift. As a result, the atom most efficiently absorbs the incoming photon in case that it moves towards the laser beam. An atom receives a momentum kick $\Delta p = \hbar k$ in direction of the beam, and then it spontaneously emits a photon in a random direction which, performed over many iterations, leads to the effective net momentum transfer from laser photons and reduction of the motional energy. In this way, the energy may not be reduced down to the ground level, because the ion starts to heat again by recoils originating from the spontaneous emission.

In order to further reduce the motional energy, additional cooling methods have to be employed. The 'sideband cooling' method [19] is based on individual addressing of motional transitions with the narrow-linewidth laser. Here, the lifetime of the excited state has to be much longer than the period of motion ($\omega \gg \Gamma$). For this reason, the cooling is conveniently performed at 729 nm quadrupole transition with $\Gamma^{-1} = 1.16$ s (see Sec. 2.2). The condition $\omega \gg \Gamma$ defines the so-called 'sideband-resolved' regime.

The sideband cooling process is performed in cycles of repetitive absorption on the red sideband followed with the spontaneous emission on the carrier, assuming the condition that the Lamb-Dicke criterion holds. The overall cooling rate R_n is then given by two factors - the probability of the excited state $p_e(n)$ of the motional state and the decay rate of the excited state Γ

$$R_n = \Gamma p_e(n) = \Gamma \frac{(\eta\sqrt{n}\Omega_0)^2}{2(\eta\sqrt{n}\Omega_0)^2 + \Gamma^2}, \tag{2.33}$$

with ground state Rabi frequency Ω_0 and the η denoting the Lamb-Dicke parameter of the transition.

The heating rate is strongly dependent on the mean motional energy, and converges to zero when approaching the ideal ground state of motion. In case that there are not any other heating sources present, the main origin of the heating rate comes from the off-resonant carrier and first blue sideband excitation and the consecutive spontaneous emission back to the electronic ground state. While there is no change in motional mode at the carrier emission,

the decay on the blue sideband appends the heating rate equal to $[\Omega_0/(2\nu)]^2\tilde{\eta}^2\Gamma$. Here, the $\tilde{\eta}$ is the Lamb-Dicke parameter of emission generally different than η, as the emission can occur in any direction. This allows, for example, cooling configurations utilizing three level system where the wavelengths of emitted photon and cooling light are different [59]. The second source of heating may originate from the excitation of the first blue sideband with the probability $(\eta\Omega_0/[4\nu])^2$, which is followed by the decay on the carrier calculated as $(\eta\Omega_0/[4\nu])^2\Gamma$. In the steady state, the mean energy after the sideband cooling can be expressed as

$$\overline{n} = p_1 = \frac{\Gamma^2}{4\nu^2}\left(\left[\frac{\tilde{\eta}}{\eta}\right]^2 + \frac{1}{4}\right). \tag{2.34}$$

Since we have $p_1 = 1-p_0$, the ground state occupation probability after sideband cooling can be written as $p_0 = 1 - (\Gamma/2\nu)^2$ which is close to 1 in case that the condition for the sideband-resolved regime $\omega \gg \Gamma$ holds.

2.9 Angular momentum and Zeeman splitting

A Zeeman effect describes the frequency splitting of atomic energy levels caused by the applied external magnetic fields [60]. The strength of the splitting and the number of lifted degenerate spectral components is related to the total angular momentum, which may be achieved by electron in the current energy level. Addressing of different Zeeman spectral lines allows for multiple experimental configurations, such as ground state cooling and coherent manipulations with motional state, where the overall efficiency of these operations is strongly dependent on the particular spectral line. On the other hand, the unwanted Zeeman transitions can be conveniently suppressed by adjusting the beam geometry and the light polarization.

The total angular momentum J consists of an orbital momentum denoted as L and the electron spin S, where $J = L+S$. A total amount of degenerate Zeeman sub-levels is then equal to $2J + 1$, each of them defined with a magnetic number m_j, acquiring the values in the range of $-J, -J + 1, ...J - 1, J$. In the presence of the external magnetic field B, the degeneracy is lifted and the corresponding sub-levels will form the separate spectral lines. For the small magnetic fields on the order of a few Gauss, frequency difference between the split levels will correspond to the linear Zeeman effect and can be approximated by

$$\Delta\nu = \frac{\mu_B}{h}(m_j g_j - m'_j g'_j)|B|, \tag{2.35}$$

where μ_B is the Bohr magneton, h the Planck constant, and m_j and g_j are the magnetic quantum numbers and Landé factors for corresponding spectral lines [61, 62] and $|B|$ is the intensity of the applied magnetic field. Corresponding Landé factors for particular Zeeman levels of $^{40}Ca^{+}$atom can be taken for example from the reference [48].

Since an electron is a spin-half particle and the energy level scheme consists of a single valence electron only, it may attain the values of $S = \pm 1/2$. In such a case, the eigenvalues of angular momenta would acquire the half integer values as well. The excited state denoted as $D_{5/2}$ will split into total of six sub-levels, and the ground state $S_{1/2}$ will have two sub-levels only, with $m_j = \pm 1/2$. The experimental measurement of Zeeman splitting of the employed $^{40}Ca^{+}$atom is presented and discussed in Sec. 3.6 and schematically depicted in Fig. 3.8.

For atom-photon interaction investigated in terms of magnetic splitting, the change of the total angular momentum between the photon and electron has to be conserved. This raises restrictions on transition between certain Zeeman sub-levels. Considering the interactions at most common dipole transitions, the circularly polarized photon will change the value of m_j by $\Delta m_j = \pm 1$, based on the sign of the circular polarization, while the absorption of photon linearly polarized along the direction of the B field will not change the magnetic quantum number, so that $\Delta m_j = 0$.

The same effect is apparent for spontaneous emission at different Zeeman transitions. The transition which changes the momentum by $\Delta m_j = 0, \pm 1$ will emit linearly polarized photon, or right or left-handed circularly polarized photon, respectively. The transitions are commonly denoted as σ_-, π and σ_+ for $\Delta m_j = -1, 0, +1$. The particular polarization state is always referred to the quantization axis, which is defined here along the direction of the applied B field. Corresponding transition probabilities for spontaneous emission are defined with Clebsch-Gordan coefficients [63].

At the quadrupole 729 nm transition, the allowed change of the angular momenta can be $|\delta_m| \leq 2$, depending on the mutual orientation of beam polarization vector and the magnetic field, with respect to the Paul trap axis. The combin‘lar states of m_j. This can be described with Wigner-Eckart theorem [48, 64, 65]

$$\begin{aligned}\Omega &= \frac{eE_0}{2\hbar} \langle S_{1/2}, m | (\epsilon \cdot \mathbf{r})(\mathbf{k} \cdot \mathbf{r}) | D_{5/2}, m' \rangle | \\ &= | \frac{eE_0}{2\hbar} \langle S_{1/2} | \, r^2 \mathbf{C}^{(2)} \, | D_{5/2} \rangle \sum_{q=-2}^{2} \begin{pmatrix} 1/2 & 2 & 5/2 \\ -m & q & m' \end{pmatrix} c_{ij}^{q} \epsilon_i n_j |. \end{aligned} \quad (2.36)$$

Here, the $\langle S_{1/2} | \, r^2 \mathbf{C}^{(2)} \, | D_{5/2} \rangle$ denotes a reduced matrix element and the matrix

terms in the sum are the Wigner 3-j symbols. The geometric dependent part $g^q = c^q_{ij}\epsilon_i n_j$ denotes the efficiency of transition corresponding to the change of the quantum number m_j. For the axial Paul trap geometry, the vectors corresponding to magnetic field, beam propagation, and polarization can be expressed as $\mathbf{B} = (0, 0, B_0)$, $\mathbf{k} = k_0(\sin\phi, 0, \cos\phi)$ and $\epsilon = (\cos\gamma\cos\phi, \sin\gamma, -\cos\gamma\sin\phi)$. It is useful to define the variables $\phi(k, B)$, denoting an angle between the wave-vector $\mathbf{k}$ and the magnetic field $\mathbf{B}$, and $\gamma(\epsilon, B)$, which is an angle between $\mathbf{B}$ and the polarization ϵ. Considered particular geometry together with these vectors can be conveniently used to characterize the coupling factors g^q as

$$\begin{aligned} g^0 &= \frac{1}{2}|\cos\gamma\sin(2\phi)|, \\ g^{\pm1} &= \frac{1}{\sqrt{6}}|\cos\gamma\cos(2\phi) + i\sin\gamma\cos\phi|, \\ g^{\pm2} &= \frac{1}{\sqrt{6}}|\frac{1}{2}\cos\gamma\sin(2\phi) + i\sin\gamma\sin\phi|. \end{aligned} \tag{2.37}$$

The experimental realization is implemented for a fixed beam direction, which is incident at the angle $\phi(k, B) = 45°$ with respect to the B field aligned parallel with the trap axis. The strength of coupling to particular Zeeman states is dependent on the polarization direction ϵ. This allows particular configurations of the coupling, as depicted in Fig. 2.4. Particularly, in case that $\gamma(\epsilon, B) = 0°$, the coupling is restricted only to transitions which correspond to $\Delta m_j = 0, \pm2$, and is particularly useful for implementation of the sideband cooling and motional state manipulations (Sec. 2.10). Additionally, the case where $\gamma(\epsilon, B) = 45°$ provides reasonable coupling strength to all Zeeman sublevels, so they can be conveniently recognized.

2.10 Coherent interaction on motional sidebands

The coherent Rabi oscillations denote the cyclic behavior of the population probability of the two-level system, undergoing the coherent drive. In implementations presented in this Thesis, they are observed either on carrier transition, which does not involve the interaction with motional mode of freedom, or at motional sidebands, which is accompanied with an addition or subtraction of the single quantum. In such a case, the condition on

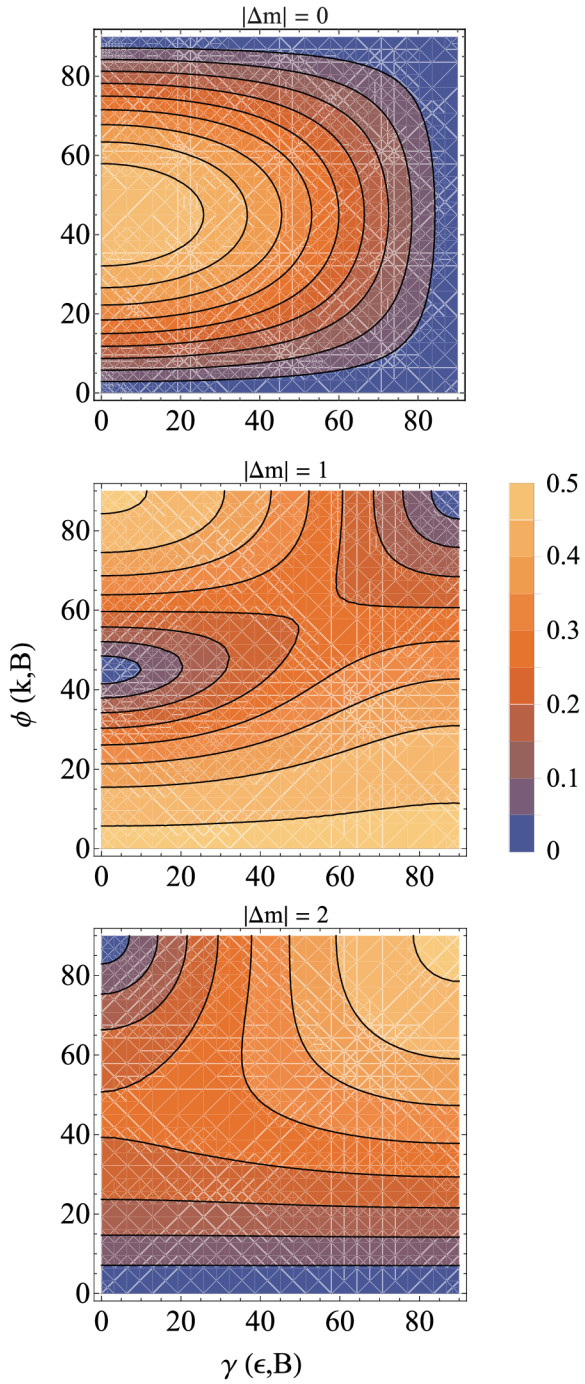

Figure 2.3: Coupling to Zeeman levels corresponding to $\Delta m_j = 0, 1, 2$ from left to right, where $\gamma(\epsilon, B)$ denotes a relative angle between polarization and magnetic field, and $\phi(k, B)$ an angle of wavevector towards the magnetic field. The configuration for typical experimental routine presented in this work is set to $\phi(k, B) = 45°, \gamma(\epsilon, B) = 0°$. Note that these calculations for geometric factors are similar also for other ion species having the same quadrupole line structure and can be thus applied also to calculations considering other atoms.

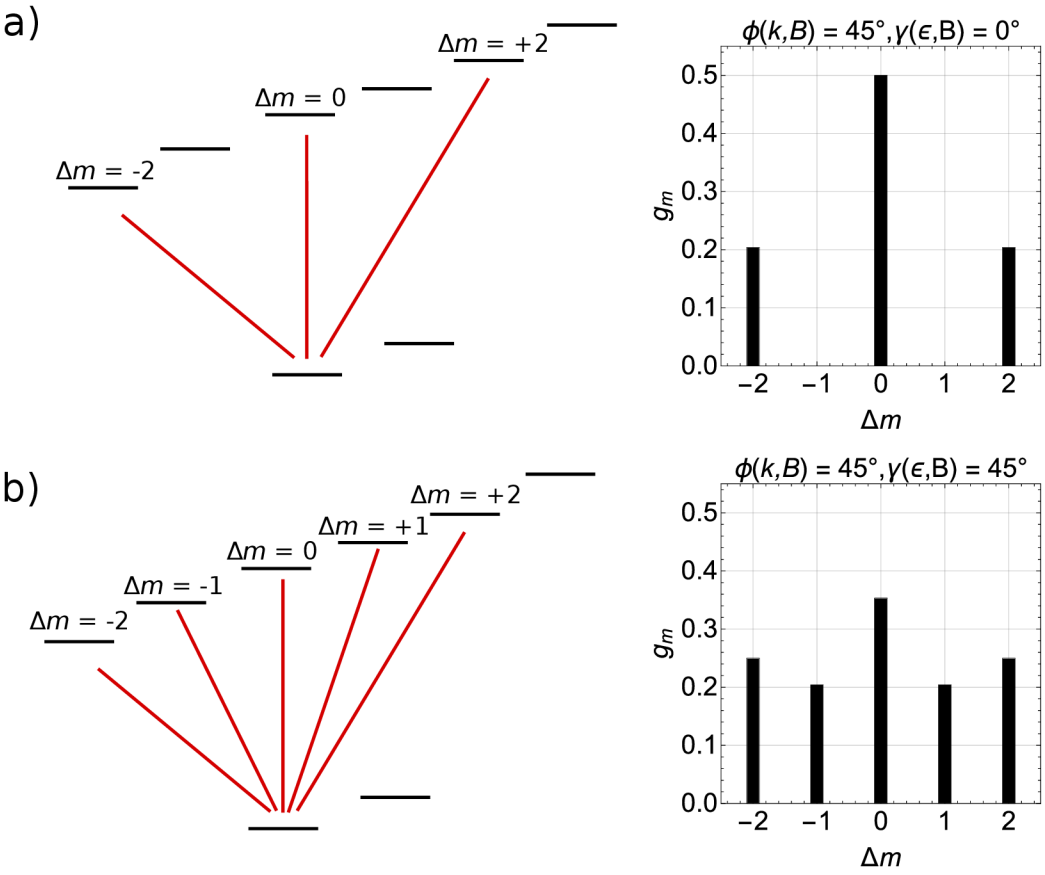

Figure 2.4: Coupling strengths resulting from the Eq. 2.37 and Fig. 2.3 for two particular experimental settings of angles $\phi(k,B)$ and $\gamma(\epsilon,B)$. a) represents the ideal setting employed for our experiment, where only the transitions for sideband cooling ($\Delta m_j = 2$) and motional state engineering ($\Delta m_j = 0$) are coupled. b) shows the setting which allows for spectroscopic measurement of all employed energy transitions. The transitions depicted with red lines correspond to optical pumping set to $S_{-1/2}$ lines. The coupling strength for σ_+ would show analogical results. Bar plots on the right show values of coefficients g_m denoting the coupling efficiency to particular transitions with Δm, calculated from the set of Eq. 2.37.

sideband-resolved regime has to be fulfilled, meaning that the frequency of the motional mode is much larger than the natural linewidth originating from the spontaneous decay rate (so that $\omega \gg \Gamma$, where we consider ω on the scale of 10^6 Hz and $\Gamma \approx 1$ Hz for quadrupole transitions, see Table 2.1) [48]. Consequently, the Rabi oscillations are more conveniently observable at quadrupole 729 transition, due to the long lifetime of the excited state.

Additionally, we consider coupling in the Lamb-Dicke regime, which restricts the possible interactions to 1^{st} motional sideband only, neglecting the higher order motional modes. With an ion prepared close to the motional ground state, there are only three achievable interactions, that being carrier, 1^{st} red and 1^{st} blue sideband, as described in Sec. 2.7. Following this treatment we describe the dynamics of the two-level system at carrier transition as an evolution of population probability of the excited state [48]

$$P_e(\tau) = \frac{1}{2}[1 - \sum_{n=0}^{n_{\max}\to\infty} P_n \cos(\Omega_0(1-\eta^2 n)\tau)], \tag{2.38}$$

where the sum is evaluated over the distribution of the motional modes P_n with $n_{\max} \to \infty$ being the maximal considered motional energy level, theoretically approaching infinity. For evaluations on measured data, the value of $n_{\max}$ is set sufficiently high, so it does not significantly affect the resulting population distribution.

The multiplication of the Rabi frequency Ω_0 with the square of Lamb-Dicke parameter η^2 points to the weak dependence of carrier coupling on the populations. The increasing thermal population in higher phonon states described with the element P_n is then responsible for the gradual damping of the Rabi oscillation, which can originate from contribution of axial and both radial motional modes. For thermal state, where P_n is described with Bose-Einstein distribution, the damped carrier Rabi oscillation pattern can be also expressed as following [48]

$$P_e(\tau) = \frac{1}{2}(1 - \frac{\cos(\Omega_0\tau) + \Omega_0\tau\eta^2(\overline{n}+1)\sin(\Omega_0\tau)}{1 + (\Omega_0\tau\eta^2(\overline{n}+1))^2}), \tag{2.39}$$

where $\overline{n}$ determines the mean energy of the single motional mode. The Eq. 2.39 can be also extended to describe the damping originating from other motional modes, by replacing $\overline{n}$ and η with the summation over all motional modes and their corresponding Lamb-Dicke parameters [48].

The coupling to 1^{st} order motional modes at red or blue sideband contains both the frequency dependence on the Lamb-Dicke parameter η and the Rabi frequency Ω_0. The excited state probabilities $P_e^{\text{bsb}}(\tau), P_e^{\text{rsb}}(\tau)$ for 1^{st} blue and

red sidebands are directly dependent on phonon probability distribution P_n as following

$$P_e^{\mathrm{bsb}}(\tau) = \frac{1}{2}[1 - \sum_n P_n \cos(\Omega_{n,n+1}\tau)\exp(-\gamma_n\tau)], \tag{2.40}$$

$$P_e^{\mathrm{rsb}}(\tau) = \frac{1}{2}[1 - \sum_n P_n \cos(\Omega_{n,n-1}\tau)\exp(-\gamma_n\tau)], \tag{2.41}$$

with

$$\Omega_{n,n+1} = \Omega_0\eta\sqrt{n+1}, \Omega_{n,n-1} = \Omega_0\eta\sqrt{n}, \tag{2.42}$$

where the coefficient γ_n describes the Rabi oscillation damping which is dependent on the energy of the motional mode denoted with n. In our experimental observations and also in references [19, 66] it has been found that the damping coefficient scales up with the motional energy and can be described as

$$\gamma_n = \gamma_0(n+1)^x, \tag{2.43}$$

with γ_0 is the damping of the motional ground state, and x is the scaling factor which is related with the noise properties, typically estimated as $x = 0.7$, see reference [66] and also experimental verification in Sec. 3.14.3.

2.11 Basic definitions of non-classicality in ion's motion

There are two basic ways to treat the quantum mechanical motional states. The first treatment employs the decomposition of arbitrary state in the number state basis, as described in Sec 2.6. Alternatively, the motion can be treated similarly as in quantum optics, using the theory of coherent states, firstly introduced by Glauber in 1963 [20]. In this way, the density matrix of the state can be described as [67]

$$\rho = \int P(\alpha)\,|\alpha\rangle\langle\alpha|\,d^2\alpha, \tag{2.44}$$

where the outer product $|\alpha\rangle\langle\alpha|$ denotes the over-complete non-orthogonal basis of coherent states. By definition in [67], if $P(\alpha)$ has meaning of classical probability density function, then state is classical from the perspective of classical coherence theory of linear oscillators. Such states can be obtained

by classical external linear drive of such oscillators with a fixed frequency. If this is not the case, the state is called 'non-classical'. The special subclass of non-classical states presents sub-Poissonian statistical properties where the variance in phonon number is smaller than the mean phonon number [68]. This is also the case of Fock mechanical states, where the phonon number noise is principally zero, while the phase is infinitely uncertain. However, such noise reduction can be also approached by a displaced squeezed ground states of oscillators. They can be obtained using diverse linearized nonlinear dynamics described approximately by the interaction Hamiltonians maximally quadratic in the annihilation and creation operators. Such dynamics ideally keeps Gaussian ground-state distributions of position and momentum still Gaussian. To basically distinguish such trivial cases on sub-Poissonian statistics from more relevant and applied still imperfect Fock states, quantum non-Gaussian sub-set of non-classical states must be introduced.

Similarly with the definition in Eq. 2.44, we define the 'quantum non-Gaussianity' with use of the following equation [21]

$$\rho = \int P(\lambda) \left|\lambda\right\rangle \left\langle\lambda\right| d^2\lambda, \tag{2.45}$$

where $\left|\lambda\right\rangle = S(r)D(\alpha)\left|0\right\rangle$ is a pure Gaussian state, with displacement operator $D(\alpha)$, squeezing $S(r)$ and $\left|0\right\rangle$ denoting the vacuum state. In Eq. 2.45, the $P(\alpha)$ denotes the probability density distribution of Gaussian states $\left|\lambda\right\rangle$. In case that the quantum state cannot be described in a way of Eq. 2.45, it is denoted as 'quantum non-Gaussian'.

A convenient way to characterize the quantum states is the direct reconstruction of number states population, where for example the Fock state probabilities may be directly obtained from the fit of the coherent interaction (see Eq. 2.40). A specific criteria has been derived [21], which distinguishes Gaussian and quantum non-Gaussian states based solely on the measured populations, and can be applied even in the presence of high losses or for states with positive Wigner functions in whole phase space.

The stricter form of quantum non-Gaussianity criteria can be formulated using the hierarchical properties of the Fock states, which directly relate to some of the sensing applications. The hierarchical nature of the criteria also provides a way to gradually describe the 'quality' of generated imperfect Fock states, by evaluating their robustness with respect to thermal losses, which is specific for each Fock state. The genuine quantum non-Gaussianity (GQNG) is defined similarly to quantum non-Gaussianity (QNG), with the Eq. 2.45, where $\left|\lambda\right\rangle = S(r)D(\alpha)\sum_{m=0}^{n-1} c_m \left|m\right\rangle$ denotes the sum of coherent and squeezing operations applied on the mixture of number states with order $(n-1)$ smaller

than the number state of interest. Therefore, the GQNG state is such state, which cannot be expressed with a mixture of displaced and squeezed number states of a lower rank. A specific $P_n^{\max}$ can be derived for each number state, for witnessing the GQNG threshold. In a single term, the genuine quantum non-Gaussian state of rank n can be defined as a state, which cannot be achieved by

$$|\psi\rangle = D(\alpha)S(r)\sum_{m=0}^{n-1} c_m |m\rangle . \tag{2.46}$$

Alternatively, it is possible to derive the condition for genuine quantum non-Gaussianity for Fock states with use of stellar hierarchy formalism, as described in the reference [69].

2.12 Estimation of discrete non-classicality on broad phonon number distributions

In Section 2.11, we discuss the definitions of criteria of non-classicality and quantum non-Gaussianity. In measurements presented, we employ additional non-classicality measures, which are able to better describe specific features of probability distribution shapes. We use the Fano factor defined as [70]

$$F = \frac{\langle n^2\rangle - \langle n\rangle^2}{\langle n\rangle}, \tag{2.47}$$

which describes the ratio between the state's variance and mean phonon number. The values of $F \geq 1$ point to distributions with Poissonian or super-Poissonian distribution, while $F < 1$ corresponds to non-classical sub-Poissonian statistics.

Klyshko's hierarchic criteria of nonclassicality [71] can be conveniently employed when assessing non-classical properties manifested dominantly in the high population of particular Fock state, as they are sensitive to population difference in three neighboring states. For a chosen phonon number n, the Klyshko's criterion is defined as

$$K_n = (n+1)P_{n+1}P_{n-1} - nP_n^2. \tag{2.48}$$

Clearly, for number states of the order n, the corresponding measure of K_n is negative.

Experimentally accessible indicator of nonclassicality and quantum non-Gaussianity is the value of Wigner function at the origin of the phase space,

which can be calculated as [19]

$$W(0,0) = \frac{2}{\pi} \sum_{n=0}^{n_{max}} (-1)^n P_n, \tag{2.49}$$

where P_n corresponds to the measured population distribution. For odd populations in number state basis, the origin value of Wigner function is negative and thus serves as a direct indicator of quantum non-Gaussianity in the low loss regime. However, the Eq. 2.49 fails to detect the non-classical properties for even states and a various range of other quantum non-classical states. This can be generally remedied by investigating the other regions in the phase space.

Finally, to have a global identification of the non-classical aspects of different states with a large variance phonon number distribution, we employ the entanglement potential [72] defined as the amount of entanglement contained in the state

$$\rho_{\text{ent}} = e^{\pi/4(ab^\dagger - a^\dagger b)} \rho_{\text{k}} \otimes |0\rangle\langle 0| \, e^{-\pi/4(ab^\dagger - a^\dagger b)}, \tag{2.50}$$

where a and b are the annihilation operators for the first and the second oscillator mode, respectively. In quantum optics, this operation corresponds to splitting an optical mode on a balanced beam splitter. The entanglement potential (EP) measure reflects the fundamental inability to generate entanglement behind the beam-splitter if the state ρ_{k} at the input is not non-classical and takes further advantage of greater availability of measures of bipartite entanglement relative to measures of nonclassicality. In our case we quantify the entanglement using the straightforwardly computable logarithmic negativity [73]

$$LN(\rho_{\text{ent}}) = \log_2 \| \rho_{\text{ent}}^{\text{PT}} \| \tag{2.51}$$

Here, PT denotes partial transposition and $\| A \| = \text{Tr}\sqrt{A^\dagger A}$ corresponds to trace norm. This measure is not unique [74–76], however, it can be easily numerically evaluated even for high-dimensional non-Gaussian states [77]. Experimentally, it requires full density matrix and might too sensitive to statistical and estimation errors.

3. Experimental methods to control ion's motion

This Chapter covers the basic description of implemented experimental routines of ion trapping, controlling the ion's fluorescence rate and also motional state. We include experimental and technical details on utilization of physical principles described earlier in Chapter 2.

3.1 Laser manipulation of internal energy level populations

The crucial point of the experimental control lies in addressing of the transitions between energy levels in the $^{40}Ca^{+}$ ion (see Sec. 2.1 and Fig. 3.1). This is done by employment of in total four lasers. The description of the laser stabilization using frequency offset locks to the fiber frequency comb and including the particular set up for stabilization of the qubit 729 nm laser to the level of a few Hz can be found in [50, 51]. In addition, other two lasers at 422 nm and 377 nm are used to produce singly ionized $^{40}Ca^{+}$ion. At first, one of the two valence electrons is excited at transition $4s^2S_0 \rightarrow 4s4pP_1$ by 422 nm radiation, and in the second step, it is sent into continuum by laser at 377 nm.

The transition $4S_{1/2} \rightarrow 4P_{1/2}$ is used for Doppler cooling and also for fluorescence detection, due to the short excited state lifetime which is 6.9 ns. The light of the fluorescing atom is collected with a high numerical aperture lens[1], which is then further sent towards the EMCCD camera[2], or to the avalanche photo-detector[3]. In typical experimental setting, it is possible to detect up to 4×10^4 photons per second.

In the cooling and detection process at $4S_{1/2} \rightarrow 4P_{1/2}$ transition, the finite

[1] Sill Optics S6ASS2241, covering 2 % of full solid angle [50]

[2] ANDOR Luca, type S

[3] Laser Components COUNT Blue

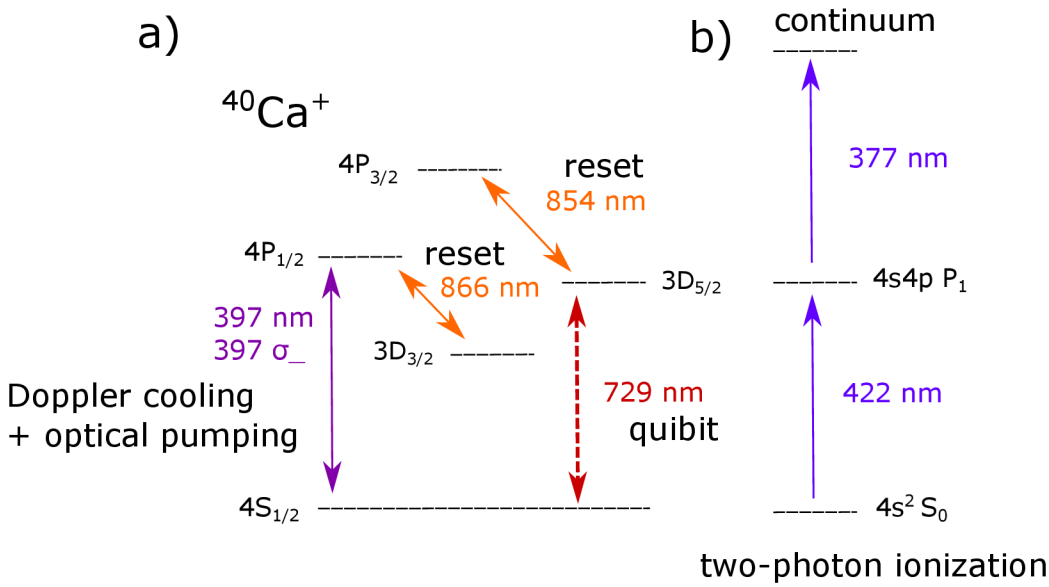

Figure 3.1: Processes of electronic state manipulation used in experiments. a) shows spectral lines for experimental control and motional manipulation. The fluorescent 397 nm transition serves for Doppler cooling and also for optical pumping with circularly polarized beam. 866 nm serves for the re-shuffling of the dark state $3D_{3/2}$ after Doppler cooling. The narrow quadrupole 729 nm transition defines the two-level system coupled with the harmonic oscillator. The beam at 854 nm serves for a reshuffling of the $3D_{5/2}$ state down to the ground state $4S_{1/2}$. In addition, the special circularly polarized beam at 397 nm denoted as σ^- is used to distinguish transitions corresponding to two Zeeman levels of $4S_{1/2}$ ground state. b) shows the two-photon ionization process used for ion trapping.

branching ratio of the excited state results into a probability of decay into the metastable $3D_{3/2}$ state. Therefore, the reshuffling laser at 866 nm is employed to re-excite the atom into the $4P_{1/2}$, from where the electron may decay back to the ground level $4S_{1/2}$. The two beams at 397 nm and 866 nm have to be implemented simultaneously, in order to detect the ion's fluorescence and reduce the motion in Doppler cooling step.

The quadrupole transition at $4S_{1/2} \rightarrow 3D_{5/2}$ is addressed with the 729 nm laser beam. The lifetime of the excited $3D_{5/2}$ state is very long (1.16 s), so the 729 nm beam frequency has to be narrowed and stabilized to the bandwidth scale of approximately tens of Hz. This is achieved by PDH locking to a high finesse reference cavity, which is in detail described in work [51]. The transition between the states $3D_{5/2} \rightarrow 4P_{3/2}$ serves for the reshuffling of the excited D-state to the ground state $S_{1/2}$.

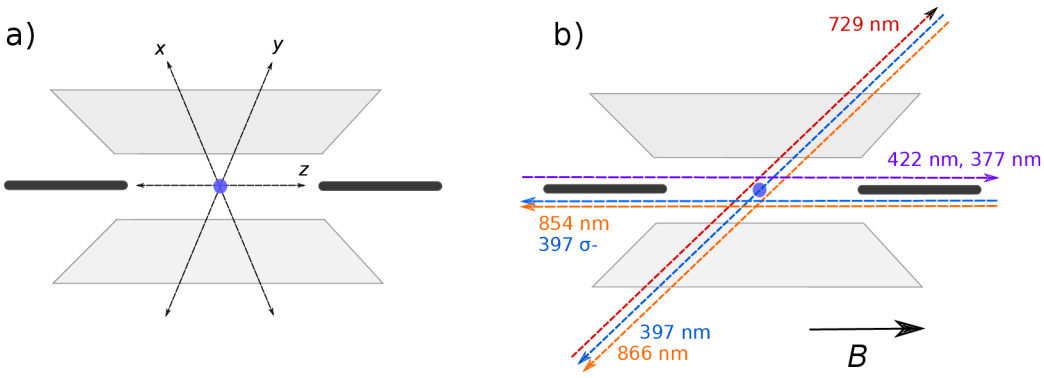

Figure 3.2: Geometry of normal motional modes in the trap and alignment of the laser beams. a) shows the three main directions of oscillations, where x, y represents two radial modes which are bound to two pairs of 'blade' electrodes (only one pair is shown here), z is the direction of the axial mode. b) depicts the alignment of lasers used for internal state control and two-photon ionization process, with respect to trap axes. A Doppler cooling is performed with 397 and 866 nm lasers, 729 nm provides tools for the motional state engineering, 377 and 422 nm lasers implement the ionization step, 397 σ^- does the optical pumping and 854 nm re-shuffles the excited state level. For the description of the typical pulse sequence, see Sec. 3.4. The direction of the magnetic field depicted with B is set as parallel to the axis of the trap in all experiments presented in this thesis, which allows for a convenient optical pumping scheme with the 397 circullary polarized beam along the trap axis.

The geometric orientation of the laser beams with respect to the trap is depicted in Fig. 3.2. The orientation takes into account the geometry of direction of normal oscillation modes in the trap. The beams which are aligned under 45° angle have a significant overlap with all of the three motional modes of a single ion. This direction is used both for the Doppler cooling lasers and for the qubit laser. The 397 σ_- beam, denoted as 'optical pumping', propagates parallel to the trap axis. The beam is circularly polarized, and it's direction coincides with the local magnetic field vector. This ensures that only one of the two Zeeman levels of the ground state $S_{1/2}$ can be coupled [59, 78].

3.2 Compensation of micromotion

Micromotion is the fast oscillation which is being driven by the trap frequency Ω_{RF}. The amplitude of the micromotion increases as a function of ion's distance from the trap RF potential minimum. In order to allow for independent compensation of the excess micromotion, additional two pairs of compensation

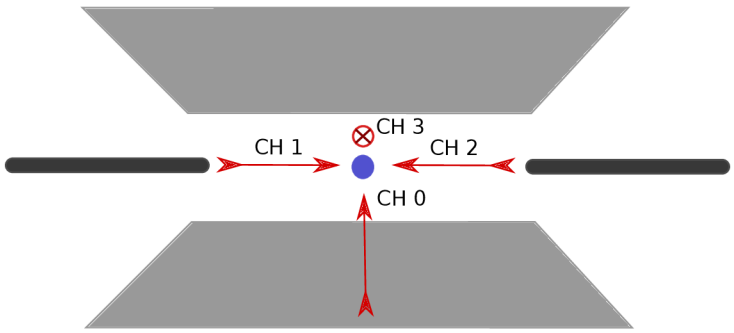

Figure 3.3: Main directions of the DC potentials in the employed Paul trap. Arrows with labels Ch_1 and Ch_2 denote directions of the axial confinement in the trap. Additional pointers Ch_0 and Ch_3 denote direction of applied compensation voltages, where direction of arrow Ch_3 is perpendicular with the plane of the page. Compensation electrodes are not pictured in the schema.

electrodes are employed inside the vacuum chamber, with DC potential on scale of tens to one hundred volts. Fig. 3.3 depicts the simplified geometry of the two pairs of the micromotion compensation electrodes and of two axial electrodes in our linear trap, observed from a direction of imaging on the CCD camera. All of the electrodes are connected to the source of the high DC voltages[4].

The fundamental limitation arises while aiming to compensate micromotion for long ion chains or large 3D ion crystals with a finite radial size [79, 80]. Since the amplitude of micromotion increases with the distance from the trap center, the full compensation cannot be achieved for all ions simultaneously. For compensation of the axial micromotion over the extended axial scale, our setup included also the possibility to drive the radial RF electrodes symmetrically, but with opposite phase [81, 82]. However, as this thesis is focused on experiments with single ions, experiments presented here employ the more conventional RF driving corresponding to one pair of opposite blades at ground and other pair oscillating at RF potential around this ground value.

There are various experimental routines to minimize the micromotion [81]. At the first stage of the experiment, when the amplitude of the micromotion is very high, it can be detected directly with the CCD camera [83], and recognized as a motional blur caused by the fast oscillation. The coarse alignment of the atom is employed, to erase the blur and position the atom closer to the trap center [81].

Another method is a coincidence correlation method [81, 84], which is based on detection of Doppler shifts of ion moving towards and backwards to

[4]powered by ISEG high DC voltage source

Ch_0	102 V
Ch_1	1382 V
Ch_2	1017 V
Ch_3	96 V

Table 3.1: Tip voltages corresponding to the ion's position in the center of the trap (Ch_1 and Ch_2), and compensation voltages which are measured to provide the minimal micromotional amplitude obtained by a photon correlation method (Ch_0 and Ch_3). Current values are valid for RF trap setting of Ω_{RF} = 30 MHz and amplitude corresponding to transmitted power of 4 W.

the direction of the excitation - Doppler cooling. Then, the micro-motional oscillations are imprinted to the detected fluorescence as a periodical modulation of arrival times of incoming photons.

We implement the correlation method as a coincidence measurement between the trigger derived from the RF-drive, and the ion's fluorescence detected with the avalanche photo-diode detector. The result is recorded with a two-channel time-correlating device[5] with 4 ps time resolution. The employed avalanche detector has a jitter approximately 1 ns, so the bandwidth of measurable correlations is approximately 1 GHz, which is large enough to cover the correlation signals expected at the trap frequencies around 30 MHz.

The sample results are presented in Fig. 3.4. The displayed data show the correlation histogram of coincidence counts between the triggering pulse derived from the RF-signal and the detected fluorescent photons. For the case of uncompensated excess micro-motion, the correlation histogram should in principle show harmonic periodical signal. However, the nontrivial dependence of the excitation parameters in the multi-level structure of $^{40}Ca^{+}$ion, together with the nonlinear response of the excitation probability of the two level system on the effective detuning of an ion result in typical signal shown in the Fig. 3.4. For the compensated case, the probability of photon arrival will be constant for all time delays, returning the flat line in the histogram. When the ion is displaced to the opposite side of the RF potential, one observes a change in the phase of the correlation signal equal to π.

Additional method of micro-motion estimation is the measurement of the ion fluorescence in Hanbury-Brown-Twiss experimental configuration [85], where several very useful modifications of such scheme have been developed including the phase interferometry of the emitted fluorescence before the correlation measurement. This, contrary to the previous method, allows for the detection of

[5]PicoHarp 300

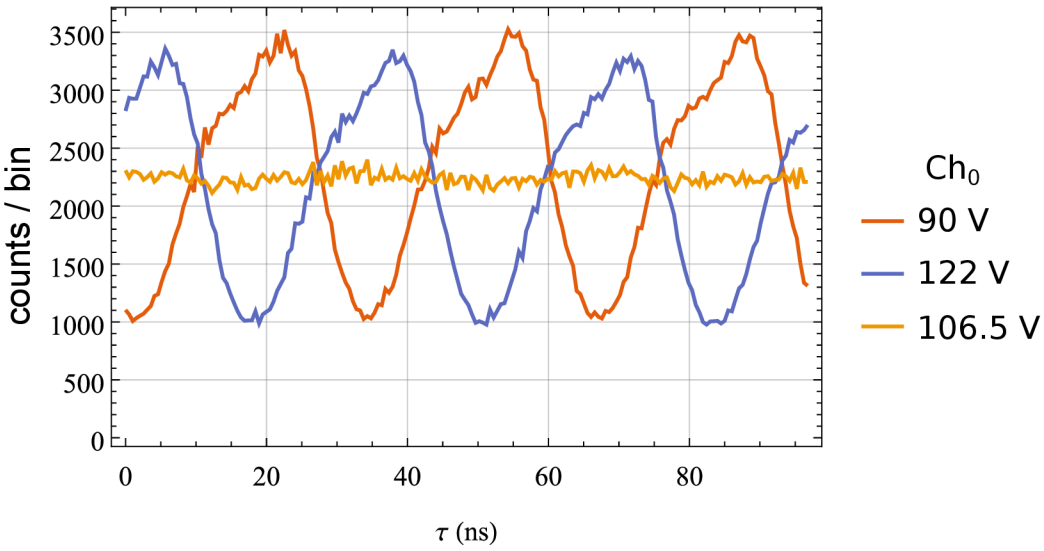

Figure 3.4: Sample data histogram for measurement of the RF trigger - photon correlation, used for micromotion sensing. The vertical axis shows the histogram counts as a function of delay τ. The histogram resolution is 0.512 ns per point. The blue and red lines show the case of the de-compensated excess micro-motion. The contrary phases imply the ion is located at the opposite side of the potential well. The yellow line shows the coincidence counts for nearly ideally compensated excess micro-motion. The ion is displaced in the direction of the Ch_0 electrodes.

the micromotion also in the direction of detection if the scattered fluorescence. However, due to the small count rates on scales reaching tens of kHz at maximum, the data acquisition of photon-photon coincidences is much longer compared with to cross-correlations with external trigger at 30 MHz frequency.

In this context we would also like to point to the recent work devoted to measuring enhancement in sensing the micro-motional modulation by correlating the fluorescent count rate with it's reflection at the distant mirror [86, 87]. In such a configuration, the detection sensitivity is enhanced with respect to the directly observed fluorescence by a factor of more than 100 due to the phase-sensitive interferometric measurement of photons.

Finally, in Table 3.1, we write the voltages corresponding to compensation and tip electrodes, which were measured to optimally compensate the micro-motion for presented experimental tests. The trap is driven in asymmetric configuration, where the two electrodes are grounded, and the other two are supplied with the RF, at the frequency corresponding to 30 MHz and the RF power transmitted to the trap of 4W.

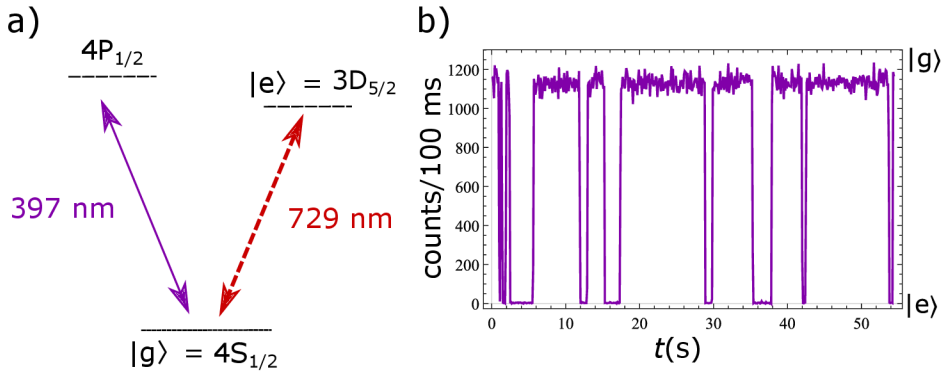

Figure 3.5: V-like energy level scheme (a) with the measured 'quantum jumps'(b) for weakly continuously illuminated transition at 729 nm, showing the discrimination between two quibit eigenstates in σ_- basis. The detected count-rate points to the population of level $|g\rangle = 4S_{1/2}$, denoted as a 'bright state', while the low count rate around zero points ot the ion being in the 'dark state' $|e\rangle = 3D_{5/2}$.

3.3 Internal state detection

For estimation of the population of the qubit states in the σ_z basis we employ method which is in literature commonly denoted as 'electron shelving' [88, 89]. It enables the detection of the ion's internal state with efficiency typically higher than 99 %. The basic principle lies in addressing the additional electronic level denoted as $|r\rangle$, so the scheme finally operates as a V-like three level system, as described in Fig. 3.5 a). Thus, for the case when electron populates the state $|e\rangle$, it is impossible to detect any fluorescence except for the rate of the dark counts.

In our experimental scheme, we realize the two-level system at $4S_{1/2} \rightarrow 3D_{5/2}$ transition at wavelength 729 nm, where state $|g\rangle$ corresponds to the $4S_{1/2}$ level, and the excited level $|e\rangle$ is the $3D_{5/2}$ state. Fluorescence is detected at 397 nm transition $4S_{1/2} \rightarrow 4P_{3/2}$. Once the electron is excited into the state $3D_{5/2}$ by the 729 nm laser, the fluorescence at 397 nm is suppressed. Therefore, the state $|e\rangle$ is denoted as a 'dark' state, while the opposite level $|g\rangle$ is the 'bright' state. The 'quantum jumps' [88] corresponding to the abrupt change in the population of the excited state due to the projection by photon detection are manifested in the famous telegraphic signal, see the Fig. 3.5 b) for the example of such measurement. The flat areas where the fluorescence is measured correspond to the situation when the ion is projected to the ground state, while the areas with rate equal to zero correspond to the projection on the excited level $|e\rangle$.

3.4 Pulsed sequence control

The electron shelving method provides the projection to one of the eigenstates of the two-level system. Despite the actual superposition, the single shelving experiment always returns a yes/no answer, if the atom was in the 'dark' or 'bright' state. Therefore, any experimental sequence is implemented with a high number of repetitions, which allows to obtain the statistics of projections on the two-level system. The sequences of excitation laser pulses are directed with the programmable RF-generator[6] and from here, pulses are delivered to the set of acousto-optical modulators[7]. All the experiments consist of a hundred independent sequence repetitions, which suppress the projection noise and provide the probability amplitudes with the reasonable error estimate.

A general form of the sequence is depicted in Fig. 3.6. The sequence starts with the Doppler cooling, followed with optical pumping, possibly sideband cooling which further reduces the mechanical thermal energy, then with state manipulation and finally the state analysis.

3.5 Optical pumping

The optical pumping in the experimental sequence is performed in order to set the preference of electron transition into one of two possible Zeeman sublevels of the $4S_{1/2}$ manifold. The splitting itself is performed with a pair of Helmholtz coils placed parallel with the trap axis [50, 51], inducing the external magnetic field of approximately 10 Gauss. The particular splitting of the spectral lines for employed experimental setting was measured spectroscopically (see Fig. 3.8 in Sec. 3.6). Here, we describe the basic physical principle and experimental optimization process of the optical pumping.

A weak and short optical pumping pulse at 397 nm is applied in each sequential experiment. The pumping photon bears a left or right hand circular polarization state, carrying the angular momentum $\Delta m_j = \pm 1$. Consequently, following the photon scattering into the unwanted ground state level, an incoming pumping photon implements an excitation back to the excited state, which is followed by additional spontaneous emission. This process occurs, until the electron travels into the selected m level, which is unaffected by the pumping pulse.

From an experimental point of view, the choice between σ_+ and σ_- can be made arbitrarily, however, it is necessary to choose one configuration for

[6] electronics based on FPGA logic, controlled in LabView software

[7] Brimrose, central frequency of modulation typically 250 MHz

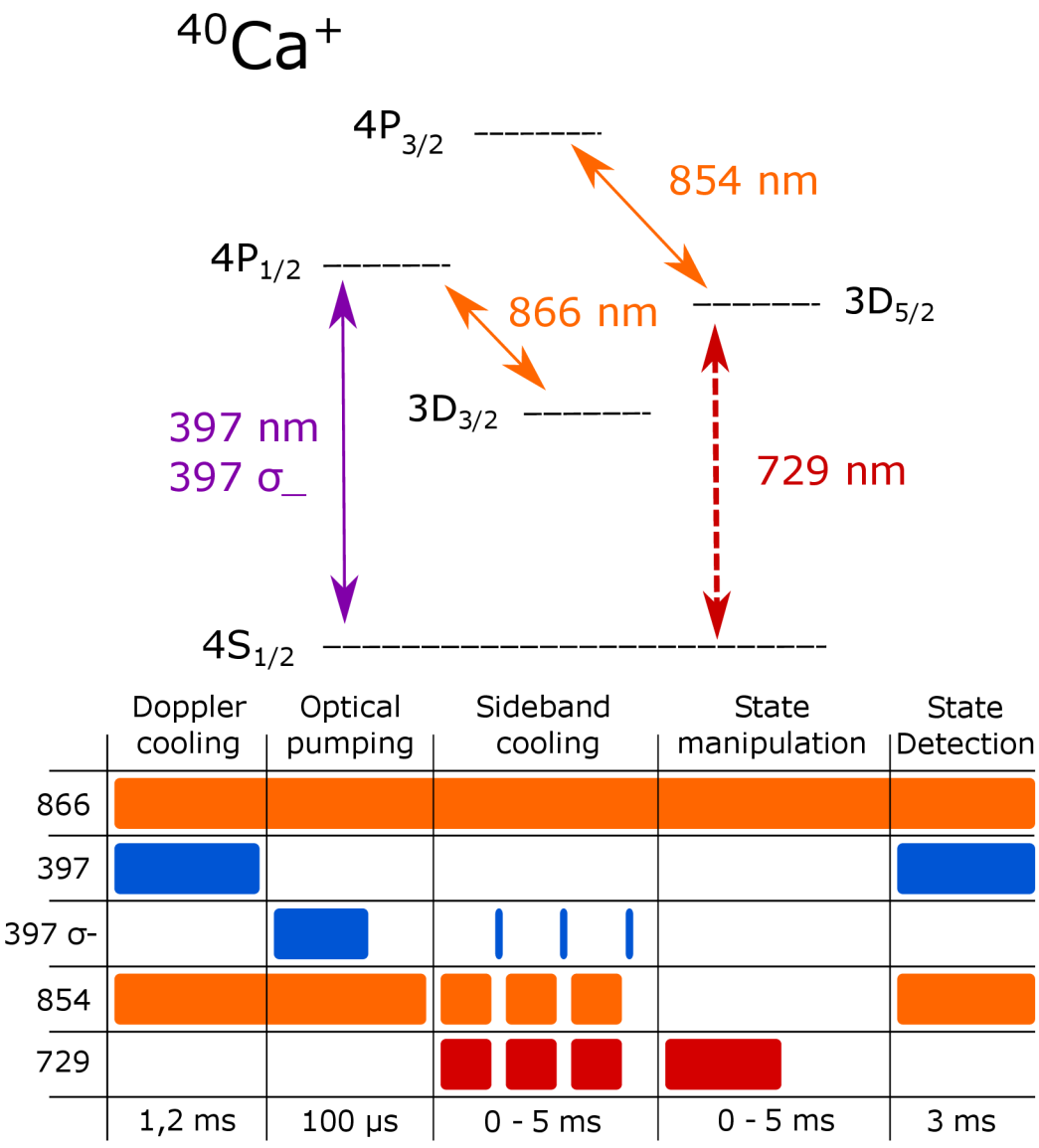

Figure 3.6: Example of the experimental sequence used for motional state preparation, manipulation and state detection. The Doppler cooling represents the continuous illumination with 397 nm and 866 nm lasers, typically with 1.2 ms duration. The optical pumping initializes the state of the electron to particular m_j state of the S state. The sideband cooling part consists of multiple pulses of simultaneous 729 nm and 854 nm beams, which are interrupted with short 397 σ_- optical pumping, preventing the population to accumulate in unwanted Zeeman component of the S state through rare decay of the excited $P_{3/2}$ state to $D_{3/2}$ followed by the optical reshuffling using 854 nm laser back to the S state manifold. The overall length of the sideband cooling sequence part depends on application. For ground state cooling with over 98 % of population in the state $|n\rangle = 0$, the required length exceeds 3 ms. State detection refers to the electron shelving, and also contains the gating of window for detection by the APD.

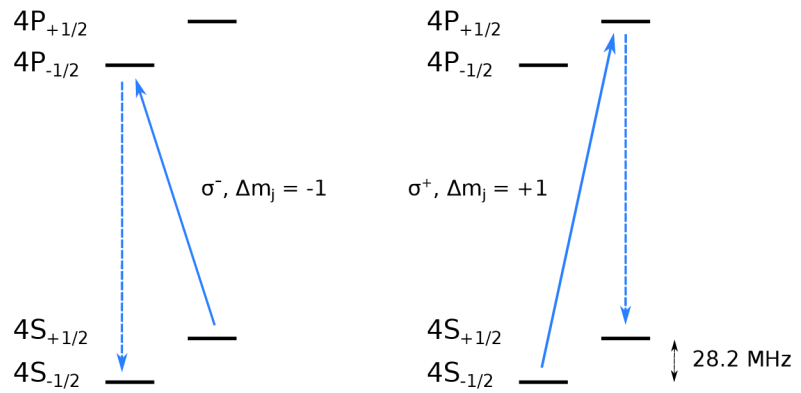

Figure 3.7: Optical pumping realized at the 397 nm with additional addressing beam, employed in the axial direction. The σ_+ and σ_- correspond to the left or right handed circularly polarized photons, which induce the angular momentum change of $\Delta m_j = \pm 1$. In the case of photon scattering into one of the states addressed with pumping pulse, the electron is transferred back to the excited level.

all experiments and keep it fixed. In our experimental scheme, we choose to implement the experiments at σ_- transitions. This also brings up an advantage for sideband cooling regime (see Sec. 3.8), which is realized at the 1^{st} axial red detuned sideband of the outermost transition $4S_{1/2}(m = -1/2) \rightarrow 3D_{5/2}(m = -5/2)$. Particularly in this case, the probability of off-resonant excitation of other spectral lines is decreased, as the transition is located at the edge of the spectrum. The principle of the optical pumping is displayed in Fig. 3.7.

In the experiment, the setup and optimization of the optical pumping routine is set as following. The optical pumping beam is applied in the axial direction of the trap, and it's polarization is set to circular. The polarization is optimized in the regime of continuous laser excitation, when the standard Doppler cooling beam at 397 nm is turned off, so the the ion is Doppler cooled only in the axial direction. This is however not a significant issue for ion's stability on scale of a few minutes, which are required for optical pumping optimization.

Once the polarization of the incoming beam is set to circular, the fluorescence radiated at $4P_{1/2}(m = +1/2) \rightarrow 4S_{1/2}(m = +1/2)$ is suppressed. Due to the circular polarization of the interacting photon, one of the σ transitions is then driven maximally, while the latter is not addressed. The rotation of the polarization angle by π will then set the preference for scattering into the second Zeeman sub-level.

Typically, the power of optical pumping beam is set to approximately 15 μW. We aim to illuminate the ion with the attenuated beam, which would, however, still reliably implement the optical pumping effect. The 397 σ beam, while being

applied at high power for a long time, may cause the motional heating of the axial mode. The power of optical pumping is optimized at Rabi oscillations for carrier transition, and it is set to the lowest intensity and temporal length, which does not yet lead to the decrease of the carrier flop contrast, which would be caused by population scattering into the neighboring $|S\rangle$ state.

3.6 Spectroscopy on the quadrupolar transition

The spectroscopic measurements provide a tool to directly measure the energy level structure of the $4S_{1/2} \rightarrow 3D_{5/2}$ transition (see scheme in Fig. 3.8). They allow for determination of all of the crucial information about the internal energy level structure of the probed transition and, at the same time, serve for precise estimation of its temperature or even of the full motional state. They can be used also to determine the magnitude of DC magnetic field at the position of ion and also the Zeeman splittings.

The pulse sequence consists of Doppler cooling, optical pumping, the probe by a weak 729 nm laser pulse, and the state detection by electron shelving. Each point of the spectrum corresponds to a probability originating from 100 repetitions of the experimental sequence. The frequency detuning of the 729 nm pulse is controlled by setting the modulation frequency to the acousto-optical modulator in double-pass configuration, while the first order diffracted modulated light from the second modulator is sent to the experiment.

In order to observe transitions from both $4S_{1/2}$ states, we first set the optical pumping such that it coincides with the σ_- transition of the $4S_{1/2} \rightarrow 4P_{1/2}$ and implement frequency spectroscopy on the quadrupole $4S_{1/2} \rightarrow 3D_{5/2}$ transition. After that, the polarization of the pumping pulse is rotated to the orthogonal state σ_+, and the other five carrier transitions at $4S_{1/2} \rightarrow 3D_{5/2}$ can be observed. The positions of measured spectral lines are determined with respect to the AOM modulation frequency. The measured spectra corresponding to $4S_{-1/2}$ state are depicted in Fig. 3.9. From the resulting values, we determine the physical frequency splitting of $4S_{1/2}(m = -1/2)$ and $4S_{1/2}(m = +1/2)$ ground state as 28.22 MHz, and the splitting between $3D_{5/2}$ states to be 16.92 MHz which corresponds to the applied magnetic field of $B = 6.72$ Gauss.

A significant requirement on the amplitude of the B field is, that the induced Zeeman splitting should exceed the frequency modulation emerging from the motional modes. In addition, for some particular values of B one has to optimize its magnitude in order to avoid the proximity of transitions corresponding to different σ_+ or σ_- lines, which could become an issue in case that the optical pumping is not set properly, due to the loss of population in advantage of the unwanted σ transition.

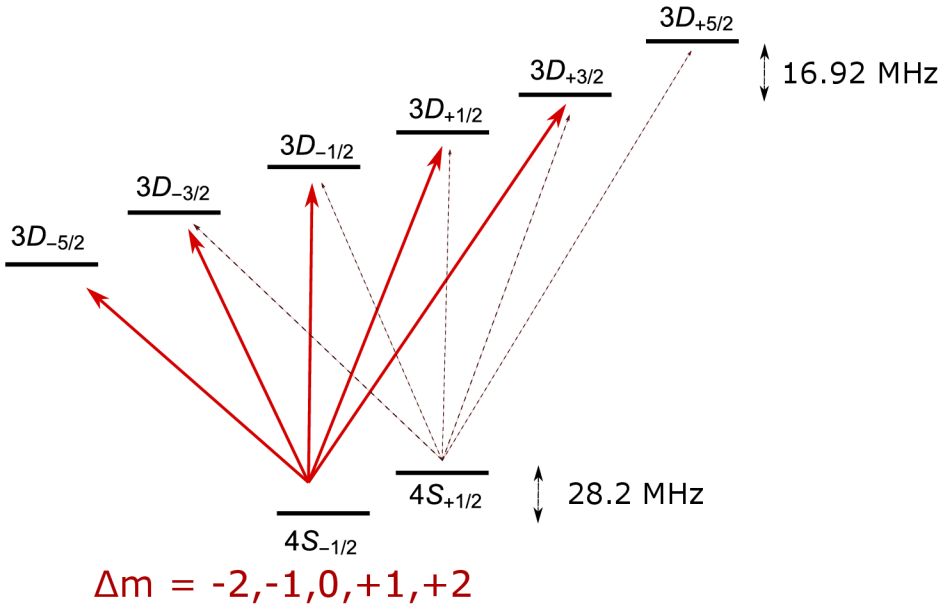

Figure 3.8: Scheme of spectroscopy of quadrupole transition $4S_{1/2} \rightarrow 3D_{5/2}$. Red solid lines depict the addressable transitions for optical pumping set to σ_-, corresponding to the possible $\Delta m = \pm 2, \pm 1, 0$. Alternatively, σ_+ transitions can be measured by setting optical pumping to σ_+, as depicted with black thin lines. The Zeeman splitting is induced with external magnetic field $B = 6.72$ Gauss according to the Eq. 2.35. For the current setting, the frequency splitting between $4S_{1/2}(m = -1/2)$ and $4S_{1/2}(m = +1/2)$ is 28.2 MHz. The $D_{5/2}$ is split into 6 sub-levels differing by 16.92 MHz.

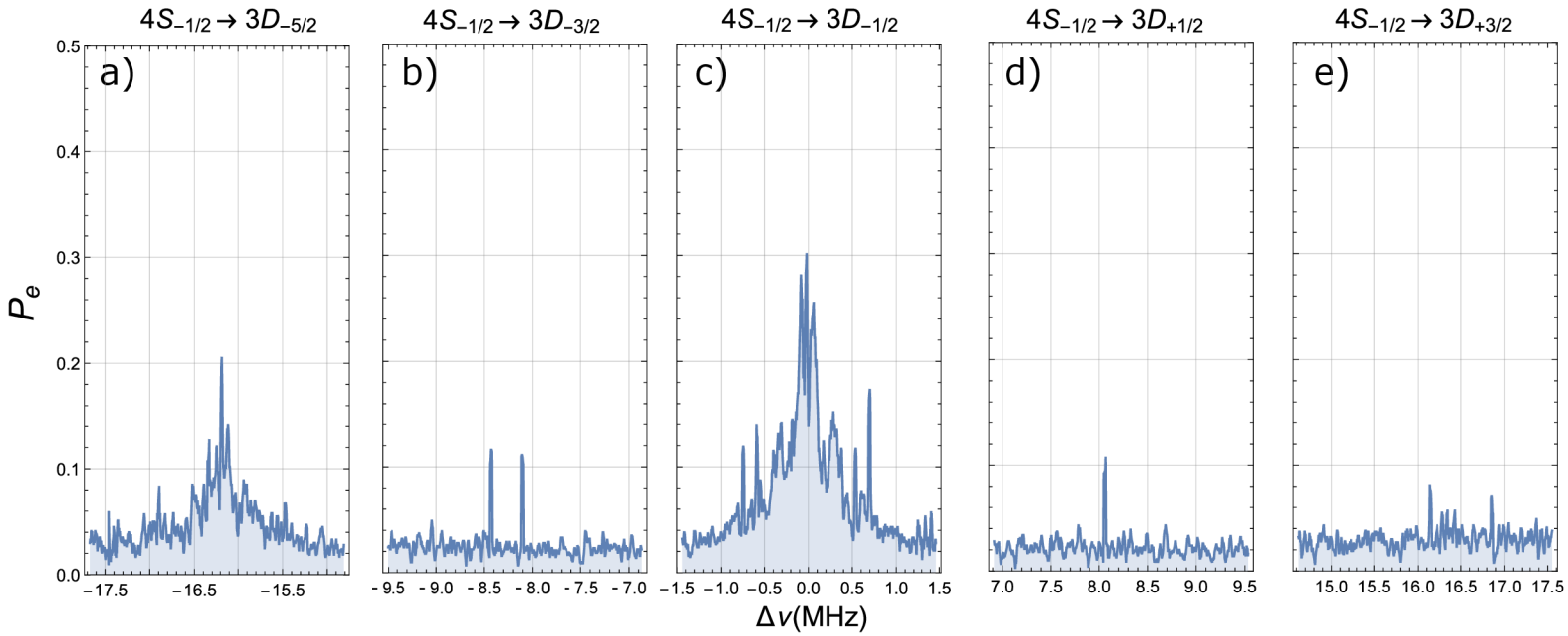

Figure 3.9: Measured spectrum for σ_- states. The configuration of the polarization with respect to the trap axis is set to amplify transitions corresponding to $\Delta m_j = 0, \pm 2$. The strongest central carrier $4S_{1/2}(m = -1/2) \rightarrow 3D_{1/2}(m = -1/2)$ is used for motional state engineering and detection, while the outermost $4S_{1/2}(m = +1/2) \rightarrow 3D_{5/2}(m = -5/2)$ is employed for sideband-cooling. The second transition with $\Delta m_j = +2$ is not effectively addressed, because the carrier frequency lies on the edge of the AOM diffraction bandwidth. The central carrier transition at $4S_{1/2}(m = -1/2) \rightarrow 3D_{1/2}(m = -1/2)$ showed in the plot c) was measured at the AOM frequency 278.43 MHz. The surrounding structure shows axial and radial motional sidebands, which are measured in better detail in the following section 3.7. In subfigures b) and d), the coupling is suppressed, the lines present in figures correspond either to micromotional modulation. We note that, for this particular measurement, we measured offset corresponding to 7 % of ground state excitation. The constant offset came up from the improperly set optical re-shuffling with the 854 nm laser.

3.7 Laser spectroscopy of secular motion

The secular motional modes are imprinted to spectral lines as a frequency modulation of electronic transitions, which makes them directly observable when setting the laser to the correct detuning. The basic condition to distinguish the modulation is the 'sideband resolved regime', where the motional frequency is much higher than the natural decay of the excited state ($\omega \gg \Gamma$). The strength of laser coupling to sidebands is driven by the energy in the motional mode. In Lamb-Dicke regime, the significant coupling occurs for first sideband only, with higher order modes being strongly suppressed.

To successfully measure the oscillatory motion, the vector defining the direction of vibration has to have a significant projection into the direction of the excitation beam. In our experimental configuration, the 729 nm beam is aligned at the angle 45° with respect to the trap axis. This ensures that both the axial and radial oscillations are projected to the plane of the laser and thus they may effectively couple with it. For the measurement presented here, we do not implement the sideband cooling routine, so the initial thermal distribution corresponds to the Doppler cooling limit.

Fig. 3.10 displays the spectrum of the $4S_{1/2}(m = -1/2) \rightarrow 3D_{1/2}(m = -1/2)$. Horizontal axis denotes the laser frequency detuning from the central carrier transition. The vertical points show the resulting probability of the electronic state to be the excited *D*-state. Each point represents a probability reconstructed from a hundred independent measurements.

In Fig. 3.10, the carrier transition is represented with the strongest central line. First axial sidebands are displaced exactly 1.188 MHz apart from the carrier, for the set axial DC potential of 1200 V. The radial motional modes are represented by the highest peaks, at $|\delta| = 2.074$ MHz from the carrier frequency. The small peaks detected closest to the carrier resonance show the beating of the axial and radial mode and the modulation frequency $\nu_{xz} = \nu_x - \nu_z = 0.868$ MHz. We can see the background excitation at the sides to the carrier, which arises despite the attenuation of the excitation laser. With the increasing intensity of the laser beam, the line-shapes tends towards the saturation.

3.8 Sideband cooling

Sideband cooling brings in the possibility to further reduce the energy of the motional mode, typically down to mean energy around $\overline{n} = 0.01$ phonons. It is also commonly denoted as the 'ground-state' cooling, as the mean motional energy of the oscillation mode is already very close to the minimal possible.

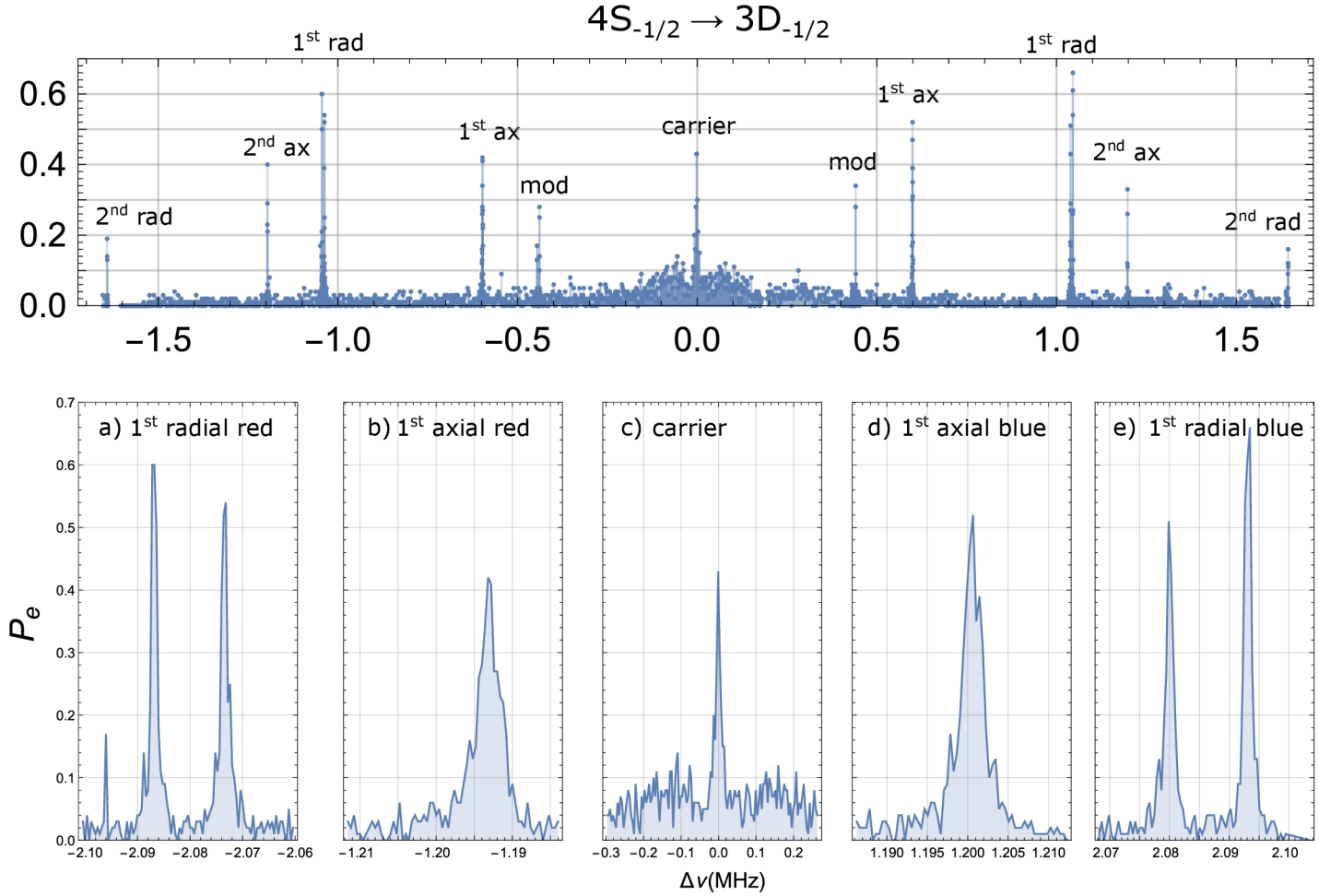

Figure 3.10: Spectroscopy of motional modes measured at $4S_{1/2}(m = -1/2) \rightarrow 3D_{1/2}(m = -1/2)$ transition. The upper figure shows the broad scan of the whole spectrum, including the second radial and axial modes. The lower figure shows the detail of the first order radial and axial sidebands. a) 1st is a radial red sideband, b) 1st axial red sideband, c) carrier transition, d) 1st blue axial sideband, and e) 1^{st} blue radial sideband. The 'mod' label denotes the sideband at the frequency of mutual modulation between axial and radial modes.

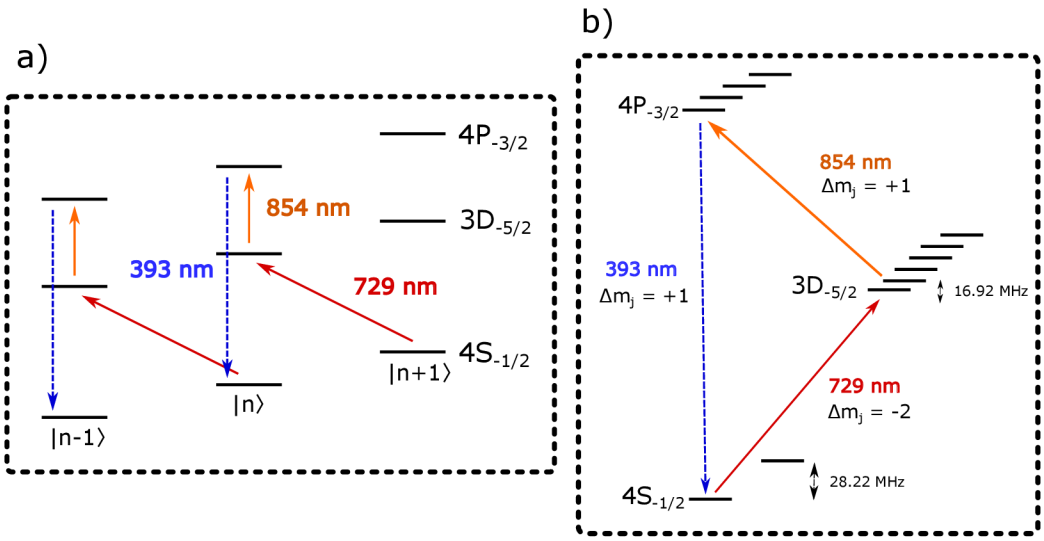

Figure 3.11: A scheme of the sideband cooling routine. a) shows the cooling cycle in the combined electronic-motional level scheme, where the first order axial red sideband is addressed, and b) depicts the loop of the angular momentum change between the Zeeman levels.

Fig. 3.11 depicts the cyclic scheme of the sideband cooling routine. The part in b) shows the dynamics between the Zeeman sub-levels. This is a repetitive loop, starting in the state $4S_{1/2}(m = -1/2)$, following to $3D_{5/2}(m = 5/2)$ with angular momentum change $\Delta m_j = -2$, then to $4P_{3/2}(m = -3/2)$ with $\Delta m_j = +1$, and finally down to the $S_{1/2}(m = -1/2)$ again with the same $\Delta m_j = +1$. Importantly, due to the conservation of total Δm_j and the selection rules on dipole and quadrupole transitions, only scattering down to $4S_{1/2}(m = -1/2)$ level is allowed, preserving the closed cooling cycle. For this type of the cooling loop, the optical pumping pulse in the experimental sequence is set to σ_-. Similar cooling loop can be employed also for σ_+.

The part a) in Fig. 3.11 shows the dynamics of the cooling cycle in motional ladder scheme. We address the red modulation sideband of $4S_{1/2}(m = -1/2) \rightarrow 3D_{5/2}(m = -5/2)$ with 729 nm laser. A coherent transfer of electron into the excited state $3D_{5/2}(m = -5/2)$ leads to the subtraction of the single energy quantum. The lifetime of the excited state is 1.1 s, so the population cannot effectively transfer back to the ground state by the spontaneous emission. The additional laser pulse at 854 nm is employed, which addresses the transition between $3D_{5/2}(m = -5/2) \rightarrow 4P_{3/2}(m = -3/2)$, from where the electron quickly decays back to the $4S_{1/2}(m = 1/2)$ ground state at the wavelength 393 nm.

The biggest limitation of the sideband cooling efficiency lies by the

off-resonant excitation of the neighboring motional transitions from the state $|0\rangle$, which imposes a limit on the minimal mean energy $\overline{n}$ achievable. In case that the sidebands are well resolved, that is $\Gamma \ll \omega$, the cooling efficiency increases and the ion is cooled to the ground state with high probability.

Additional possible issue in the cooling routine lies in the finite probability of the interruption of the loop. One of the reasons originates in the small probability of a spontaneous decay from $4P_{3/2}(m = +3/2)$ level to a lower excited state $3D_{3/2}(m = +3/2)$, which is approximately 6 % [90]. From here, the electron can be reshuffled to the $4P_{1/2}(m = +1/2)$ by 866 nm beam. Finally, from $4P_{1/2}(m = 1/2)$ level, the population may decay into both Zeeman sub-levels $4S_{-1/2}(m = -1/2)$ and $4S_{+1/2}(m = +1/2)$. We employ a short σ_- optical pumping pulse every 1 ms which on average corresponds to the high probability of populating the $4S_{1/2}(m = +1/2)$ state due to this process. The electron scatters back to the $4S_{1/2}(m = -1/2)$ level, and the cycle may continue on. The sideband cooling sequence is technically implemented as a pulse train, where the long pulses consisting of the simultaneous excitation with 729 nm and 854 nm lasers are accompanied by short pulses of optical pumping to σ_-. Figure 3.6 visualizes the experimental sequence.

Typically, in our experimental configuration, the length of the sideband cooling sequence varies from 2 to 4 ms. The achievable occupation of the motional mode after the cooling approaches $\overline{n} = 0.03 \pm 0.01$ phonons. The power of 729 nm laser is increased to 9 mW, which in our experimental configuration corresponds to the carrier Rabi frequency of $\Omega_0 = 2\pi \times (69.7 \pm 0.1)$ kHz. On the contrary, the 854 nm laser is attenuated to the lowest possible intensity which would still reliably implement the repump. The attenuation minimizes the induced AC Stark shift of the excited level caused by the 854 nm beam. In case of frequency shift being too large, the transition is effectively detuned out of the 729 nm resonance. Although this issue can be partially fixed by detuning of the 729 nm frequency, our experience guided us to the limit of very low 854 nm beam intensity. The 854 nm laser frequency is optimized at the reshuffling of the $4S_{-1/2} \rightarrow 3D_{-1/2}$ carrier transition, where the correct frequency detuning is set to reach the best de-population of exited state to the ground state. Typically, the power of 854 nm laser employed in our experiments is set in a range between only 5 to 10 μW.

3.9 Motional state estimation

The motional state readout is based on measurements of the coherent Rabi oscillations, as described in Sec. 2.10. Particularly, the main relevant transition for the presented population distribution estimations is the blue axial

sideband. Additionally, we measure flopping at carrier transition too, in order to experimentally determine the value of Rabi frequency and consequently the Lamb-Dicke parameter. The measured carrier and blue sideband Rabi patterns are fitted with the Eq. 2.39 and 2.40.

In the approximation of thermal states, which result from the Doppler and sideband cooling steps [91], the carrier Rabi oscillation is described with the Eq. 2.39. The measured carrier flops are presented in the Fig. 3.12. For the measurement of the ground state Rabi frequency from carrier Rabi oscillation, we calculate the coarse value of the Lamb-Dicke parameter η_{calc} from the spectroscopically measured frequency of the axial motional mode with use of the Eq. 2.24

$$\eta_{\text{calc}} = \frac{2\pi}{\lambda}\cos(\alpha)\sqrt{\frac{\hbar}{2m\omega_{\text{ax}}}}, \tag{3.1}$$

where $\lambda = 729$ nm, $m = 40 \cdot 1.66 \cdot 10^{-27}$ kg is $^{40}Ca^{+}$atomic mass and $\omega_{\text{ax}} = 2\pi \times 1.188$ MHz is the measured frequency of the axial mode. We also employ the excitation angle $\alpha = \pi/4$ given by the alignment of the 729 nm laser beam with respect to the trap axis., which signifies that the laser beam is aligned at the angle 45° with respect to the trap axis. For this motional frequency, this initial estimation of the Lamb-Dicke parameter value results as $\eta_{calc} = 0.0629$. Estimation of η by measurement is discussed in in Sec. 3.11.

For the fit of the carrier oscillations depicted in Fig. 3.12, we thus assume the η_{calc} as constant, the Rabi frequency Ω_0 as a fitting parameter, and the mean energy $\overline{n}$ as well, which is a term responsible for oscillation damping. From the least-squares fitting method of the Eq. 2.39 into the measured data, we finally obtain the Rabi frequency $\Omega_0 = (2\pi \times 59)$ kHz and the mean energy $\overline{n} = 14.1$ phonons.

Once the values of Rabi frequency Ω_0 and Lamb-Dicke parameter η_{calc} are known, it is possible to directly obtain the phonon number distribution by measurement of the Rabi oscillations on the blue axial sideband. This is described with the Eq. 2.40 as

$$P_e^{\text{bsb}}(\tau) = \frac{1}{2}[1 - \textstyle\sum_n P_n \cos(\Omega_{n,n+1}\tau)e^{-\gamma_n\tau}].$$

For the specific cases, the distribution P_n may be substituted with coherent or thermal statistics. The Rabi frequency scales up with the Lamb-Dicke parameter as $\Omega_{n+1} = \Omega_0\eta\sqrt{n+1}$, and the incoherent decay is represented with element γ_n for each number state, which has been found to scale approximately as $\gamma_n = \gamma_0(x+1)^{0.7}$ [92] (see Sec. 3.14.3). According to the reference [66], the

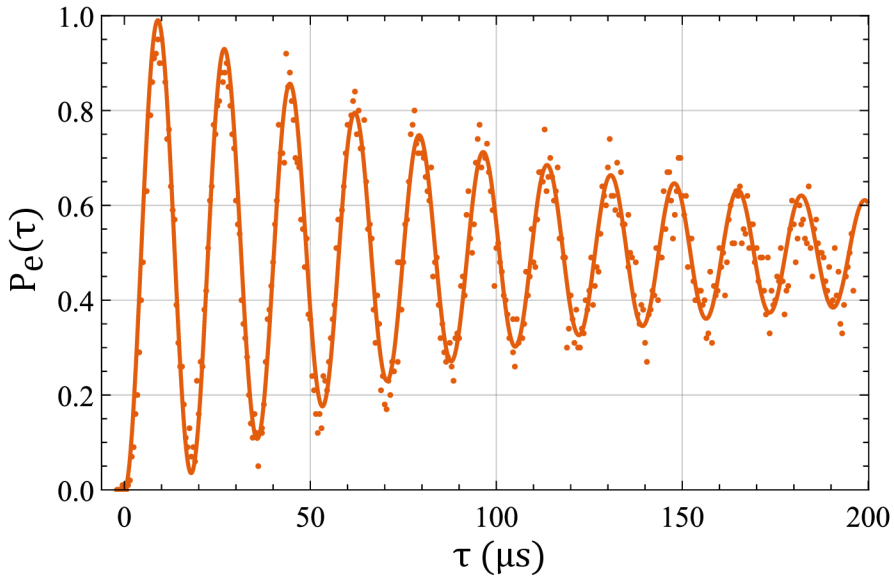

Figure 3.12: Carrier Rabi oscillation at $4S_{1/2}(m = -1/2) \rightarrow 3D_{1/2}(m = -1/2)$ transition for the axial mode being cooled close to the ground state motion. The solid line corresponds to the fit by the Eq. 2.39, with the fitting parameters $\Omega_0 = (2\pi \times 59)$ kHz and $\overline{n} = 14.1$ phonons.

damping is explained by the combination of multiple factors - one of them is the interaction with the surrounding environment where the environmental degrees of freedom are considered entangled with the motional state. The second origin of damping can be attributed to the oscillation of some classical parameter, such as the intensity of the laser or magnetic field noise, which can be also present in systems which are perfectly isolated from the environment.

The occupation of higher motional states causes the increase in the measured Rabi frequency. The ability to prepare these states with high fidelity provides a feasible tool to measure this frequency scaling with unprecedented high accuracy. The statistical distribution of motional state population P_n provides the crucial information about the quantum state, which can be directly used to evaluate the various measures of the non-classical and quantum non-Gaussian features.

3.10 Engineering motional quantum states

The aim of the motional state engineering in this Thesis is to control the phonon number distribution P_n in such way, that we are able to construct a state with desired statistical distribution of interest. We will not consider coherent aspects

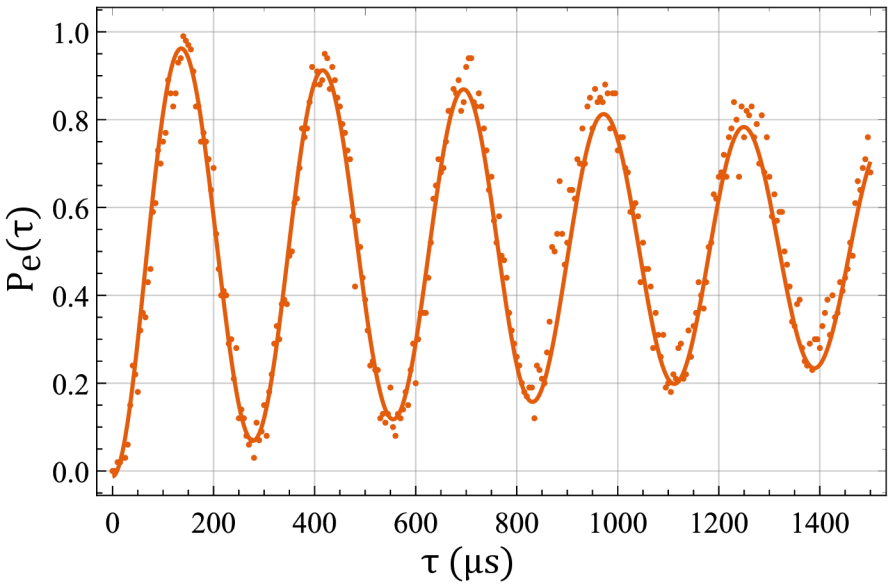

Figure 3.13: Blue sideband Rabi oscillation at $4S_{1/2}(m = -1/2) \rightarrow 3D_{1/2}(m = -1/2)$ transition between the motional states $|g, 0\rangle \rightarrow |e, 1\rangle$, where in the ket state notation $|g\rangle, |e\rangle$ stands for the spin part and states $|0\rangle, |1\rangle$ for the motional degree of freedom. The axial motion is cooled close to ground state, being represented with thermal distribution with measured mean energy $\overline{n} = 0.03 \pm 0.01$ where the uncertainty is calculated from projection noise, see Sec. 3.14.4. The damping factor γ_0 for Fock state $|0\rangle$ was estimated as $\gamma_0 = 2\pi \times (8.9 \pm 0.2)$ kHz. For this measurement, the noise properties are described exclusively with this damping factor γ, unlike for the case of the damped carrier Rabi oscillation, where the decay is contributed to the mean energy $\overline{n}$.

of generated phonon superpositions and focus solely on the phonon number probabilities. The methods to achieve so lie either in setting of the length of Doppler and sideband cooling, leading to generation of classical states with thermal distributions, or by setting the arbitrary combination of carrier and first order motional sideband pulses. We will focus here on basic methods of generation and population reconstruction for thermal and Fock states of motion, and their statistical mixtures resulting from a mechanical thermalization or deterministic nonlinear manipulations of thermal states.

3.10.1 Thermal states

A thermal state of motion can be simply achieved by laser cooling. Statistics of phonon populations P_n after cooling typically obeys the Bose-Einstein thermal distribution [19, 58, 91] written as

$$P_n = \sum_n \frac{\overline{n}^n}{(\overline{n}+1)^{n+1}}. \tag{3.2}$$

which is characterized with a single variable $\overline{n}$ denoted as mean energy. The amount of mean thermal phonon population $\overline{n}$ can be tuned by length of the sideband-cooling sequence in the state preparation step. In this way, the energy may be tuned from a close-to ground state, up to the Doppler cooling limit. Particularly, for our experiment, the scope lies between $\overline{n} = 0.03$ up to $\overline{n} \approx 8$.

The characterization of the thermal motional distribution shrinks to the aim of finding the mean energy $\overline{n}$ and confirmation of the thermal character of the observed photon probability distribution. There are various methods to achieve so, including comparison of couplings to red and blue sidebands [19, 93], measuring of the strength of motional coupling with respect to the carrier transition [48], or measuring the spatial and coherence properties of emitted light. They include the implementation of thermometry based on the optical spatial resolution of ion wavepacket [94], or related optical interferometric schemes [86]. However, for thermal state energy which is close to the Doppler cooling limit and lower, and in tight trapping potentials corresponding to motional frequencies on the order of a few MHz, the most convenient way of characterization is a direct fit of Rabi oscillations with the Eq. 2.40.

We discuss two different methods to fit the population distribution of thermal states. For the bare estimation of the mean phonon population on the state, which can be apriori expected to be in a thermal, i.e. Bose-Einstein phonon number distribution, it becomes sufficient to employ the predetermined relation between the relative weights of P_n and merely use the mean phonon number $\bar{n}$ as the fitting parameter. We thus insert the Bose-Einstein probability distribution in Eq. 3.2 directly to the fitting function. (Eq. 2.40). Fitting only the single parameter $\overline{n}$ largely simplifies the estimation. The main source of imperfections of this routine lies in the fact that the actual distribution is never perfectly thermal. The small deviation from the motional population could originate mainly from the assumption of idealized cooling dynamics, which, however, can be disturbed by the presence of different excitation scenarios and corresponding parametric nonlinearities in the system. [95]. In addition, small intensity fluctuations of the employed Doppler cooling laser, and detection projection noise unavoidable for the finite number of measurement repetitions, result in the deviations from the thermal distribution, which do not perfectly match the simplified model of thermal oscillator.

For this purposes, we often prefer to employ the estimation of probability phonon distribution without any assumption about its statistics. We compare these two estimation methods when applied on same set of data, and present

the results in Fig. 3.14. There, the first plot with blue line depicts the results from direct probability estimation, on the data set resulting from 100 repetitions of the sequence in each point of the measured Rabi oscillation. The second method shows the statistical estimation based on the fit with a single fitting parameter $\bar{n}$. The comparison shows that in the limit of many experimental repetitions, the direct fit of the motional populations returns the similar results as the method which utilizes only the mean energy of the thermal state as a single fitting parameter. The method of direct estimation of populations is preferred for measurements in the scope of this work, due to it's applicability beyond the set of thermal states only.

For our experiment, the typical energy achieved after the optimization of mutual detuning of 397 nm and 866 nm lasers and their intensities, the estimated energy of a single ion after the Doppler cooling limit was corresponding to as $\overline{n} = 8.0 \pm 1.0$ phonons on axial mode. The corresponding measured Rabi flops are depicted in Fig. 3.15, including the estimated probability distribution, compared to the ideal Bose-Einstein statistics derived from the fitted $\overline{n}$.

3.10.2 Number states

There are various methods which can be implemented for the number state generation, such as accumulation of motion from repetitive anti-Jaynes interaction [34, 96], rapid adiabatic passage [24], or implementation of reservoir engineering [97]. The most understood method corresponds to the iterative excitation of the Jaynes-Cummings (JC) and anti Jaynes-Cummins (anti-JC) interactions, implemented on blue and red axial sidebands. This method is reliable, convenient to implement, and previously provided experimental demonstrations of low number states with very high deterministic population of desired $|n\rangle$.

However, the necessary condition to be fulfilled is the ability to minimize the initial population entropy which is typically approached by initialization of the ion in the motional ground state $|g, 0\rangle$. In our experiment, we could systematically reach the population of $|g, 0\rangle$ as $P_0 = 0.97 \pm 0.02$, which corresponds to mean number of phonons $\overline{n} = 0.03 \pm 0.01$. The corresponding Rabi oscillation for 1^{st} motional blue sideband at transition $|g, 0\rangle \rightarrow |e, 1\rangle$ has estimated Rabi frequency $\Omega_0 = (2\pi \times 71)$ kHz.

For the transition $|g, 0\rangle \rightarrow |e, 1\rangle$, we define the experimental π-pulse as a measured duration τ, for which the maximal amount of population is transferred to the excited state. For the particular Ω_0, this has been estimated as $\pi_0 = 112\ \mu$s with the measured efficiency of population transfer between P_0 to P_1 being close to 0.99.

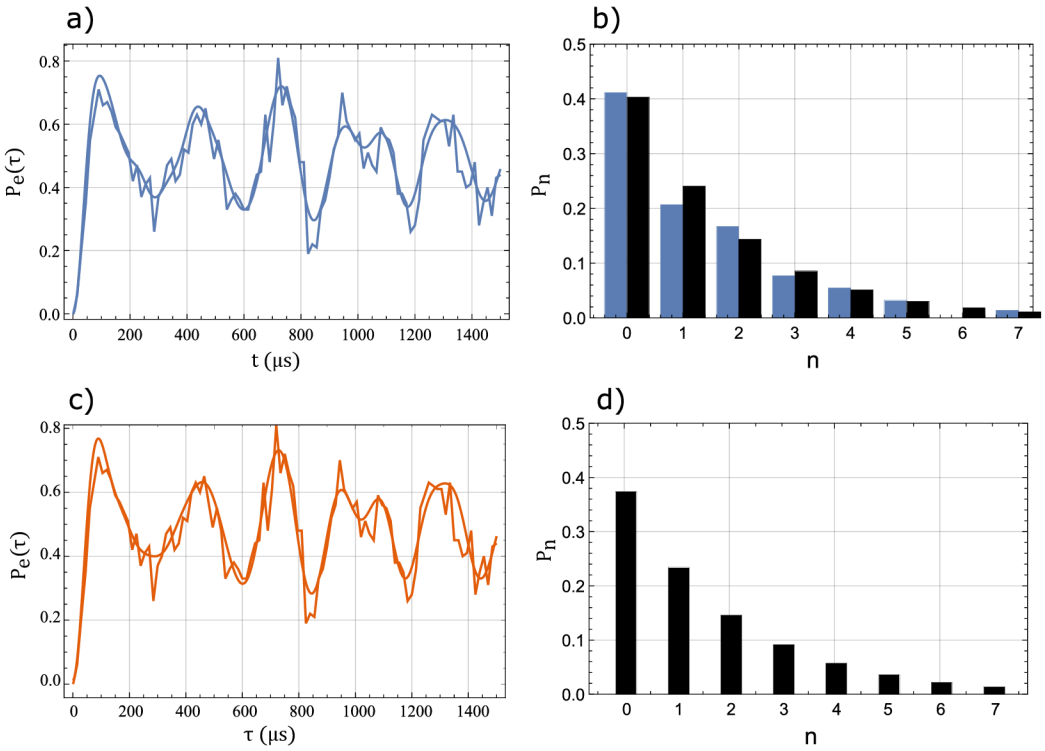

Figure 3.14: Comparison of two different fitting methods to measure the mean energy of axial motion in thermal state. Figures a) and b) show fit and the results by the method which employs direct reconstruction of the states' probabilities from least squares fit of the Eq. 2.40. The resulting distribution is then fitted with Eq. 3.2, returning the mean energy $\overline{n} = 1.5 \pm 0.2$, with the error resulting from five independent measurement. Black columns in b) show the ideal thermal distribution modeled for corresponding $\overline{n} = 1.5$. The fidelity between this Bose-Einstein probability distribution with the same $\overline{n}$ and the distribution estimated from a full fit of P_n is 96.5 % [47]. The upper limit on the probability sum in Eq. 2.40 was set to $n_{\max} = 7$, above which the remaining population of the thermal state is expected to be less than 1 %. Figures c) and d) show the fit by the thermal distribution, when $\overline{n}$ is taken as a single parameter, resulting to the mean energy $\overline{n} = 1.67$. Both methods return the result which are equivalent within the estimated error bar.

The experimental sequence for generation of the previously observed low number states $|g,1\rangle$ and $|g,2\rangle$ goes as following. We experimentally determine the exact length of the π-pulse by scanning the pulse duration in order to reach the most effective excitation to the $|e,1\rangle$ level. Next, the π-pulse on carrier transition transfers the population back to the ground state of two level system, $|e,1\rangle \rightarrow |g,1\rangle$. In the last step, we apply a 854 nm quenching pulse, which serves

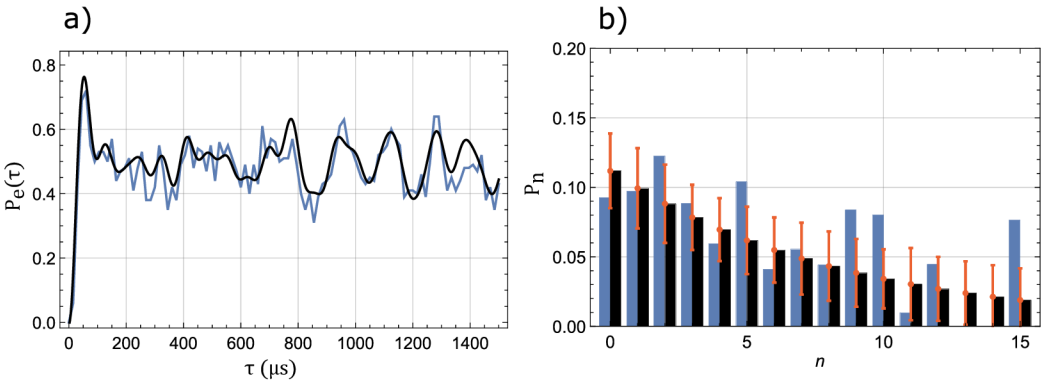

Figure 3.15: a) Blue sideband transition $4S_{1/2}(m = -1/2) \rightarrow 3D_{1/2}(m = -1/2)$ at axial motional mode measured at the limit of Doppler cooling, which is the initial state before application of the sideband cooling step. The state is prepared by application of 1 ms of Doppler cooling sequence step (see Fig. 3.6). The mean phonon number is estimated $\overline{n} = 8.0 \pm 1.0$. Blue trace presents the measured data, black is the fit from Eq. 2.40 with measured $\overline{n}$. b) shows the corresponding measured population (in blue), and theoretically estimated one (black), for the measured curves displayed in a). Fidelity of the populations from the full p_n fit with respect to theoretical was estimated as 78.5 %. The red error bars correspond to one standard deviation, which is evaluated for each population with use of the Monte-Carlo simulation method (see Sec. 3.14.4), assuming the projection noise from 100 population measurements on the two-level system. The resulting uncertainty of each population varies between ±2.2 % to ±2.9 %, with the average value ±2.4 %. Comparison of measured data with these uncertainties shows that most of the values fall into to the interval defined by single standard deviation of the ideal value for corresponding thermal state, which implies that the Monte-Carlo estimation proves itself as a good method to estimate the uncertainty in case that it is not possible or convenient to perform repetitive measurements.

to eliminate the residual population of the state $|e, 1\rangle$, which is typically much below 5 %. We also apply a short optical pumping pulse at σ_- at 397 nm to suppress the accumulation of the population in the $4S_{1/2}(m = +1/2)$ level, which can arise from the improbable $4P_{3/2}(m = +3/2) \rightarrow 3D_{3/2}(m = +3/2)$ decay.

In order to generate higher order Fock states, one may choose the method which extrapolates the sequence for the generation of $|2\rangle$, that is, iterative excitation of blue and red sidebands with pulse lengths corresponding to π pulses. In order to end up in the ground state of the electronic transition, the last pulse for the odd number state is the carrier π pulse, or a red sideband π pulse for even Fock states, respectively.

In Fig. 3.16, we plot the Rabi oscillations for generated Fock states $|1\rangle$ and $|2\rangle$. The frequency of the oscillation increases by the factor $\sqrt{n+1}$, which leads

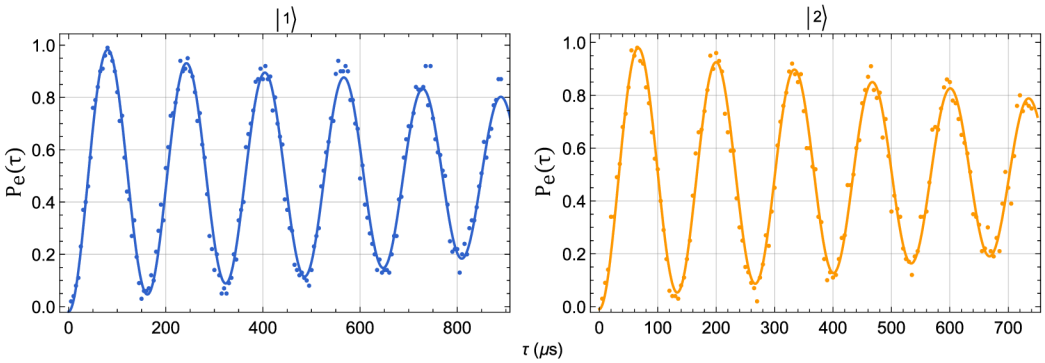

Figure 3.16: Fock states of motion at axial mode up to order $|2\rangle$, generated by the method of alternate application of blue and red sideband π pulses. The ground state Rabi frequency for this measurement was measured for ground state as $\Omega_0 = (2\pi \times 71)$kHz. For these values the populations of the measured number states was $P_1 = 0.96 \pm 0.02$ for state $|1\rangle$ and $P_2 = 0.98 \pm 0.02$ for state $|2\rangle$. The increase of motional number for the measured oscillations is manifested by the higher Rabi flopping frequency.

to shortening of the corresponding oscillation period. In order to maximize the amount of population transferred between the $|g, n\rangle \rightarrow |e, n+1\rangle$ states (or between $|e, n\rangle \rightarrow |g, n+1\rangle$ states), the duration of the π pulse is optimized experimentally by scanning the pulse duration. This is important due to the time offset of the RF pulse generated by the programmable pulse sequencer, which in our case slightly varies depending on the complexity of the pulse sequence. Also, the oscillation damping and loss of contrast slightly shift the position of the pulse maximum. he experimentally measured π pulses differ from theoretically estimated lengths by $\pm 5\ \mu s$.

3.11 Estimation of the Lamb-Dicke parameter

For initial estimation of the carrier Rabi frequency and damping it is possible to employ the coarse value of the Lamb-Dicke parameter η, which was calculated from the spectroscopically measured frequency of the given motional mode with use of the Eq. 2.24. Once the motional ground state cooling is achieved in the experiment, η can be also precisely experimentally estimated from the comparison of the Rabi frequencies on the first blue motional sideband and on the carrier transition. In case that the mean energy $\bar{n}$ is zero, the carrier Rabi oscillations given by the Eq. 2.38 should become independent on motional coupling, and thus they should not be affected by the Lamb-Dicke parameter η. The measurement of the carrier Rabi oscillation then provides the Rabi frequency Ω_0. The oscillations on first blue motional sideband then allow for a

direct estimation of Lamb-Dicke parameter without any prior knowledge of the trapping parameters, like motional frequency or corresponding laser excitation parameters. Note that by definition, the estimated Lamb-Dicke parameter is always related exclusively to the given excitation laser frequency and direction with respect to the particular normal mode of ion's motion.

The measurements of carrier and blue sideband Rabi oscillations after ground state cooling are shown in Fig. 3.17. The measured oscillation pattern always appears damped even for ground-state cooled motion, with decay caused by the residual population in radial modes, which were not ground-state cooled in this sequence. Additionally, the damping can be typically caused by the intensity fluctuations of the employed laser beam, however, after implementation of the precise sample and hold stabilization of the 729 nm laser intensity at the input to the vacuum chamber, we did not observe any significant contribution of this kind.

Since we have to assume the damping in the fit, we fit the carrier oscillations by the Eq. 2.39, where we assume the preliminary value of $\eta = 0.0629$ together with the mean energy $\overline{n}$ taken as a variable, resulting into $\overline{n} = 14.1 \pm 0.2$ phonons.

In the second step, we apply a sideband cooling method and reduce the axial motion close to the ground state. The corresponding Rabi oscillation on the blue sideband is then described with use of the formula 2.40, with η and γ now serving as fitting variables. We again employ five independent measurement runs, returning the final value of $\eta_{729} = 0.0611 \pm 0.0002$, and the damping $\gamma_0 = 2\pi \times (8.9 \pm 0.2)$ kHz.

3.12 Motional heating on axial mode

Motional heating is a process which is manifested as a gradual increase of the energy in the motional mode over the time of the measurement. The main origin lies in the fluctuation of electric fields inside the trap, which couple to the motional charge [90, 98]. Alternatively, the ion may be heated by the photon scattering on the dipole transition. In the first case, the ion heats up to the limit of energy of surrounding environment, in the latter, the ion will over time reach the energy of the limit for Doppler cooling.

To measure the heating rate, the cooling is set close to the ground state of motion. We insert the time delay interval between the state preparation and state detection step into the experimental sequence, which is between 10 ms and 250 ms (see Fig. 3.6). While varying the duration of the time gap, we are able to determine the amount of thermal heating acquired by the ion during the corresponding time period. The resulting energy is obtained from a statistical distribution, which is again extracted from a fit of the blue sideband

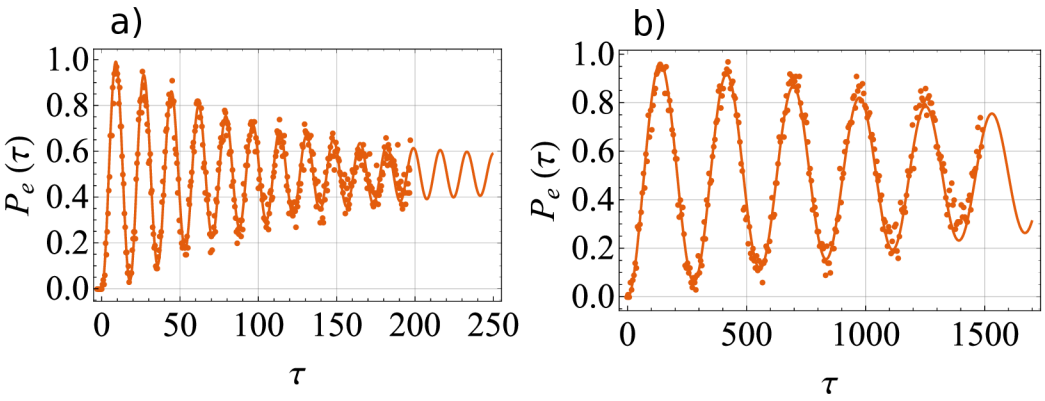

Figure 3.17: Measured Rabi oscillations at a) carrier and b) blue sideband to determine the Lamb-Dicke parameter. For each estimation, in total five similar measurements under the same experimental conditions were performed. From a), we have obtained $\Omega_0 = 2\pi \times (58.9 \pm 0.1)$ kHz, and $\overline{n} = 14.1 \pm 0.2$, from the fit of the BSB Rabi oscillations presented in b) we retrieve the experimentally determined value of $\eta_{729} = 0.0611 \pm 0.0002$ and $\gamma = 2\pi \times (8.9 \pm 0.2)$ kHz.

Rabi oscillation.

Fig. 3.18 shows the Rabi oscillations of initial close-to ground state, and thermal state after 250 μs of heating, which represents the maximal waiting time set in the heating rate measurement. The similar measurements have been made for time differences ranging from 50 μs to 250 μs with 50 μs steps. The amount of heating acquired by atom for each time interval is plotted in Fig. 3.19. From a linear dependence of the axial heating rate, we deduce the resulting change of energy as $\Delta\overline{n} = 2.7 \pm 0.2$. The measured amount of heating is further used to characterize the source of imperfections for generated complex motional mixtures, and their comparison with theoretical simulations.

3.13 Heating by random photon recoils

Significant, but to a large extent controllable source of motional heating in presented experiments originates from the interaction with excitation lasers in the sideband unresolved regime. This happens particularly in the processes of reshuffling of the excited state $4P_{1/2}$ or in the optical pumping. The certain amount of population in prepared motional quantum state is always lost in credit of the neighboring number states with the probability proportional to the square of the Lamb-Dicke parameter η^2.

We measure the recoil heating experimentally, as depicted in Fig. 3.20. The

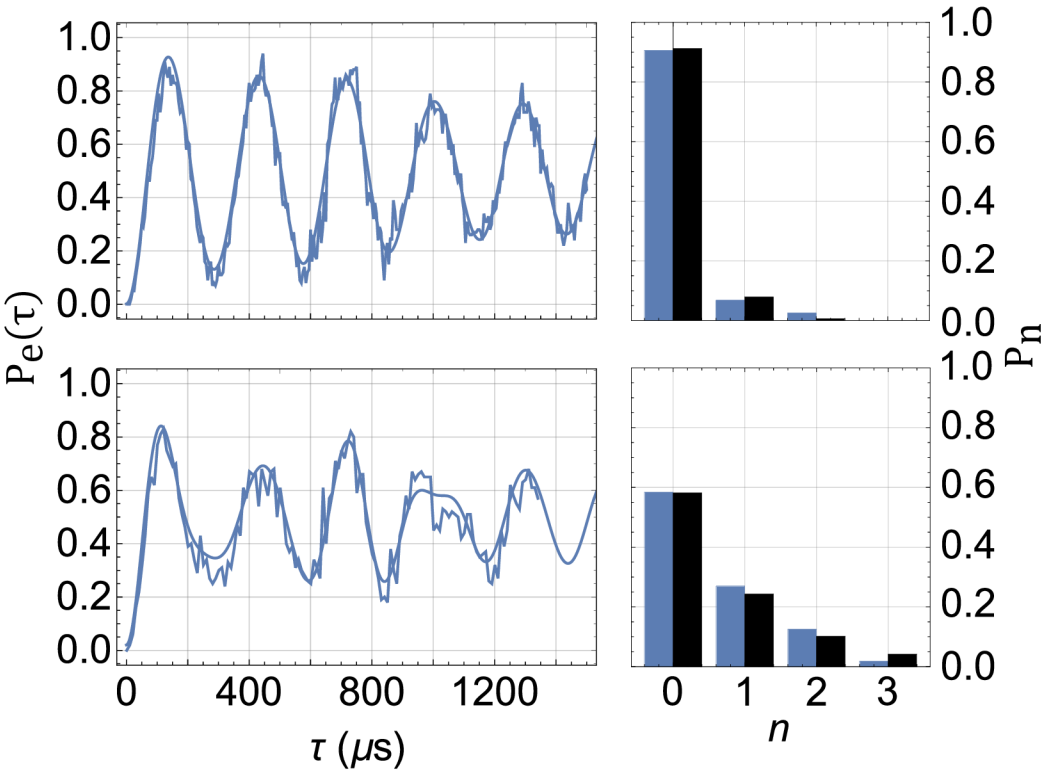

Figure 3.18: Axial heating rate measurement. Upper part of the figure shows the initial thermal state with mean energy $\overline{n} = 0.09 \pm 0.01$ phonons with corresponding statistics. b) is a developed state after 250 ms waiting time, with estimated $\overline{n} = 0.72 \pm 0.05$. Blue columns show reconstructed populations, black columns are thermal distributions corresponding to the measured mean energy $\overline{n}$.

experiment starts in ground state of motion of axial mode and the two-level system. We apply the carrier π-pulse to transfer the maximal amount of population to the excited state ($|g,0\rangle \rightarrow |e,0\rangle$), where we apply re-shuffling at 854 nm. Before the detection step, we also add the 5 μs optical pumping pulse. At this point, certain amount of population proportional to η^2 transfers into the neighboring energy level $|g,1\rangle$. We implement five sequential repetitions of this 'carrier' $\rightarrow$ 'reshuffling' $\rightarrow$ 'optical pumping' pulse sequence, and after each iteration, we investigate the change of the population distribution with respect to the previous iteration. In the limit of a single experimental reshuffling cycle, the effective Lamb-Dicke parameter η^2 can be estimated, which correspond to

$$\eta^2 = \Delta P_1 / P_0, \tag{3.3}$$

with $\Delta P_1 = P_1^{\text{out}} - P_1^{\text{in}}$ denoting the population acquired into the state P_1 during

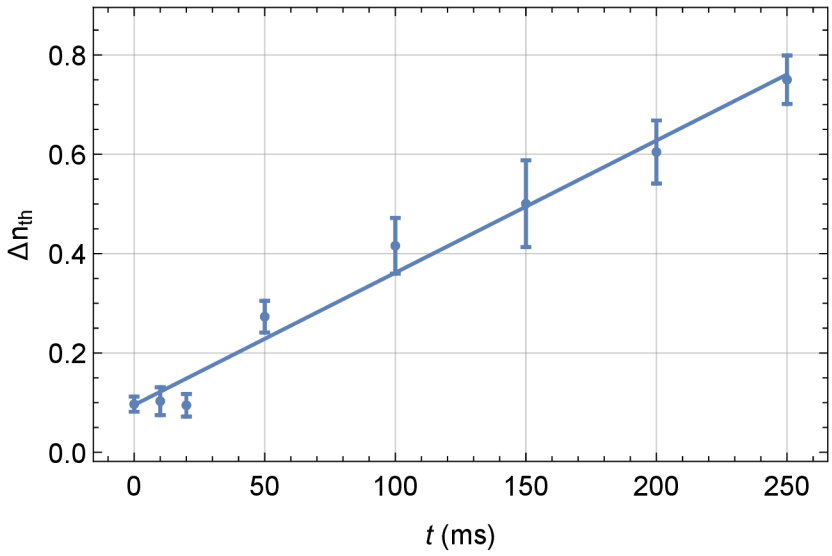

Figure 3.19: Axial heating rate measurement. The amount of acquired mean thermal energy Δn_{th} is showed as a function of delay set into the experimental sequence. From a linear fit, we estimate the axial heating rate as $\Delta\overline{n}$ = 2.7 ± 0.2.

the heating, which is normalized on the population in the lowest level, initially being close to the ground state. After five heating steps, we estimate the average $\eta^2 = 0.029 \pm 0.002$, where the uncertainty corresponds to a single standard deviation, meaning that approximately 2.9 % of P_0 is transferred due to heating. As depicted in Fig. 3.20 c), the initial state $P_0 = 0.92$ is reduced after two heating cycles to $P_0 = 0.85$, and after six steps the population drops to $P_0 = 0.75$.

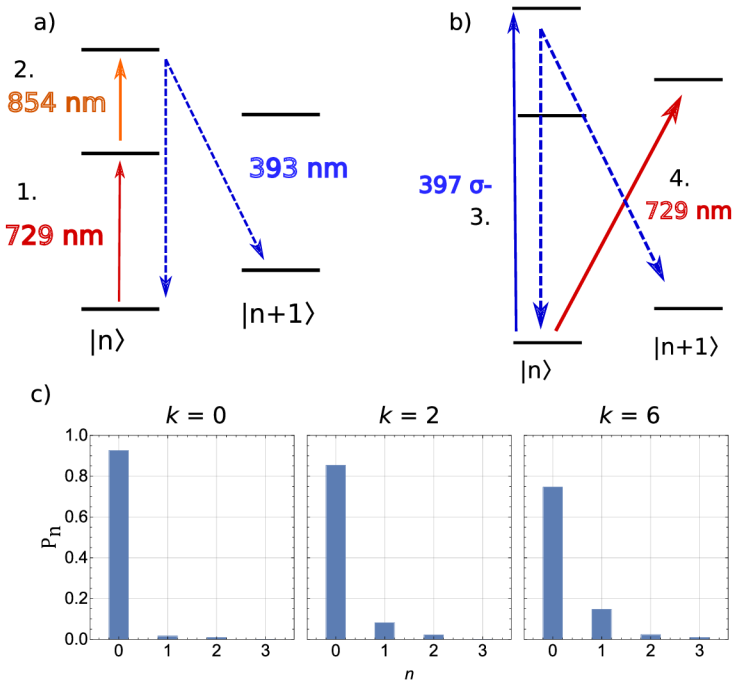

Figure 3.20: Illustration of the estimation of the heating rate due to photon recoils in the processes of optical re-shuffling (a) and optical pumping (b). The excitation of the two-level system with 729 nm beam (1.) and 854 nm (2.) light is followed by the spontaneous emission of a 393 nm phonon back to the $4S_{1/2}$, which may cause the addition of the motional quantum. Similarly, this can happen also after excitation of σ_- transition (3.). Finally, the state is probed and measured with 729 beam tuned to the first blue sideband (4.). c) shows the results of the measurement, for initial state with k = 0 iterations, then for k = 2 and k = 6 iterations. The measurement results into the value $\eta^2 = 0.029 \pm 0.002$.

3.14 Approximations for reconstruction of motional population

The following considerations are be related to the Rabi oscillations on the first blue motional sideband using the Eq. 2.40.

$$P_e(\tau) = \frac{1}{2}[1 - \sum_n^{n_{max}} P_n \cos(\Omega_{n,n+1}\tau) \exp(-\gamma_n \tau)].$$

We discuss the necessary conditions to be considered in the fitting routine, in order to return estimated populations which would be closest to the experimentally implemented state. We investigate the effect of constraints on fitting parameters, particularly the truncation of the probability sum,

then normalization of the resulting statistics, measuring scaling of damping coefficient with motional population, and calculation of error estimate with the Monte-Carlo methods.

3.14.1 Truncation of motional state distribution

The Rabi oscillation on the blue motional sideband described by the Eq. 2.40 consists of sum over the statistical distribution $\sum_{n=0}^{\infty} P_n$. Practically, the sum has to be truncated at certain maximal population denoted as $n_{\max}$. The selection of the sum maximum may impact the final distribution of probability. In particular, for the states with low motional energy and populations concentrated in several lowest n, the inclusion of very high n typically increases the noise and probability of population of high n, mainly due to their high oscillation frequencies which become more similar to the sampling rate of the oscillations. On the other hand, truncation at too low n can obviously deform the observed statistics by impossibility to resemble the population of higher phonon numbers.

We run a simulation of the population fitting on states with various thermal energies. In the first step, we generate the Rabi oscillation pattern for thermal state with mean $\overline{n}$ the and the sum maximum $n_{\max} \to \infty$. In the second step, we fit that Rabi oscillation with the Eq. 2.40 where the truncation parameter $n_{\max}$ is set as a variable. Finally, in the third step, we fit the resulting distribution with the Eq. 3.2 describing a thermal motional state and project the resulting $\overline{n}_{\text{fit}}$ as a function of the original set $\overline{n}$. The Fig. 3.21 shows the deviation from the optimal fit result for various $n_{\max}$ and $\overline{n}$, which is very high for the low values of $n_{\max}$ and gradually decreasing with increasing $n_{\max}$.

The final value of $n_{\max}$ for the fit is then considered as a value, whose probability does not exceed $P_n^{\max} = 0.01$ for a thermal state with the same energy as for the state under investigation. The whole process for the unknown motional state thus goes as following. At first, we set the $n_{\max}$ much higher than expected for measured state. The population distribution is fitted with the Eq. 2.40. We calculate the mean motional energy as $\overline{n} = \sum_n nP_n$. Then, we simulate the Rabi oscillation with motional thermal distribution P_n defined with the Eq. 3.2, fit it again with the Eq. 2.40 and select such a value n_{max} where $P_n^{\max} < 0.01$. In Fig. 3.24, the selected values are marked with black arrows.

As an example displayed in Fig. 3.24, we investigate the initial thermal state with mean energy of about $\overline{n} = 1.5$, with the theoretical population $p_7 = 0.011$ and $p_8 = 0.007$. In this case, we set the $n_{\max} = 7$, since it is the last element obtaining population higher than 1 %. Additional example is thermal state with energy close to the Doppler limit, which is approximately $\overline{n} = 7$. Now, the sum is truncated at $n_{\max} = 18$, with $p_{18} = 0.011$, where $p_{19} = 0.01$. Similarly, this

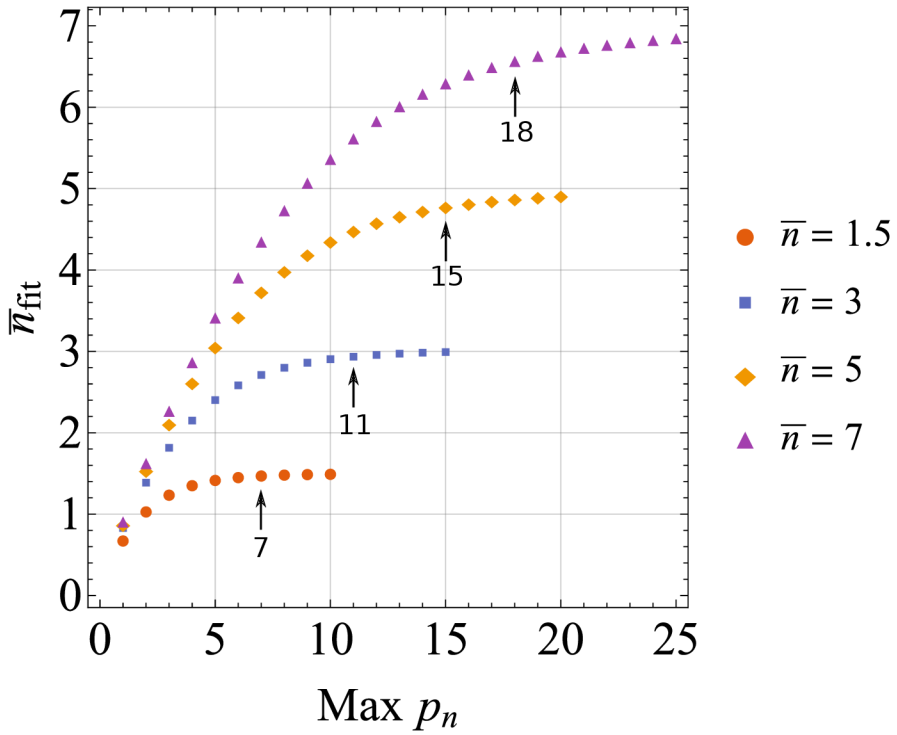

Figure 3.21: Illustration of the effect of sum truncation for fits of ideal thermal states. The y axis shows the mean energies resulting from fits of Rabi oscillations for ideal thermal states $\overline{n} = 1.5$, 3, 5, and 7, which are plotted as a function of set maximum of the probability sum $\sum_{n=0}^{n_{max}} p_n$. The resulting trends show that setting of a low maximum leads to under-estimation of the resulting energy. The black arrows denote the highest number states, which contain more than 1 % of the total population. These number states are thus used to set n_{max} in the fitting equation.

is applied also on states with $\overline{n} = 3$ and $\overline{n} = 5$ where $n_{\mathrm{max}} = 11$ or $n_{\mathrm{max}} = 15$, respectively.

3.14.2 Population normalization and fitting constraints

Since the $\sum_n P_n$ describes the actual probabilities of number state occupation, we expect the results to be positive and the sum of the probabilities to be normalized to 1. Generally, the completely unconstrained fit would be the most numerically accurate, but the outputs will not comply with the physical constraints [99]. We test different settings of fitting constraints to the Eq. 2.40 and in order to find the fitting routine which returns most reliable outcomes.

We illustrate the effect of the reconstruction precision on the measurement

of the thermal motional state with mean energy $\overline{n} = 3.0 \pm 0.4$ phonons (see Fig. 3.22 a). The data were taken with a 100 repetitions per the measurement point, and the time difference between data points is 10 μs. The maximum of the probability sum is set as $n_{\max} = 13$, following the truncation condition described in previous Sec. 3.14.1. We test four settings of constraints on the least-squares method, as described in the Table 3.2. For each of the routines, we investigate the probability sum, and also the mean absolute error (MAE), defined as

$$MAE = \frac{\sum_n |P_n^{\text{meas}} - P_n^{\text{th}}|}{n}, \tag{3.4}$$

which tests the fit accuracy by returning average value of residuals between the measured population and the idealized thermal state distribution, where the lowest value shows the best numerical accuracy. The results of the fitting routines and their comparison with the idealized state are depicted in Fig. 3.22 b).

Method	constraints	$\sum p_n$	MAE
1	none	0.987	0.0269
2	$0 < p_n < 1$	1.005	0.01805
3	$\sum p_n = 1$	1	0.01802
4	$0 < p_n < 1, \sum p_n = 1$	1	0.01792

Table 3.2: Table of tested settings of fitting constraints. The second column denotes the constraints applied directly to the fit. 1st setting represents the unconstrained direct fit, 2nd the condition on the probability positiveness, 3rd the constraint on the probability sum. The final 4th most accurate method combines both steps from 2 and 3, where only first is applied as a direct least-squares constraint, and the second is achieved in weighted normalization after the fit. MAE stands for the mean absolute error from Eq. 3.4, where lowest value shows fit with the best physical validity.

At first, we assume a simple unconstrained model. In the second approach, we make a simple general assumption that the probability should be greater or equal to 0 and the single probability should be smaller or equal to 1. In the third method, we force in the condition that the sum of all probabilities should be equal to 1. Finally, in fourth approach, we take the conditions similar to the Method 2 and normalize the sum of the resulting probabilities to 1.

From the comparison depicted in Fig. 3.22 b), we see that all the methods perform well for populations having at least 3 % probability. Beyond that, the unconstrained model often returns the nonphysical outputs corresponding to negative probabilities. Even though the method gives the best possible values for the least-squares fit, the results have the lowest correspondence with the ideal distribution, as can be seen from it's MAE value being higher than for

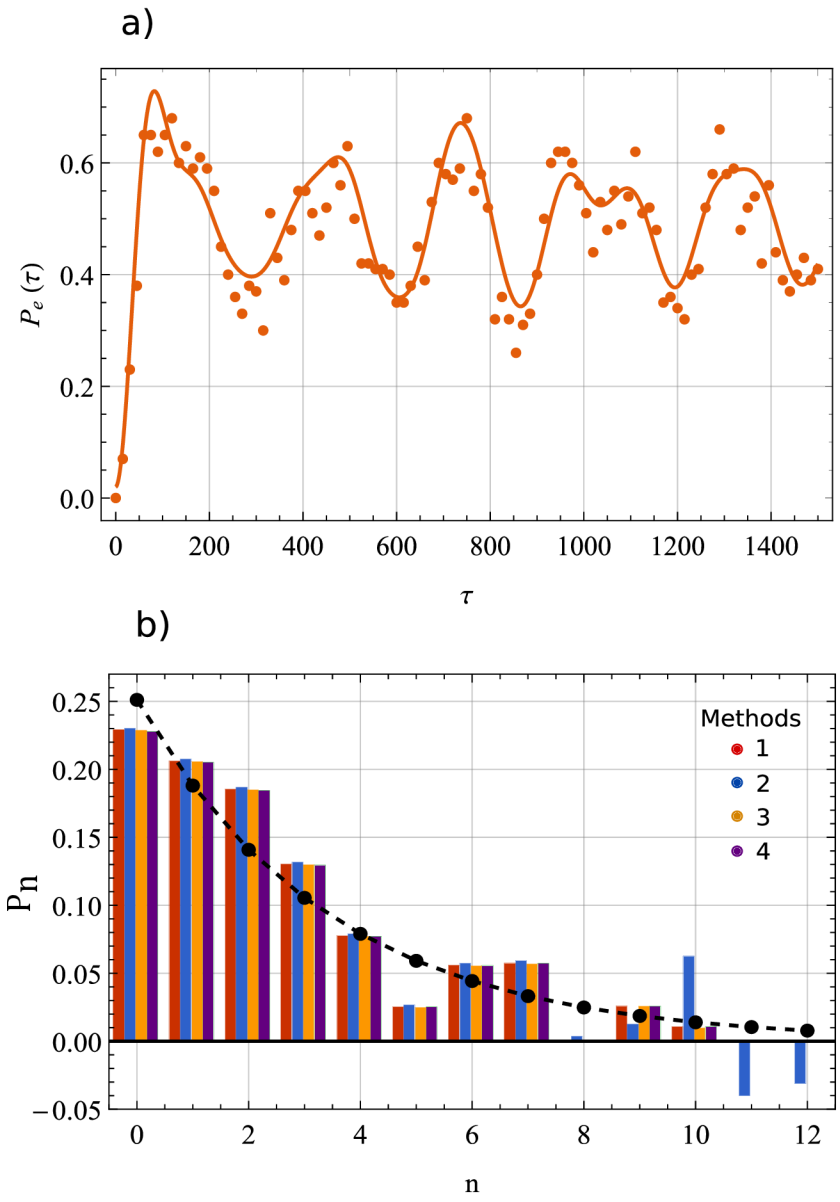

Figure 3.22: Test of the constraints for the fitting method. a) shows the Rabi oscillation corresponding to thermal state with measured $\overline{n} = 3.0 \pm 0.4$ phonons on the first blue axial sideband. b) shows the fits by Eq. 2.40 with various settings of fitting constraints, where the black points show the expected ideal populations. The properties of the methods are written in Tab. 3.2. For our experiment, we use the 4^{th} method, which constraints each probability to be $0 < p_n < 1$, and then utilizes the weighted normalization of resulting probabilities to sum to 1.

other employed routines. From here, we infer that at least some constraints on probability distribution are needed.

The 3rd fitting method assuming the constraint on probability sum performs well in this particular case, there is however a probability of returning the negative state populations as well. We have empirically experienced around 10 % of random failure while estimating arbitrary motional state. This also gives rise to additional problems in the Monte-Carlo uncertainty estimation routine (described in 3.14.4), leading to artificial increase of the error bar due to the failed estimations. This can be overcome by implementation of additional condition for positivity of the parameters, which however further decreases the numerical accuracy.

Finally, it appears that the optimal solution is to use the 4th method. The residual statistical population is redistributed to the motional states with use of the weighted average, meaning that the highly populated levels will be more affected. The evaluated MAE is the least of all four implementation, while at the same time the physical constraints on the probability positivity and normalization are conserved.

3.14.3 Damping in Rabi oscillation

All Rabi oscillation measurements in our experimental setup are subjected to decay, where in the limit of long probing times the oscillatory pattern converges to incoherent mixture of $|S\rangle$ and $|D\rangle$ states. In the employed fitting model corresponding to the Eq 2.40, we accounted for this effect with use of the exponential decay parameter γ_n. In the measured Rabi oscillations for various phonon number populations, the damping rate is expected to scale according to the power law [19, 48, 66]

$$\gamma_n = \gamma_0(n+1)^x, \tag{3.5}$$

with γ_0 governing the ground state decay and x the damping factor. The decay enhancement characterized with the factor x depends partially on the spectral properties of noise, which can stem from both laser frequency or intensity fluctuations, or from the noise in the magnetic field. In addition, motional frequency fluctuations or fluctuations of the ion or laser beam position can contribute [66, 100–102]. In the first order approximation, the laser intensity fluctuations are expected to play most significant role, which, theoretically, should correspond to x=0.7 [103].

We perform a measurement to experimentally determine the damping factor on the generated states approaching close to ideal Fock states (see 3.16). Populations of the prepared states are close to 100 %, we may therefore assume

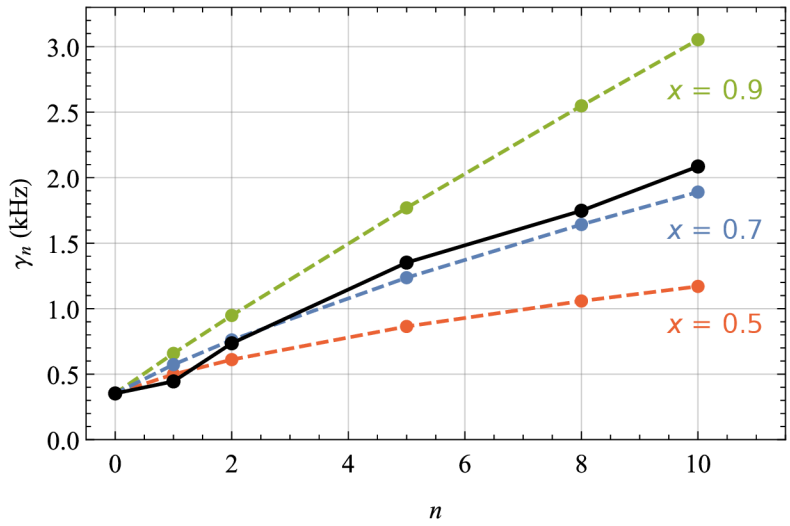

Figure 3.23: Estimation of the accuracy of γ_n scaling according to the Eq. 3.5 for various values of scaling factor x. Black line shows directly fitted values of γ_n from the Eq. 2.40. Green, blue and red lines show the values where $\gamma_0 = 0.35$ kHz and other values are calculated from the Eq. 3.5 for various factors x.

that damping will closely match the behavior described with Eq. 3.5. We obtain the corresponding γ_n factors from measured Rabi oscillations without any prior assumption on value of scaling parameter x. Finally, we take the initial value γ_0 as a reference, and evaluate γ_n with use of various scaling factors. The results are shown in Fig. 3.23. The initial damping factor corresponding to ground state was here estimated as $\gamma_0 = (0.35 \pm 0.02)$ kHz, where the uncertainty is estimated from five independent measurements.

Fig. 3.23 shows the measured and theoretically predicted damping factors γ_n, which are bound to the order of generated Fock state. The black line shows the measured values of γ_n which are evaluated from the Eq. 3.5 without any prior assumption on the scaling with factor x. In the other traces, we calculated the particular value of γ_n from the Eq. 3.5 where γ_0 is taken measured as the ground state damping and n depicts the number state order. We found out that the measured trend of the dependence reliably matches with the prediction for $x = 0.7$, which is in agreement with former observations and predictions [66].

3.14.4 Estimation of error in probability distributions

One of the crucial intrinsic effects in the estimation of the phonon number probability originates from the projection on one of two electronic levels.

This can be efficiently minimized by increasing the number of experimental repetitions, but it may never be suppressed completely. The uncertainty of projection then propagates through the whole fitting routine and additional data processing, up to the final probabilities and also to evaluated measures. For the short measurements, where long term temperature drifts contribute negligibly, the majority of the experimental uncertainty can be mapped back to the projection noise. With use of Monte-Carlo method, it is thus possible to determine these unknown uncertainties from the measured projection noise.

A projection noise is mathematically described with a binomial distribution, where N projections of the same experiment may result in two different outcomes. We typically probe the corresponding two-level system with $N = 100$ repetitions of each experiment. The error of each projection of a two-level system to it's eigenstate is calculated as

$$\delta P_e = \sqrt{\frac{P_e(1 - P_e)}{N}}, \tag{3.6}$$

where P_e denotes a probability of two-level projection.

The Monte-Carlo routine is then employed as following. After the Rabi oscillation measurement, we simulate additional 100 pseudo-random realizations of corresponding probed Rabi oscillation, where each measurement sample is randomly chosen with the Gaussian probability distribution, where the standard deviation of such a distribution is set to be equal to the error from the projection noise. For each of these virtual datasets, we estimate the population distribution, and from these, we can evaluate the standard deviation of each probability from the simulations, while the mean value is always taken from the measurement.

Typically, the obtained standard average error of estimated motional populations is usually ± 0.02 of the estimated population. We note that, this value does not represent the actual full measurement uncertainty, but it is the lower limit on the uncertainty given by the fundamental projection measurement. We thus employ this routine for measurements, where we did not acquire the multiple data sets for a given experimental setting, otherwise the error is always estimated statistically from several independent measurements.

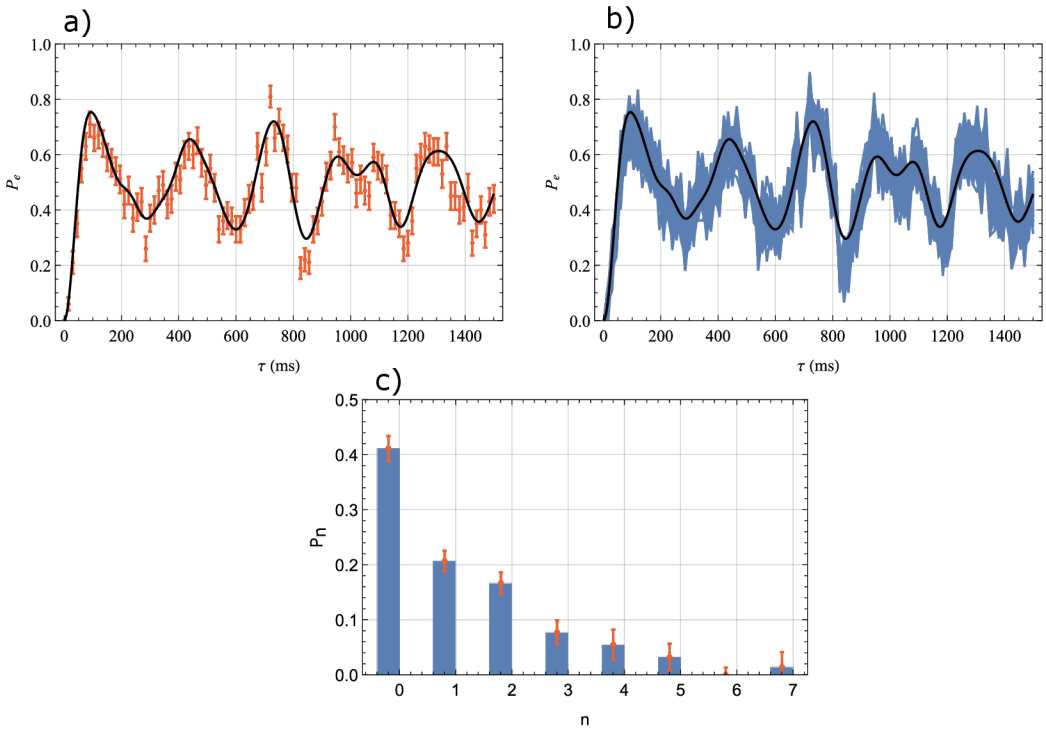

Figure 3.24: Illustration of Monte-Carlo routine for error estimation. In the first step, shown in a), we calculate the projection noise from 100 projection measurements of each point in the Rabi oscillation. The error bars depict the corresponding single standard deviation. Second, we generate the 100 random realizations of Rabi oscillations, where each point is varied with Gaussian probability distribution, whose standard deviation is set to be equal to measured projection noise. The scale of the generated values is depicted by blue in b). Finally, each of these virtual realizations is fitted and the corresponding phonon number distribution contributes to the final statistics. In c), we plot the resulting population distribution including population uncertainties, which are evaluated as standard deviations of the simulated distributions of P_n.

4. Mechanical Fock states of single trapped ion

This chapter covers results published in [35], related to the generation and characterization of number states. The discussion focuses mainly on experimental implementation, theoretical background to the work presented in this chapter can be found in references [21, 23, 104].

The process of number state generation from ground state of motion by repetitive addressing of the ladder-scheme, described in Sec. 3.10.2, represents a conceptually simplest method. However, the experimental feasibility of this method requires in principle very high degree of control of the mechanical quantum system. It requires a deep Lamb-Dicke regime of laser-ion interaction and a good ground state cooling for minimization of initial state entropy. The sequence time necessary to prepare higher number states is longer, which results to bigger affection of these states by the spontaneous heating processes in a room-temperature environments [111].

It is experimentally very demanding to create a desired motional number state which would have nearly ideal population probability of the particular energy level. However, even the state with small amount of imperfections can be employed in certain applications of interest. In this chapter we will attempt to answer the crucial question - what is the amount of thermal noise, which can be added to the system, so that the non-classical and quantum non-Gaussian (QNG) properties are preserved, necessary for the enhanced sensing applications [24] or quantum error correction codes [112].

It appears that the criteria of quantum non-Gaussianity provide a convenient tool to characterize the number states which undergo the noisy processes (see Sec. 2.11). Each criteria in the genuine quantum non-Guassian (GQNG) hierarchy [23] establishes a threshold value in number state basis, also specifying the amount of noise which is sufficient for destroying the visibility of the QNG properties. We also evaluate the quantum enhanced force estimation capability for the realized QNG states of single ion's mechanics.

4.1 Realization of the motional states approaching Fock states

The motional quantum states are generated by consecutive optimized applications of the axial-mode blue and red sideband on the transition $4S_{1/2} \rightarrow 3D_{5/2}$. The resulting statistical distributions of phonon populations are detected by probing the Rabi oscillation on this spectral line, whose frequency is spectroscopically measured at the detuning $\nu = 1.188$ MHz from the carrier transition. The population of the initial ground state $|g,0\rangle$ was measured as 98 %, corresponding to estimated mean energy $\overline{n} = 0.02 \pm 0.02$. The lengths of the π pulses for red and blue sideband interactions in ladder scheme are tuned experimentally, in order to achieve the maximal possible pulse contrast. The carrier Rabi frequency $\Omega_0 = 2\pi \times (69.7 \pm 0.1)$ kHz was measured from Rabi oscillations at $|g,0\rangle \rightarrow |e,1\rangle$ transition. Additional parameters used for the state reconstruction are Lamb-Dicke parameter $\eta = 0.0611 \pm 0.0002$ and the ground state damping factor $\gamma_0 = 2\pi \times (8.9 \pm 0.2)$ kHz from the Eq. 3.5 found by fit of the measured Rabi flops on the motional ground state with $P_0 = 0.98$.

The population distributions are shown in Fig. 4.2. The measured data are compared with the theoretical prediction, which takes into account the finite heating rate influencing the state during the time of the sequence, measured as $\overline{n} = 2.7 \pm 0.2$ phonons/s. In simulation, we further do not consider any dephasing and the efficiency of the population transfer by the employed π pulses, so the efficiency of the operation is for simulation set to 1. From 4.2, we see that the measured data agree with prediction, which takes into account merely the presence of the heating rate.

The non-Gaussian properties of the noisy states are evaluated with the criteria forming a hierarchy [23], where the specified criteria for the given number state $|n\rangle$ allow to exclude any state which would correspond to an arbitrary superposition of displaced and squeezed number states $|m\rangle$ for any $m<n$. The threshold probability for current number state under probe is calculated as [35]

$$\overline{p}_n = \max_{\alpha,r,c_0,\ldots,c_m} |\langle n|D(\alpha)S(r)\sum_{m=0}^{n-1} c_m|m\rangle|^2, \tag{4.1}$$

Details of theoretical derivation tailored originally for the photonic implementation, where the loss becomes the main state deteriorating mechanism, can be found in [23]. However, for mechanical systems, such as the employed trapped ion oscillator, thermalization due to the unavoidable direct coupling to the thermal environment has been found much more dominant.

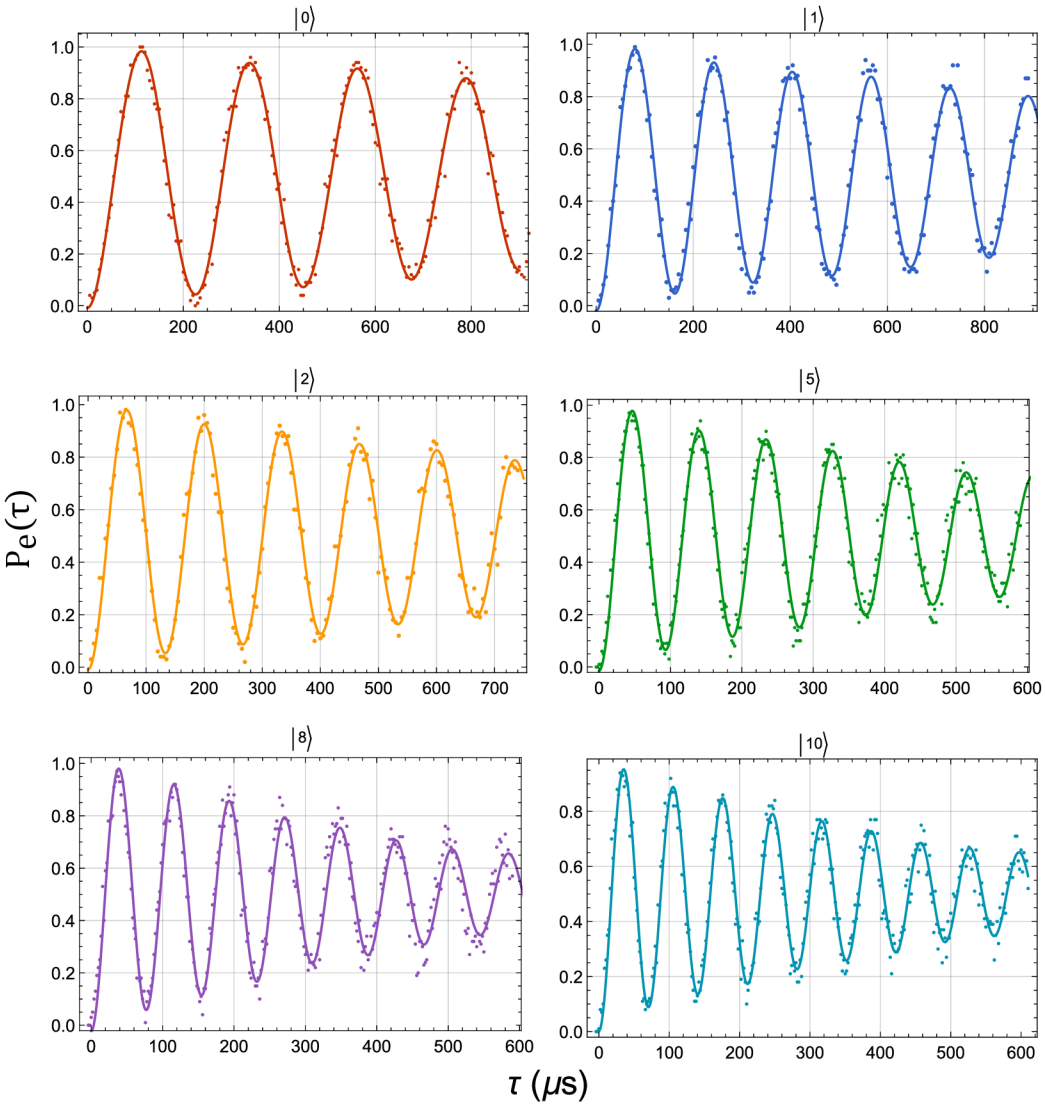

Figure 4.1: Measured Rabi oscillations on a blue motional sideband ofr motional Fock states up to the order $|10\rangle$. The increasing motional population is manifested by higher oscillation frequency, scaling up as $\Omega_{n,n+1} = \Omega_0 \eta \sqrt{n+1}$.

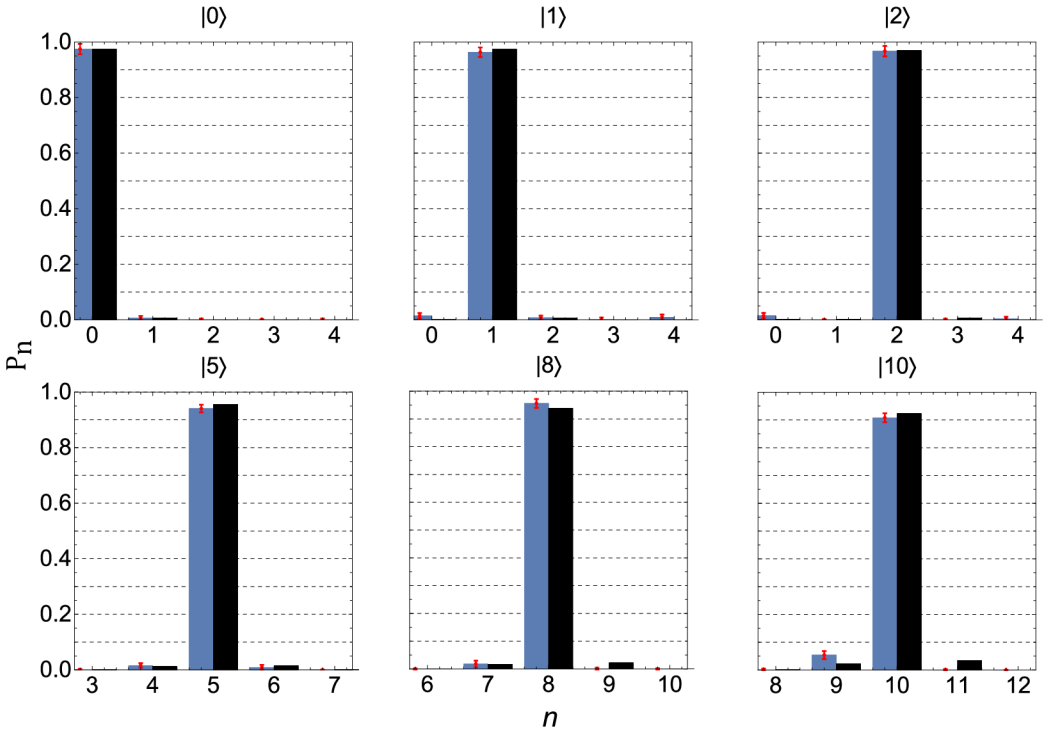

Figure 4.2: Measured and simulated populations of the Fock states. The resulting measured number state probabilities are $P_0 = 0.97, P_1 = 0.97, P_2 = 0.97, P_5 = 0.95, P_8 = 0.95, P_{10} = 0.91$, where for each of these values, the error estimate was obtained with use of the Monte-Carlo routine as ± 0.02 (see Sec. 3.14.4). The corresponding measured Rabi oscillations are shown in Fig. 4.1. A theoretical simulation, represented with black bars, assumes solely the state's imperfection caused heating effect during preparation pulse sequence, measured as $\Delta\overline{n} = 2.7 \pm 0.2$ phonons/s.

4.2 Heating dynamics on ground state of motion

The main source of gradual diffusion of Fock state population towards the neighboring oscillator states comes from the natural heating processes in the trap. The heating rate in our trap has been measured as approximately 2.7 phonons/s as presented in Sec. 3.12. This heating rate is sufficiently small to allow the realization of motional experiments on long scales of tens of ms, but this long time scale also makes it inconvenient for controllable characterization of robustness and thermalization depth of generated phononic QNG states.

The heating mechanism can be controllably implemented by photon

scattering. In our implementation, this is performed simply by adding a very short pulse at 397 nm transition before the state readout step. In the limit of long laser excitation-thermalization times, the population converges towards thermal distribution with energy corresponding to Doppler cooling limit. The interaction with the laser can be viewed as engineering of the thermal reservoir at the temperature parameterized by the interaction setting. Depending on the 397 nm laser detuning, it can correspond to temperature scale from about the Doppler cooling limit corresponding to cooling on the $4S_{1/2} \rightarrow 4P_{1/2}$ transition, or much higher temperature reservoirs for interaction with a resonant or blue-detuned laser.

We characterize this heating by implementing the calibration measurement on initial ground state of motion, in order to determine amount of energy added to the system as a function of length of the thermalization pulse. Formally, we can define the heating process as a map M_n affecting the motional distribution ρ_i in a way

$$M_{\overline{n}}(\rho_i) = \int d^2\alpha e^{-\frac{|\alpha^2|}{\overline{n}}} D(\alpha)\, \rho_i D^\dagger(\alpha). \tag{4.2}$$

For small energies $\overline{n}$, the Eq. 4.2 can be further simplified as

$$M_{\bar{n}}(\rho_i) \approx \rho_i + \bar{n}^2[a\rho a^\dagger + a^\dagger \rho a - (a^\dagger a + 1/2)\rho_i - \rho_i(a^\dagger a + 1/2), \tag{4.3}$$

where terms proportional to $\bar{n}^4$ are neglected. The map $M_{\bar{n}}$ in this approximation generally represents a change of the motional state caused by scattering with the recoil probability parametrized by $\overline{n}$.

A thermalization process described with equations 4.2 and 4.3 is valid only in the limit of low initial energies. For a state close to the Doppler cooling limit, one has to take into account the different heating dynamics with a steady state corresponding to the finite temperature of the ion on the level of few mK. The dynamics to reach this energy limit will be however dependent on the initial thermal state.

Fig 4.3 shows the initial ground state with measured $\overline{n} = 0.02 \pm 0.02$ phonons, undergoing thermalization with different lengths of the 397 pulse, where the longest time is equal to 12.8 μs. Each measured Rabi oscillation data are fitted to estimate the P_n (blue bars), and the corresponding estimated mean phonon number is used for evaluation of the idealized Bose-Einstein distribution expectable for the thermal motional state. The blue columns in Fig. 4.3 represent the measured data, and the black bars correspond to theoretical statistical distribution. The error estimates are evaluated by Monte-Carlo simulation method (described in Sec. 3.14.4). Direct quantitative comparison of measured

population distributions with ideal thermal statistics corresponding to the same mean energies clearly confirms the expectation that the consecutive application of laser induced random photon recoils results in thermalization of the single ion mechanical oscillator.

We construct a function describing the amount of thermal energy added to the system by a 397 nm pulse of the rate of laser induced thermalization. Fig. 4.4 depicts in red points the observed thermal energy as a function of heating pulse duration τ. The black dashed line shows the linear trend fitted to the data. For experiments presented further, we use the trend function to estimate the amount of energy added to the system, rather than taking the measured values directly. The linear approximation is expected to hold in case that the added energy is much lower than Doppler cooling limit. For higher values, we would expect the trend to continuously saturate towards this limiting value. The available data presented in Fig. 4.4 justify the use of linearized approach for the range of heating used in our experiments. The measured heating rate, when assuming the linear unsaturated part, was estimated to be $\Delta\overline{n} = (115 \pm 2) \times 10^3$ phonons/s.

4.3 Heating dynamics for number states

In this section, we describe the measurement of heating dynamics for number states $|1\rangle, |2\rangle$, with use of the heating process as described in previous Sec. 4.2. Analogic experiments were also performed on number states $|5\rangle, |8\rangle, |10\rangle$.

For the short time scales of the experimental sequence, relevant for the generation of target Fock states, the heating results in the error given predominantly by values of (P_n, P_{n-1}, P_{n+1}). The QNG robustness may be thus conveniently characterized by a simple comparison of the amount of population P_n with respect to the populations contained in neighboring states P_{n-1}, P_{n+1}, with the QNG threshold probability defined as $(P_n, P_{n-1} + P_{n+1})$. In case that the population of state undergoing heating exceeds these values, it can be shown that the state may be described as Gaussian [23]. The depth of non-Gaussianity can be then understood as an amount of thermal noise, which can be added to the system and at the same time, the state population is higher threshold.

Figures 4.5 and 4.6 show the measured heating dynamics of the Fock states $|1\rangle$ and $|2\rangle$, respectively, illustrating the gradual thermal diffusion of the number state population towards the neighboring oscillator levels. For the measurement, we set the intensity of the Doppler heating pulse as in the calibration measurement, and we take the calculated heating into the simulation of the evolution probability. Both measured states show the slight asymmetry of diffusion favoring the higher motional states for short thermalization times. This is caused by the asymmetry in relative amplitudes for annihilation and creation

operations in Eq. 4.3. In Fig. 4.5, we observe the development of the Fock state $|1\rangle$ to nearly ideal thermal population distribution ($\overline{n} = 2.6$), however, it is still far from reaching the limiting Doppler temperature. For the limiting case of infinite heating time, we except the convergence to the ideal thermal state with a temperature corresponding to the Doppler cooling limit.

The same measurement results are also plotted in Fig. 4.7 in coordinates defined with $(P_n, P_{n-1} + P_{n+1})$. Here, the point located in the upper left corner denotes the initial state, and the heating proceeds towards the bottom right corner. The green ticks and red crosses denote the area, where the corresponding quantum states fulfill the GQNG condition, or reject it, respectively. While probing the state $|1\rangle$, the GQNG threshold is exceeded up to the thermalization pulse of the length $\tau = 2.1\ \mu$s, which adds the energy equal to $\overline{n} = 0.31$ phonons. For the state $|2\rangle$, the thermal depth of QNG is substantially lower, reaching $\overline{n} = 0.13$ phonons. The corresponding thermal energies defining the depth of non-Gaussianity are obtained from a calibration measurement, depicted in Fig. 4.3.

The Fig. 4.8 analyses the exhibition of the genuine n-phonon QNG using idealized and measured Fock states (red data points on the top of the plot range) that are deteriorated by the thermalization process. The presented simulations signify that the observability of the lowest QNG features (red points) characterized by rejecting any mixture of $|\psi_n\rangle = D(\alpha)S(r)|0\rangle$ [21] in the presence of mechanical heating monotonously decreases with n for ideal Fock states. On the contrary, the generation and observation of genuine QNG properties (blue points) for high Fock states inside the hierarchy in Eq. 4.1 is challenging and its sensitivity to imperfections in the state preparation and detection increases with n.

The considered ideal thermalization dynamics corresponding to a Gaussian additive noise can be broadly employed for an estimation of the QNG depth, analogically, as the damping was used for photonic states [113]. The thermal depth of presented QNG witnesses has been evaluated as the corresponding increase of the mean thermal energy $\bar{n}_{\mathrm{th}}$ for the same thermalization strength applied to the vacuum state. This comparison allows for an experimental platform-independent comparison of depth of the genuine QNG states in mechanical systems. In turn, these measurements can be also employed for testing the quality of the mechanical system or for sensing of the amount of the inherent thermal noise. The thermal depth of the measured states is much

smaller for the genuine QNG hierarchy (Eq. 4.1), in a contrast to the lowest QNG criteria [21] that actually are less demanding for the higher Fock states. Still, the measured 10-phonon states conclusively proved the genuine QNG features. Although the absolute thermal depths shown as mean phonon numbers $\bar{n}_{\mathrm{th}}$ of the thermalization process decrease both for the genuine QNG features (blue values) and for the lowest QNG criteria [21](red values), their ratio increases to about an order of magnitude for $n = 10$.

4.4 Quantum enhanced sensing of mechanical force

We estimate the possible metrological advantage for phase independent amplitude sensing of the generated higher order number states. This is done with use of the classical Fisher information and Cramér-Rao bound. The following discussion is directly extracted from our work published in [35].

A mechanical oscillator prepared in a state approaching a Fock state can be directly used for a phase-insensitive sensing of a mean phonon number of weak force causing tiny displacement α of the mechanical oscillator [24] with applications in precise measurements of a small radio-frequency noise or quantum logic spectroscopy [114]. Let the mechanical oscillator be prepared in an initial state ρ and let $D(\alpha)$ denote the displacement operator characterizing evolution that the force induces. The Fisher information for the estimation of the parameter $|\alpha|^2$ reads

$$F = \sum_{m=0}^{\infty} \frac{1}{P_m(|\alpha|^2)} \left[\frac{\mathrm{d}}{\mathrm{d}_{|\alpha|^2}} P_m(|\alpha|^2) \right]^2, \tag{4.4}$$

where $P_n(|\alpha|^2) = \langle n|D(|\alpha|)\rho D^{\dagger}(|\alpha|)|n\rangle$ is the phonon-number distribution on which the sensing is performed. The Cramér-Rao bound limits the standard deviation σ of the force estimation according to $\sigma^2 \geq 1/(NF)$ with N being a number of sensing runs. We evaluate the σ saturating the Cramér-Rao bound for realistic states that perform the sensing. The estimation of metrological advantage R_ρ can be quantified for the state ρ according to

$$R_\rho(|\alpha|^2) = \frac{\sigma}{\sigma_0}, \tag{4.5}$$

where σ_0 stands for the standard deviation of the displacement measurement for the mechanical oscillator probe prepared in the motional ground state. For ideal

Fock states, (4.5) approaches

$$R_{|n\rangle}(|\alpha|^2) = \frac{1}{\sqrt{2n+1}}, \tag{4.6}$$

which is independent of the estimated parameter $|\alpha|^2$. For more details on this derivation see the Supplementary information of [35].

If a state ρ achieves $R_\rho(|\alpha|^2) < R_{|n\rangle}$ for some $|\alpha|^2$, it possesses a capability to surpass limitation in the sensing given by the Fock state $|n\rangle$. Therefore, the sequence $R_{|n\rangle}$ establishes a hierarchy of conditions for the sensing classifying the states approaching Fock states. Fig. 4.9 presents the metrological potential of the prepared motional Fock states to pass some of these conditions. Specifically, the realistic Fock states up to $n = 10$ surpass limits given by the vacuum state and the prepared state approaching the ideal Fock state $|8\rangle$ presents the capacity to exceed the Fock state $|5\rangle$. The realized state approaching $|10\rangle$ and all the higher prepared Fock states do not possess the metrological advantage against the ideal Fock state $|8\rangle$ mainly due to noise contributions including dominantly the residual heating during the state preparation sequence.

For sensing of small $|\alpha|^2$, the noise affects how far is a prepared state approaching $|n\rangle$ from the threshold given by the ideal Fock states $|n\rangle$. The advantage gets lost when realistic states contain even very small deteriorating noise which substantially decreases the speed of the sensing in the high $|n\rangle$ limit. The metrological gain $R_\rho(|\alpha|^2)$ tends to saturate for displacement amplitudes on the order of 10^{-2} and approaches the gain expectable for the ideal Fock states. At the same time, the employment of realistic states with high n in the limit of small displacements seems to be further enhanced by effectively decreasing dependence of the offset amplitude in $R_\rho(|\alpha|^2)$ on n, when compared to ideal Fock states. This has been confirmed by a numerical simulation considering sensing with states resulting from idealized thermalization of Fock states and is in agreement with the approximate formula $R_\rho(|\alpha|^2)$ for $|\alpha|^2 \ll 1$ that follows from the approximate expression for σ in (4.5).

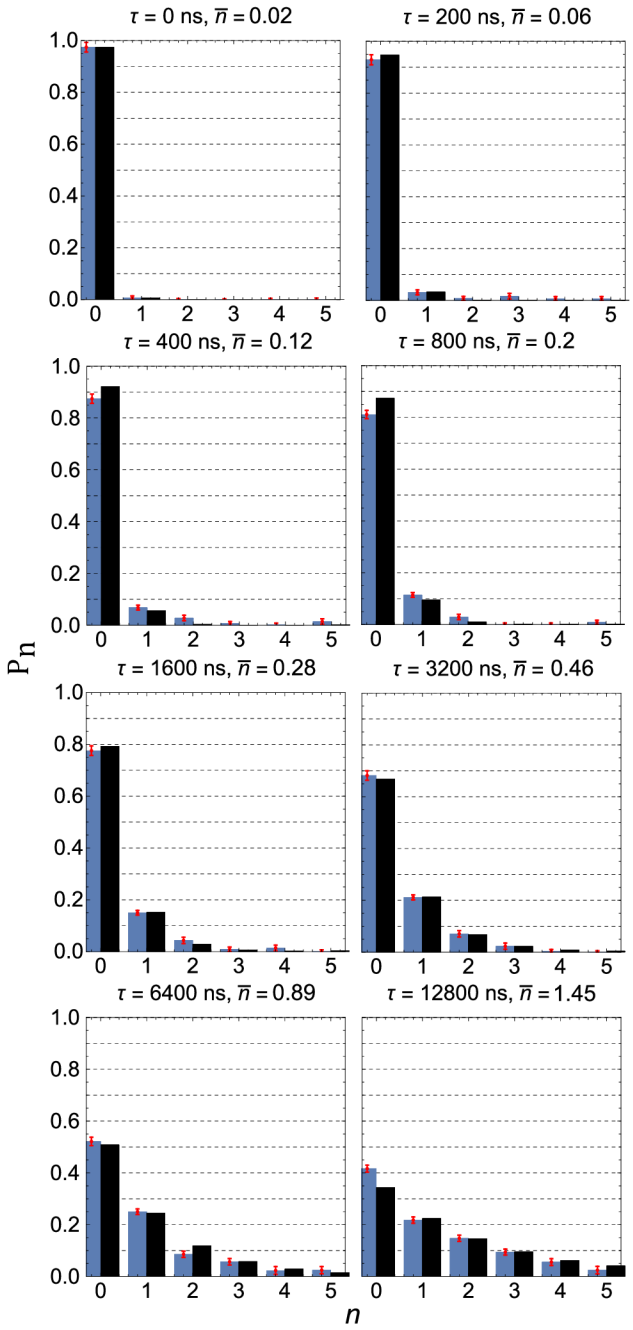

Figure 4.3: Calibration of the rate of laser induced thermalization on measurement for initial ground state on axial mode. Blue bars correspond to measured data, black bars show the thermal distribution corresponding to the added mean energy $\overline{n}$. From the comparison of measured and theoretical statistic, it is apparent the the heating dynamics described with Eq. 4.3 clearly leads to generation of the thermal states.

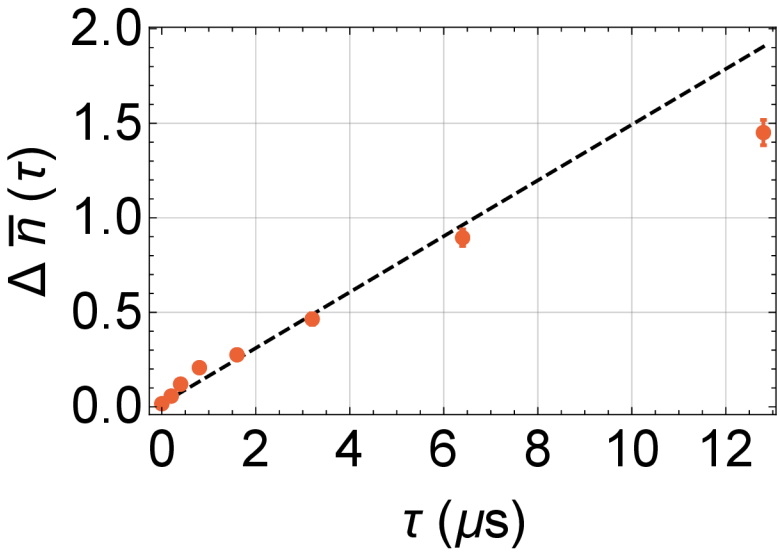

Figure 4.4: Calibration of thermalization measurement, the amount of thermal energy $\Delta\overline{n}$ added to the ground state as a function of a length of the Doppler heating pulse at 397 nm transition. Red points correspond to the measured values (see also previous Fig. 4.3), and the black dashed line relates to the fitted linear dependence. For the last value of $\Delta\overline{n}$ at $\tau = 12.8$ ms, the mean energy already approaches the Doppler limit, which explains the discrepancy with the linear fit applied to rest of the measured points. In order to achieve the better fitting accuracy, it would be necessary to perform a better model also considering the saturation which was measured as $\overline{n} = 8.0 \pm 1.0$. For short time scales at which the experiments are performed, it appears to be more convenient to describe the heating as a linear dependence on time. The resulting linear heating rate was estimated as $\Delta\overline{n} = (115 \pm 2) \times 10^3$ phonons/s.

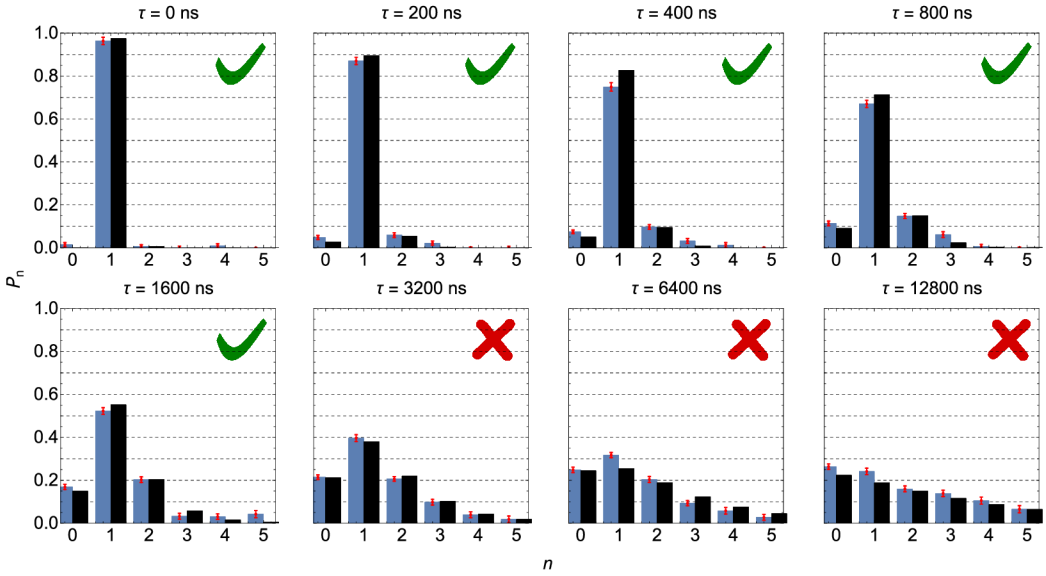

Figure 4.5: Heating dynamics and GQNG depth measured for Fock state $|1\rangle$. States which are marked with a green tick agree with the definition of the GQNG states (Eq. 2.45). States denoted with the red cross do not exceed the GQNG threshold. The limiting maximal amount of thermal energy which can be added to the system, and at the same time it preserves the QNG property, is estimated as $\Delta\overline{n} = 0.31$ phonons, corresponding to 2.1 μs heating pulse.

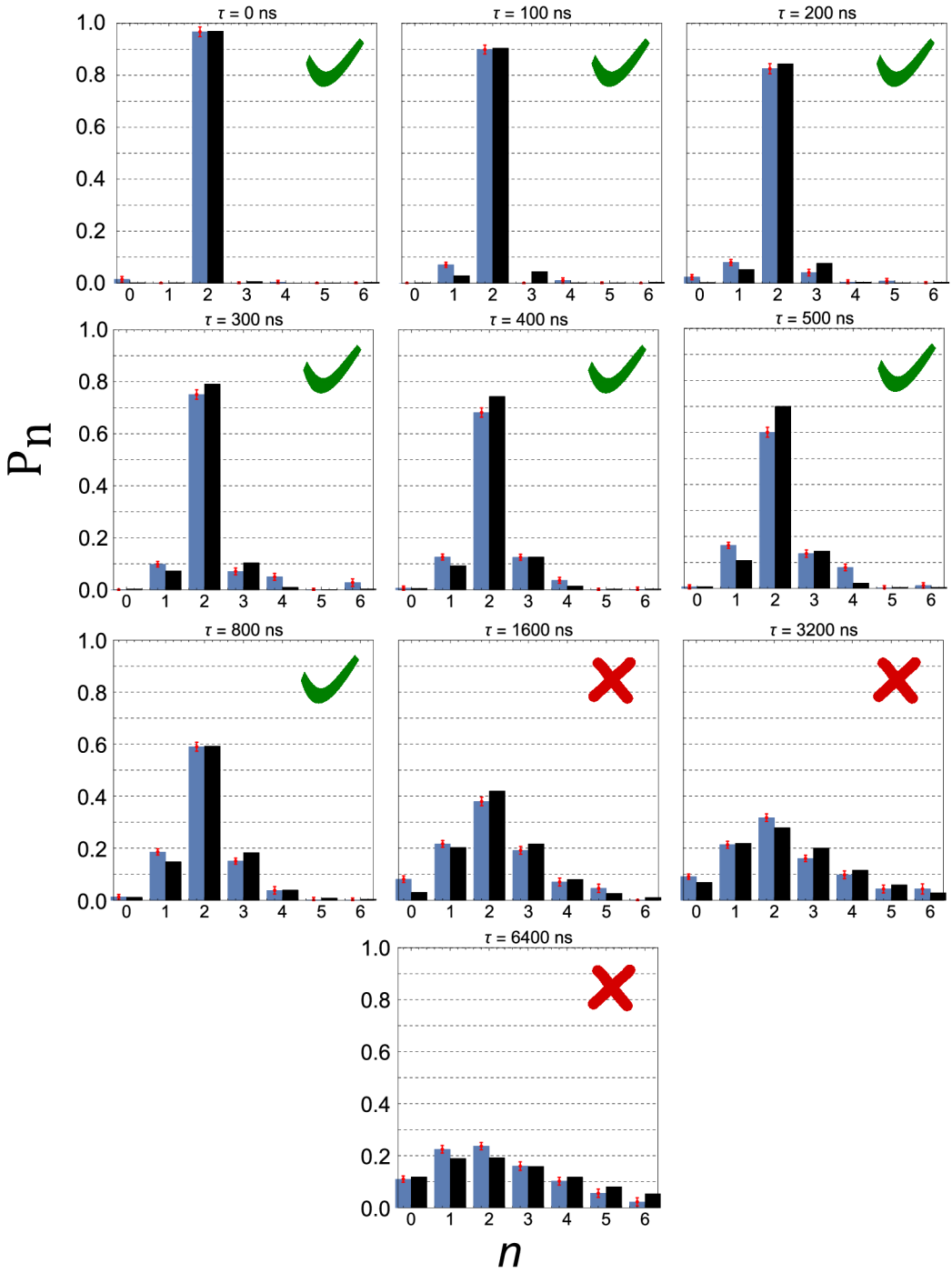

Figure 4.6: Measured thermalization dynamics and GQNG depth for Fock state $|2\rangle$. Similarly to the measurement in Fig. 4.5, the states marked with green tick are probably genuine QNG, while the states with red cross do not surpass the the GQNG threshold. The GQNG depth parametrized by the amount of added thermal energy is estimated as $\Delta\overline{n} = 0.13$, which is smaller when compared to $\Delta\overline{n} = 0.31$ for a number state $|1\rangle$.

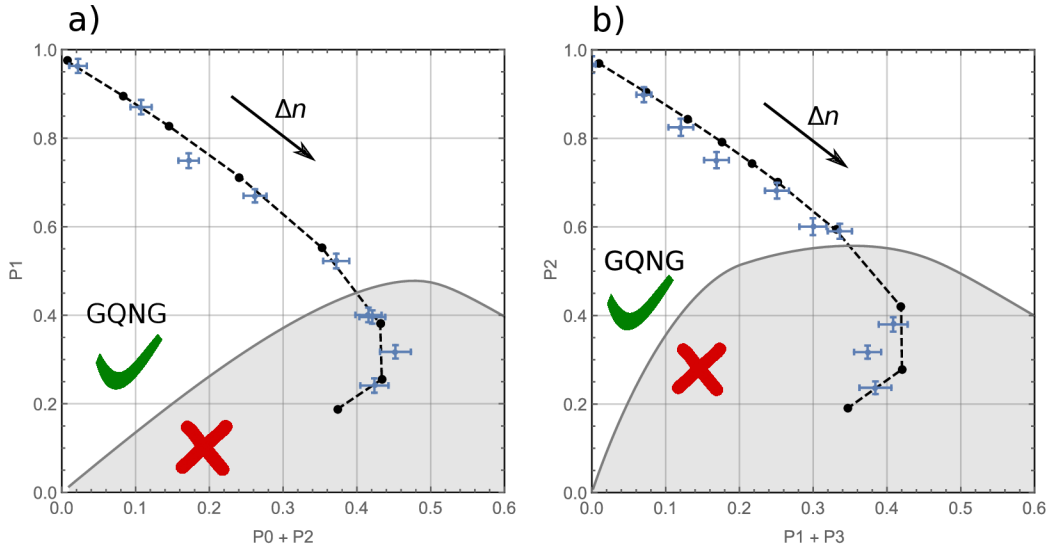

Figure 4.7: Thermalization dynamics for generated Fock states $|1\rangle$ in a), and $|2\rangle$ in b). Blue points correspond to measured states, and black line predicts a theoretical development, which corresponds to the state's distribution undergoing the addition of thermal energy according to the calibration measurement on the motional ground state (see Fig. 4.3). The dynamics progresses from the left upper corner, proceeding to the bottom right. The GQNG thermal depth for the number state $|1\rangle$ is evaluated as $\overline{n}_{\mathrm{th}} = 0.31$ phonons, while for the state $|2\rangle$ this value is substantially lower, equal to $\overline{n}_{\mathrm{th}} = 0.13$ phonons.

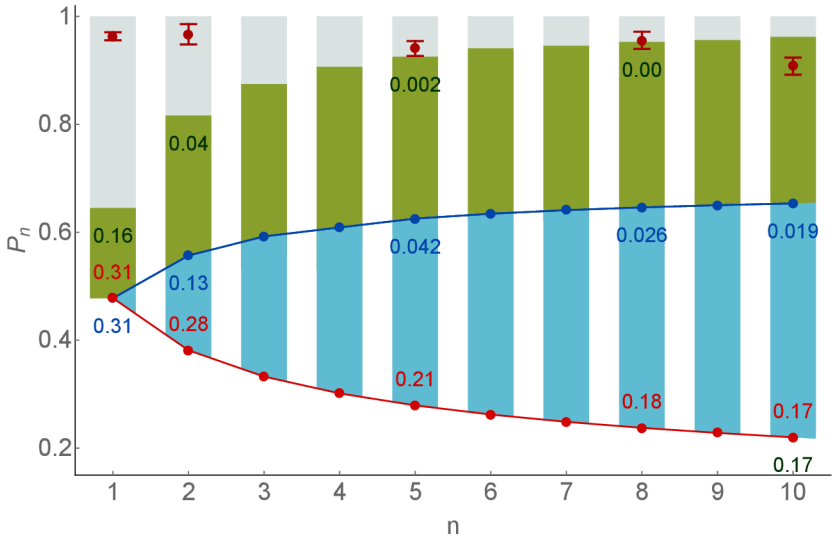

Figure 4.8: Characterization of the Fock states of mechanical motion. The red points in the upper part of the plot represent the measured populations P_n for experimentally generated states. The thresholds for a genuine n-phonon QNG are represented by blue points. The associated blue numbers quantify the thermal depth of genuine n-phonon QNG - a maximal mean number of thermal phonons $\bar{n}_{\mathrm{th}}$ that keeps the measured states above the genuine n-phonon QNG thresholds. Similarly, the red points identify thresholds for observation of the basic QNG aspects [21] and the associated red numbers determine their thermal depth. The green bars depict the force estimation capability of a specific model of noisy Fock states, where the probability P_n exceeding the presented threshold values certifies a metrological advantage [24] against the previous ideal Fock state $|n-1\rangle$ in the force estimation, while the corresponding numbers quantify a thermal depth of this advantage for the measured states.

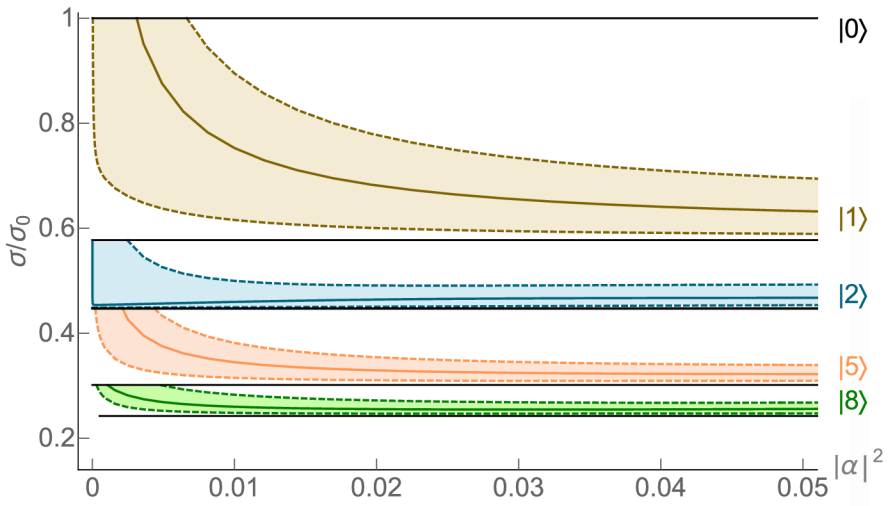

Figure 4.9: The estimation of the metrological advantage of experimentally realized states compared to the ground state for sensing of a small force that exerts motion on a mechanical oscillator. The horizontal axis quantifies the amplitude in the phase space that the force causes. The vertical axis shows the minimal standard deviation σ estimated by optimization of the Fisher information in the Eq. 4.4. The σ is normalized to the uncertainty σ_0 resulting from the equivalent sensing using a motional ground state. The black solid lines show σ/σ_0 for ideal Fock states. The dark yellow, blue, orange, and green solid lines correspond to the experimentally prepared states approaching the Fock states $|n\rangle = |1\rangle, |2\rangle, |5\rangle$, and $|8\rangle$, respectively. The graph displays only the cases of measured QNG states approaching Fock states $|n\rangle$ which surpass σ/σ_0 achievable with ideal Fock states $|m\rangle$ corresponding to any measured $m < n$. The colored regions within the borders given by dashed lines correspond to achievable σ/σ_0 for states with the phonon-number distributions within the experimental error bars.

5. Deterministic accumulation of mechanical non-classicality

This Chapter covers the experimental work published in reference [34] devoted to generation of non-classical motional states from distributions with high initial thermal energies. We report the acquisition of non-classical features in the generated state by repetitive application of anti-Jaynes Cummings interaction. This process is unconditional as it occurs deterministically for any initial thermal motional distributions without any postselection on the qubit state. The non-classical nature of outgoing statistical mixtures originates from a deterministic incoherent modulation of thermal phonon number distribution. The output state converges towards a state which has a significant overlap with a particular Fock state population. During such a process, the non-classicality can be deterministically increased, and manifests a strong quantum non-Gaussian properties.

The chapter begins with the expansion of the theory of anti-Jaynes-Cummings interaction, applied on an arbitrarily modulated state with a diagonal matrix representation. We present and discuss the employed experimental methods and we compare the resulting motional population distributions with theoretically predicted values, and evaluate the additional criteria of non-classicality.

5.1 Modulation of populations by non-linear interactions

In the following considerations about the non-linear interactions between a two-level and harmonic oscillator systems, we follow the approach described in [115] and [116]. Thermal state undergoing the addition or subtraction of energy by anti-Jaynes-Cummings (AJC), or Jaynes-Cummings (JC) interaction respectively, can create a statistical mixture of number state populations which

are non-classical. The non-classicality depends on the parameters of input thermal state and of the interaction.

We consider the harmonic oscillator to be in thermal motional state with the Bose-Einstein population distribution, and the two-level system being either in ground, or excited state. The interaction consists of the free evolution and interaction parts. We can write Jaynes-Cummings interaction as

$$H_{JC} = \hbar g(\sigma_+ a + a^\dagger \sigma_-), \tag{5.1}$$

and anti-Jaynes interaction as

$$H_{AJC} = \hbar g(\sigma_+ a^\dagger + a\sigma_-), \tag{5.2}$$

where the phase factors were set to 0 without any loss of generality of this description. These operations can be considered to implement the phonon absorption (for a operator) or emission (for $a^\dagger$).

For the case of J-C interaction, the evolution of the initial state can be described with an unitary operator $U_{JC} = \exp(-\frac{i\hbar H_{JC}}{\hbar})$, which can be also expressed in the qubit eigenbasis as [116]

$$U_{JC} = A_{gg}(t)\left|g\right\rangle\left\langle g\right| + A_{ee}(t)\left|e\right\rangle\left\langle e\right| + A_{eg}(t)\left|e\right\rangle\left\langle g\right| + A_{ge}(t)\left|g\right\rangle\left\langle e\right|, \tag{5.3}$$

with

$$\begin{aligned} A_{gg}(t) &= \cos(gt\sqrt{n}), & A_{eg}(t) &= a\frac{\sin(gt\sqrt{n})}{\sqrt{n}}, \\ A_{ee}(t) &= \cos(gt\sqrt{n+1}), & A_{eg}(t) &= -a^\dagger \frac{\sin(gt\sqrt{n+1})}{\sqrt{n+1}}. \end{aligned} \tag{5.4}$$

Here, n is the operator of number of quanta $n = a^\dagger a$. Next, we will focus on evolution of oscillator for the initial thermal state of the two-level system, which can be described with the following density matrix

$$\rho_e = p_e\left|e\right\rangle\left\langle e\right| + (1-p_e)\left|g\right\rangle\left\langle g\right|, \tag{5.5}$$

where p_e denotes the excited state probability. The dynamics of the state's evolution can be calculated by application of a completely positive map combining the qubit-oscillator state [116]

$$\begin{aligned} \rho_{\text{out}} = {} & p_e A_{eg}(t)\rho_{th}A_{eg}^\dagger(t) + (1-p_e)A_{gg}(t)\rho_{th}A_{gg}^\dagger(t) + \\ & + p_e A_{ee}(t)\rho_{th}A_{ee}^\dagger(t) + (1-p_e)A_{ge}(t)\rho_{th}A_{ge}^\dagger(t). \end{aligned} \tag{5.6}$$

By placing the formulas of the operators $A_{gg}, A_{ge}, A_{eg}, A_{ee}$ into the Eq. 5.6, we write the final formula modulation of the initial thermal distribution as

$$\rho(t) = \sum_{n=0}^{\infty} |n\rangle\langle n| \frac{\overline{n}^n}{(1+\overline{n})^{n+1}} \times \\ \times p_e \left[\cos^2(gt\sqrt{n+1}) + \frac{1+\overline{n}}{\overline{n}} \sin^2(gt\sqrt{n})\right] + \\ + (1-p_e)\left[\cos^2(gt\sqrt{n}) + \frac{\overline{n}}{1+\overline{n}} \sin^2(gt\sqrt{n+1})\right]. \quad (5.7)$$

The particular limit of the initial quibit state in a state with minimal thermal energy corresponding to the ground state further simplifies this equation, so that $p_e = 0$ and the second line in the formula 5.7 can be erased completely. The evolution of the density matrix undergoing the Jaynes-Cummings interaction can then be described in the final form as:

$$\rho_{\text{abs}}(t) = \sum_{n=0}^{\infty} |n\rangle\langle n| \frac{\overline{n}^n}{(1+\overline{n})^{n+1}} \left[\cos^2(gt\sqrt{n}) + \frac{\overline{n}}{1+\overline{n}} \sin^2(gt\sqrt{n+1})\right]. \quad (5.8)$$

In a similar way, we may describe the dynamics under the anti-Jaynes-Cummings interaction. This is driven with the elements in Eq. 5.7 which were previously neglected for the phonon absorption description. We can finally write [115]

$$\rho_{\text{em}}(t) = \sum_{n=0}^{\infty} |n\rangle\langle n| \frac{\overline{n}^n}{(1+\overline{n})^{n+1}} \left[\cos^2(gt\sqrt{n+1}) + \frac{1+\overline{n}}{\overline{n}} \sin^2(gt\sqrt{n})\right]. \quad (5.9)$$

The effect of state's probability modulation by single phonon emission is simulated and depicted in Fig. 5.1. By changing the pulse area gt of the applied anti Jaynes-Cummings interaction, we tune the effect of probability modulation on the final distribution. A special case occurs when $gt = \pi/2$, which corresponds to the addition of a full single quantum at the transition $|g,0\rangle \rightarrow |e,1\rangle$. For the ion with the maximum of the population in P_0, this operation generates number state $|1\rangle$. Another special effect occurs when $gt = \pi$. In such a case, the population in $|g,0\rangle$ undergoes the whole loop between the states $|g,0\rangle \rightarrow |e,1\rangle \rightarrow |g,0\rangle$, so the ground state population P_0 remains unchanged. The population in the higher energy levels is modulated, creating superpositions of in the two-level system between the ground and excited levels.

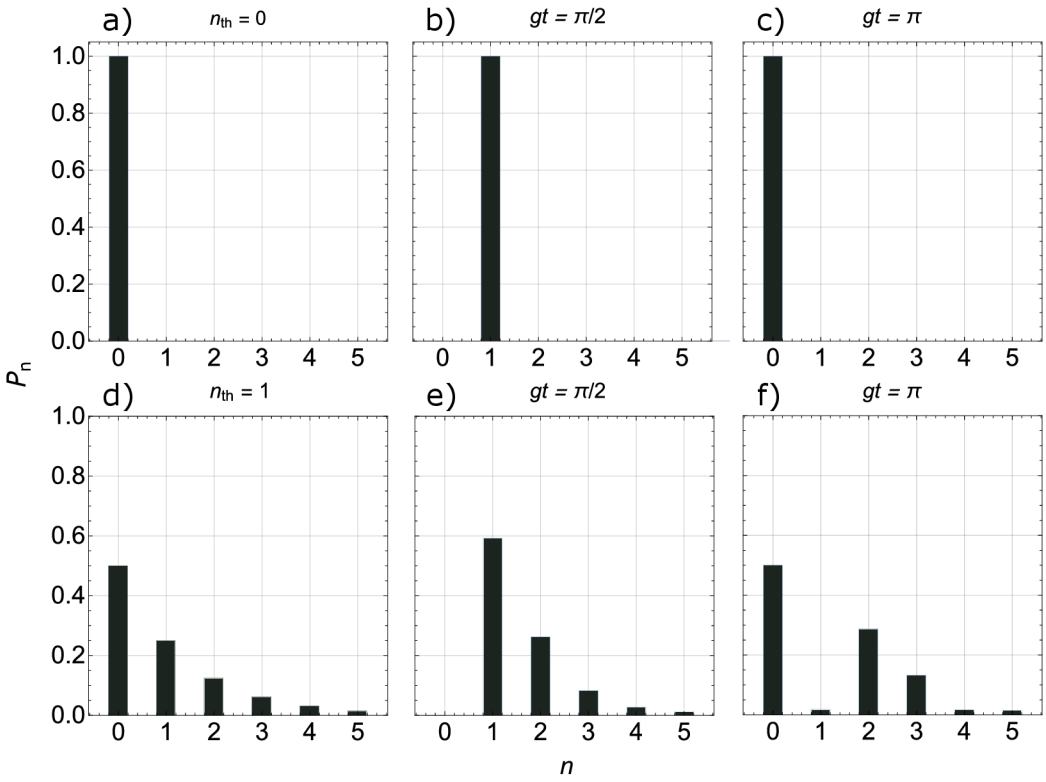

Figure 5.1: Simulation of thermal distributions undergoing the anti-Jaynes Cummings interaction, described with the Eq. 5.9. Figures a) and d) show the statistics of initial thermal states before the interaction, with energies corresponding to a mean phonon number $\bar{n_{\text{th}}} = 0$ and $\bar{n_{\text{th}}} = 1$. Cases depicted in b) and d) show the addition of a single quantum using a Rabi pulse with the area $gt = \pi/2$, which corresponds to the transition $|g, 0\rangle \rightarrow |e, 1\rangle$. b) shows a perfect generation of Fock state $|1\rangle$ from ground motional state. In d), the whole population of level $|0\rangle$ is shifted to $|1\rangle$, leaving the probability P_0 empty. A special cases depicted in c) and f) show the resulting populations after application of $gt = \pi$. For an initial thermal state close to $|0\rangle$, the population makes a whole cycle $|g, 0\rangle \rightarrow |e, 1\rangle \rightarrow |g, 0\rangle$, leaving the resulting state in the same state as in the beginning. In part f), the operation gives rise to the modulation of statistics, leading to the state which is strongly non-classical.

The origin of the modulation lies in the scaling of the Rabi frequency by factor $\sqrt{n+1}$ (see Sec. 2.6).

The Eq. 5.9 describes the addition of single quantum to the thermal initial distribution. In order to describe multiple repetitive interaction steps, we need to extend the formula to calculate probability modulation of an arbitrary input state. The Eq. 5.9 can be also written as [115]

$$\rho_b(t) = \sum_{n=0}^{n_{max}} P_n \left[\cos(gt\sqrt{n+1})\right]^2 |n\rangle\langle n| + \\ + \sum_{n=0}^{n_{max}} P_n \left[\sin(gt\sqrt{n+1})\right]^2 |n+1\rangle\langle n+1| . \quad (5.10)$$

In this formula, the elements of $\sum_n P_n$ may be arbitrarily distributed, unlike those in the Eq. 5.7, whose population distribution is thermal. The Eq. 5.10 can be conveniently used to describe the repetitive emission process. At the end of the interaction, the system is traced over the two electronic state and projected to the space of the harmonic oscillator.

5.2 Phonon addition in anti-Jaynes-Cummings interaction

The experiment starts by the addition of the single energy quantum at the 1^{st} axial motional sideband into thermal states with various energies. The outcome of this operation can be calculated from the Eq. 5.9 or Eq. 5.7.

The experimental conditions are similar to those in the experiment described in Chapter 4. The axial motional mode frequency has been set to $\nu_{\mathrm{ax}} = 1.188$ MHz. The carrier Rabi frequency was measured as $\Omega_c = 2\pi \times (92 \pm 1)$ kHz and the Lamb - Dicke parameter $\eta_{729} = (61.1 \pm 0.2) \times 10^{-3}$ (see Sec. 3.11). The optimized π pulse length was measured as $\tau = 91\ \mu s$.

The experimental sequence follows with sideband-cooling step, where a variable pulse duration is used to tune the initial thermal energy. In a motional manipulation step, we apply the single 729 nm pulse with length τ to the 1^{st} blue motional sideband, which adds the energy given by the pulse area gt. A short 854 nm reshuffling pulse is applied to transfer the residual D-state population back to the ground state of a two-level system. The state readout is performed with the electron shelving method, realizing hundred repetitions of the experimental sequence. The resulting population distribution is then obtained by a fit of the blue sideband Rabi oscillations using the Eq. 2.40.

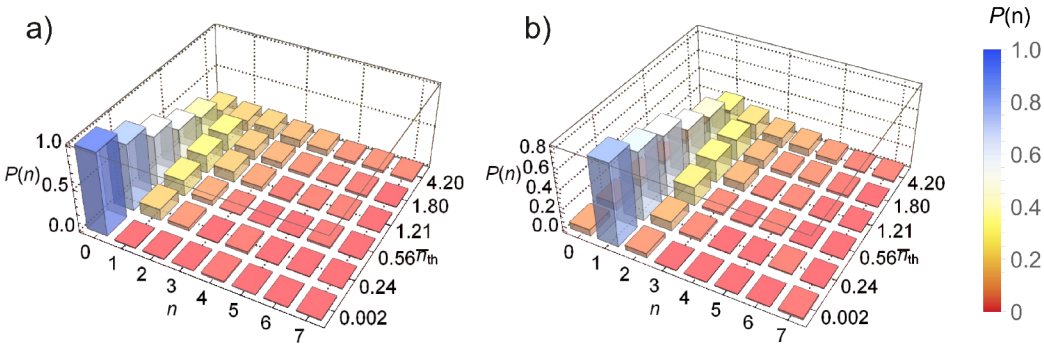

Figure 5.2: Measured distributions of initial thermal state, undergoing a an addition of a single quantum at AJC interaction with $gt = \pi/2$, which would ideally correspond to the transformation of the whole population from the state $|g,0\rangle \rightarrow |e,1\rangle$. a) shows the reconstructed initial thermal states, b) depicts distributions after the addition of a single motional quantum. The axis denoted with n_{th} defines the mean energy of initial thermal state, axis n points out the population of corresponding number state level.

In the first measurement we prove that, already for an initial state having a thermal Bose-Einstein population distribution, the incoherent modulation described with the Eq. 5.10 deterministically results into the non-classical states even for a broad range of initial thermal energies. The pulse area gt is in this case set as $gt = \Omega_0\eta\tau = \pi/2$, which is experimentally calibrated at 1^{st} blue sideband excitation of $|g,0\rangle \rightarrow |e,1\rangle$. While varying the initial thermal energy $\overline{n}$, we add a phonon depending on the chosen gt and input state statistics which leads to a transfer of a whole population from P_0 to P_1 for an ion prepared initially in the motional ground state.

The resulting statistics of initial thermal states and resulting distribution after the phonon addition are depicted in Fig. 5.2. The data measured after the interaction indeed show the obvious emergence of non-classical statistics with the benefit of P_1. The state with the lowest thermal energy corresponding to the ground state of motion was prepared such that $\overline{n}_{th} = 0.005 \pm 0.005$, and the corresponding population $P_0 = (99.5 \pm 0.5)\%$. The single phonon addition was measured to have an efficiency close to $\kappa = 97$ %, which corresponds to the maximum of the 1^{st} blue sideband Rabi flop between the states $|g,0\rangle \rightarrow |e,1\rangle$, presented in Fig. 5.3. Additional imperfection in efficiency of the full phonon addition step arises form the reshuffling and optical pumping steps performed with 854 nm and 397 nm σ_- beams. This leads to approximately $(2.9 \pm 0.2)\%$ loss of P_1 population which diffuses through photon recoils towards the neighboring number states. The quantitative evaluation of this contribution is described in more detail in Sec. 3.13. The uncertainties of resulting populations are estimated

with use of the Monte-Carlo routine, where the input uncertainties for each data point in the Rabi oscillations were sampled according to expected minimal noise - projection noise.

Next, we evaluate the criteria of non-classicality for different input thermal states after the single quantum addition. Fig. 5.4 shows results of the evaluation of Fano factor $F = \langle(\Delta n)^2\rangle/\langle n\rangle$, Klyshko's criteria for nonclassicality [71], function at the center of the phase space $W(0,0)$, for initial thermal states undergoing an addition of a single quantum with a BSB pulse area of $gt = \pi/2$. The non-classicality is proved by the negativity of measured first order Klyshko criteria K_1. The measured negative value of Winger function $W(0,0) < 0$ additionally proves the quantum non-Gaussian features for all the resulting states. Finally, the negative values of Fano factor point out to the convergence of the resulting statistics towards the sub-Poissonian distributions. We additionally evaluated the witness of quantum non-Gaussian properties based on the estimation of only two neighboring phonon number probabilities, P_1 and P_2. It unambiguously witnesses the QNG aspects for all input thermal states up to mean $\overline{n}_{th} = 4.2$, where the multi-phonon contributions are already too high. The measured states which fulfill the quantum non-Gaussian property are marked with the red tick in Fig. 5.4.

This measurement serves as a proof-of-principle calibration measurement of the phonon addition on thermal states, where we have shown that the generated distributions comply with the theory described by Eq. 5.10 and presented in Fig. 5.1.

5.3 Accumulation of motional non-classicality

In Sec. 5.2, we have shown that the non-classical properties emerge deterministically from initial thermal motional states from a bare single nonlinear phonon addition. However, some of these features are proven weakly within the scale of estimated error. In order to enhance the non-classical and quantum non-Gaussian aspects, we implement the similar process repetitively, while keeping the interaction pulse area gt fixed.

After the re-shuffling and optical pumping step, the resulting state is considered as an input state for the next step and the addition process is repeated, as depicted in Fig. 5.5. We denote a variable k to define the number of repetitions of such addition. After k iterations, the motional populations are measured using the laser spectroscopy on the blue motional sideband.

Fig. 5.6 shows the results of reconstruction of output phonon number distributions $P_n(k)$ for of up to $k = 20$ repetitions of the AJC process for an initial thermal state with a mean phonon number $\overline{n} = 1.19 \pm 0.04$. The results have been

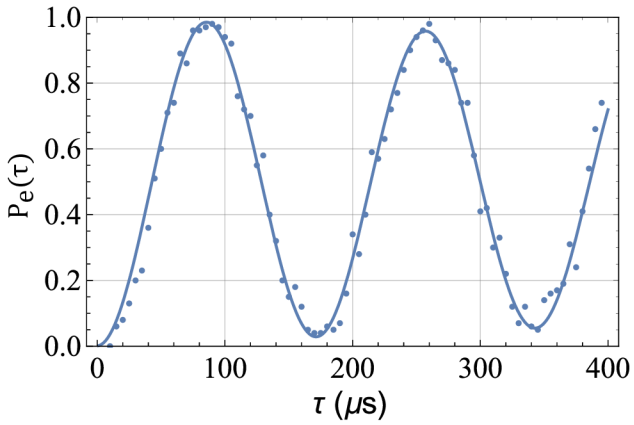

Figure 5.3: Calibration measurement of Rabi oscillations for 1^{st} axial blue sideband at transition $|g,0\rangle \rightarrow |e,1\rangle$. The resulting parameters are $\Omega_0 = 2\pi \times (92 \pm 1)$ kHz, which corresponds to the measured length of the π pulse 91 μs. The maximal excited state population was estimated from a fit as $P_e = 97\%$, which defines the general efficiency of the addition operation.

reconstructed from the measured Rabi oscillations after each displayed number of interaction repetitions k, where the sum maximum defining the truncation of the oscillator Hilbert space was set as $n_{\max} = 7$, according to the 1 % rule applied to the state with highest populations, as described in the section 3.14.1.

The crucial parameter determining the target of the accumulation process lies in the parameter gt, as originally proposed in pioneering work by Blatt, Zirac and Zoller [96]. Specifically, the fulfillment of the relation:

$$gt\sqrt{n+1} = l\pi \tag{5.11}$$

with $l = 1, 2, 3...$ being the whole number coefficient, and n denoting the filter number state. For a particular setting of gt, we manage to generate a cyclic loop in a transition between arbitrary motional states as $|g,n\rangle \rightarrow |e,n+1\rangle \rightarrow |g,n\rangle$. The transition serves as kind of filter in the Fock state basis, which forbids the motional population from states with lower energy to propagate into states that are higher than this particular transition. Such a process leads to the amplification and enhancement of visibility of resulting non-classical properties, which we denote as 'accumulation of non-classicality'.

As for an example, let us theoretically demonstrate this effect for an interaction area $gt = \pi/2$. Substituting this to the Eq. 5.11 and putting $l = 1$, we arrive to the value of $n = 3$. The transition $|g,3\rangle \rightarrow |e,4\rangle \rightarrow |g,3\rangle$ will undergo full period in the two-level system, so the population in the state $|g,3\rangle$ is not depopulated upon AJC pulse. Instead, populations in the lower energy levels

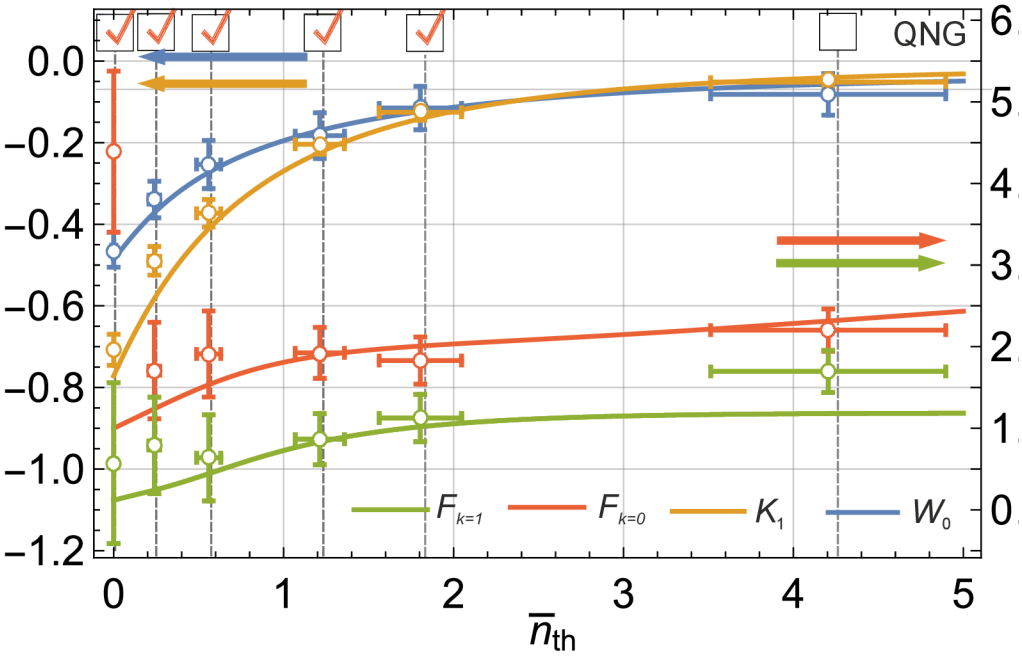

Figure 5.4: The results of evaluation of nonclassicality for the measured phonon number distributions after single nonlinear anti Jaynes-Cummings interaction of atomic mechanical oscillator prepared in thermal state. The Fano factors evaluated for initial and generated phonon populations demonstrate the conversion to sub-Poissonian statistics for states with low initial thermal energy $\overline{n}_{\mathrm{th}}$. The evaluated negative Klyshko's criteria K_1 for each output distribution unambiguously confirm a strong nonclassicality of the generated states for a broad range of initial thermal energies $\overline{n}_{\mathrm{th}}$. In addition, the observed negative values of the Wigner quasi-distribution $W(0,0)$ suggest that the generated state is always non-Gaussian. Moreover, quantum non-Gaussianity criteria (QNG) [22] show impact of multi-phonon contributions. The measures evaluated from the experimental data are displayed as full circles with error bars corresponding to three standard deviations. The solid lines correspond to theoretical predictions for AJC interaction described with Eq. 5.10 with a $gt = \pi/2$ and for given $\overline{n}_{\mathrm{th}}$ with no free fitting parameters.

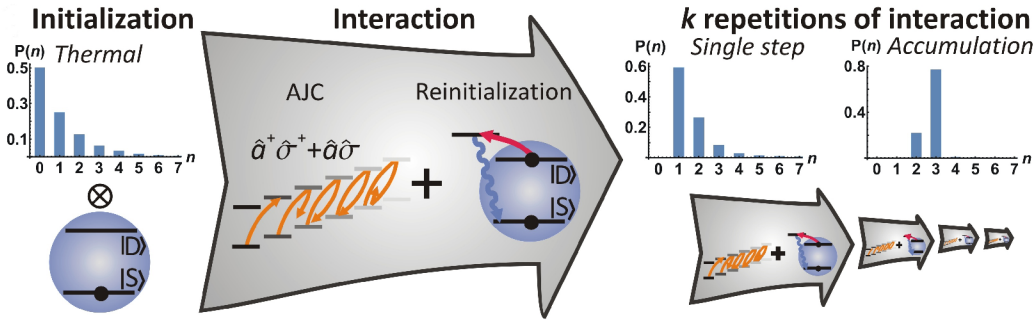

Figure 5.5: A simplified experimental sequence for an unconditional generation of nonclassical states from initially classical thermal population of atomic motion. At the beginning, the two-level system is in the ground state, and the oscillator in thermal state. The nonlinear AJC coupling is followed by a re-initialization of internal atomic population to the $|S\rangle$ level. This process is repeated k-times, leading to the accumulation of motional population in a discrete energy level $|n\rangle$, depending on the value of gt. The final distribution is read out by measurement of the blue motional sideband with a probe of Rabi oscillation.

will be gradually transferred into P_3. In the theoretical limit of infinite phonon addition steps, the population $\sum_{n=0}^{n=3}$ will accumulate in P_3, while the higher levels will arrive to P_{15}, which is an additional discrete solution of Eq. 5.11 resulting for l = 2 and $gt = \pi/2$.

In the similar way, we may derive the limiting populations for other pulse areas gt. For $gt = \pi/\sqrt{3}$, we produce a mixture of states with $n = 2, 11, 47$, for $gt = \pi/\sqrt{5}$, we will have $n = 4, 19, 79$ with coefficients $l = 1, 2, 3$. With $gt = \pi/\sqrt{4} = \pi/2$ we obtain accumulation at $n = 3, 15, 35$ with $l = 1, 2, 3$. Theoretically, with implementation of the particular value of gt, it is possible to engineer any number state filter of interest.

The accumulation is performed for up to $k = 20$ repetitions of the anti-Jaynes-Cummings process, for initial thermal state with $\overline{n} = 1.19 \pm 0.04$. We choose to demonstrate the accumulation for three pulse areas, which were set as $gt = \pi/2 = 91\ \mu$s, $gt = 0.9\pi/2 \approx \pi/\sqrt{5} = 80\ \mu$s and $gt = 1.1\pi/2 \approx \pi/\sqrt{3} = 100\ \mu$s. The lengths of the corresponding applied laser pulses were chosen with respect to the measured duration of the transition between $|g, 0\rangle \rightarrow |e, 1\rangle$.

The resulting statistics, including the evaluated non-classical features are shown in Fig. 5.6. The measured statistics show the convergence of motional population to P_4, P_3 and P_2, respectively. Inf Fig. 5.6 b) corresponding to $gt = \pi/2$, the population converges to $P_3 = 0.52 \pm 0.01$ after 20 accumulation steps.

According to theoretical prediction from the Eq. 5.10, the population should ideally converge to to $P_3 = 0.63$ after 20 accumulation steps. The discrepancy between the measured result and theory can be attributed to a residual offset in an experimental setting of the pulse area gt. With use of $gt = 1.026\,\pi$ in Eq. 5.10, the ideal population after 20 repetitions would be $P_3 = 0.54$, which is in very good agreement with the measured value. Additional limitation is the finite contrast of the applied π-pulse which defines the overall efficiency of the phonon addition operation. The contrast was estimated as $P_e = 0.97$ from measured Rabi oscillations on the ground motional state. The discrepancy between the theory and measurement can be also attributed to the motional heating originating from the potentials at trap electrodes, and also to heating induced by random photon recoils in the process of the reshuffling of the excited state population after each anti-JC pulse. These two effects are also the main reason for occupation of higher motional states and cannot be fully avoided in most experimental scenarios. However, improving the contrast of the π-pulse is feasible and in case of $\kappa = 1$, the motional state $P_3 = 0.66$ could be deterministically generated after 40 repetition steps. Theoretical estimation with an ideal π-pulse contrast and no effects of recoil heating would result in the ideal population $P_3 = 0.88$ after 20 repetition steps and $P_3 = 0.91$ after 43 steps.

The non-classical aspects of generated states are further evidenced in the non-classicality measures, which are displayed in Fig. 5.6 parts d) - f). The figure part d) shows the evolution of mean energy $\overline{n}$ of states generated after k iterations. A decrease of the state's variance with respect to the total energy is evident from the comparison of the evaluated mean energy and Fano factor and provides a complementary signature of convergence towards the energy-localized phonon number state. Fig. 5.6 e) shows the intersection of the Wigner function $W(x, 0)$, which has been evaluated from the measured populations P_n, by considering incoherent sum of partial Wigner quasi-distributions corresponding to the mixed state $\rho_{\mathrm{k}} = \sum_{n=1}^{7} P_{\mathrm{k}}(n) \left|n\right\rangle \left\langle n\right|$. The calculation returns a prediction of the quasi-probability distribution, which would result from a measurement by implementation of random phase shifts of the local oscillator in the reconstruction process. In our considerations, we are interested in the possible observable amount of negative dips in the distribution, which proves that the quasi-probability distribution cannot be expressed as any mixture of the Gaussian states. The verification of the hierarchy of quantum non-Gaussianity criteria is depicted in the inset, where the fully colored squares point to the criteria of selected order, as a function of iterations k. Evaluation within such parameterization suggests that the non-Gaussian properties are indeed amplified for increasing number of iterations.

Finally, we evaluate the entanglement potential EP defined in Eq. 2.51 and

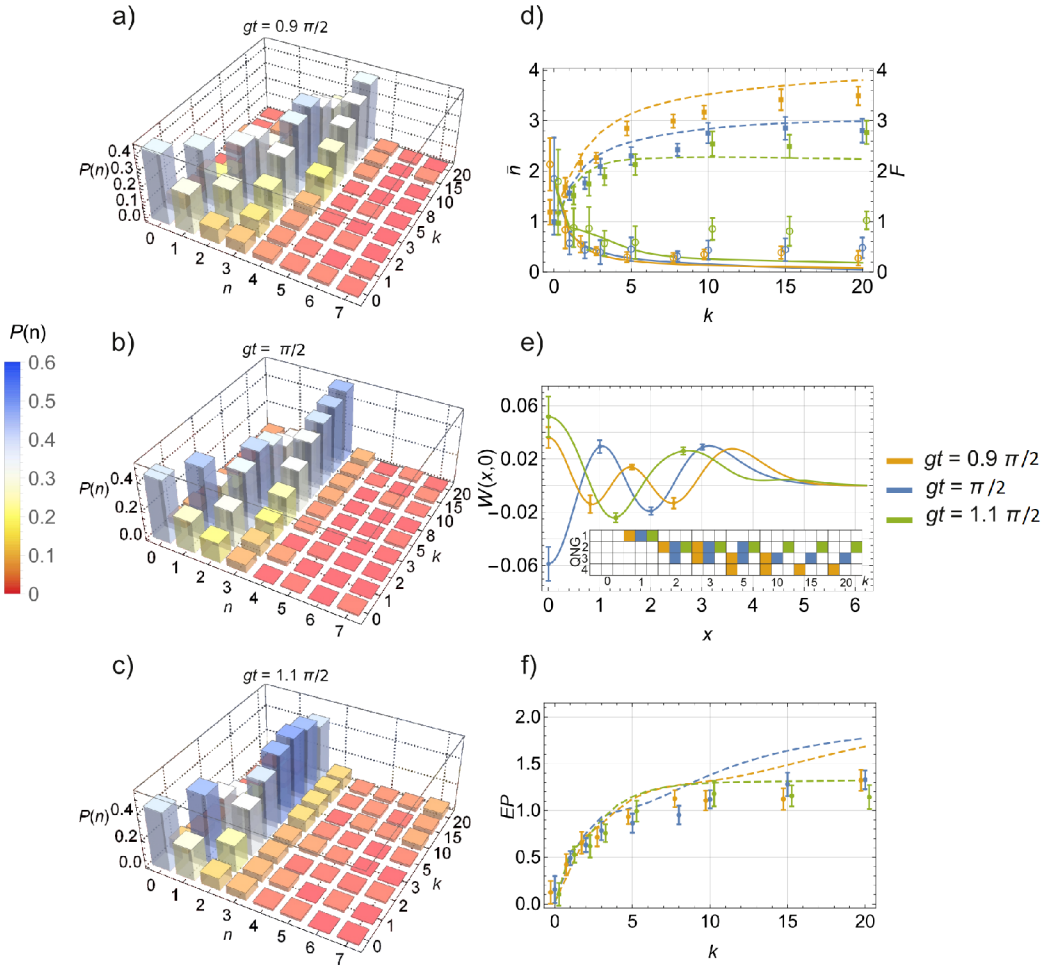

Figure 5.6: Measurement results for nonclassicality accumulation by repetitive application of the nonlinear AJC coupling. Here, $k = 0$ to 20 denotes number of repetitions, applied to the thermal motional state with mean number of phonons $\overline{n}_{\text{th}} = 1.19 \pm 0.04$. The parts a), b) and c) correspond to the generated accumulated statistical distributions for $gt = 0.9 \times \pi/2, gt = \pi/2$ and $gt = 1.1 \times \pi/2$. d) shows the evolution of mean energy and Fano factor, where the decrease for the Fano factor proves the convergence to the number state. Graph e) depicts the intersection of Wigner function $W(x, 0)$, evaluated as a weighted sum of Wigner functions corresponding to ideal number states. The full squares in the inset show the fulfillment of the quantum non-Gaussianity criteria, proving also the accumulation of the non-Gaussian properties with the increasing number of operations. f) shows the increase of entanglement potential calculated from Eq. 2.51 with the number of iterations k.

quantify it using the logarithmic negativity. We can see, that even though the increase of non-classicality sensed in this way is highest for the first step of accumulation, it still monotonically increases with a number of repetitions. Importantly, this effect can be seen even though the measurements include a random and unavoidable diffusion of phonon number statistics due to the excitation and decay on the reshuffling transition with finite Lamb–Dicke parameters. The accumulation process is apparently robust against experimental imperfections and can be applied also to states with high thermal energy resulting from a simple Doppler cooling process, irrespective of additional heating caused by the resetting of electronic state.

6. Non-classical motional states from Jaynes-Cummings interaction

Demonstrated experimental control of the motional state with use of the anti-Jaynes-Cummings interaction led to deterministic generation of non-classicality from thermal states. In this way, high fidelity number states of motion can be generated without the need to fully suppress the thermal energy of the initial state. Implementation of the contrary process corresponding to the phonon absorption has been shown to not just share these deterministic positive quantum aspects, but in addition, it is expected to counter-intuitively benefit from the thermal energy of the initial oscillator state [115].

In the following we describe the initial experimental observations of these aspects by implementation of the repeated phonon absorption on the thermal motional state of a single $^{40}Ca^{+}$ ion. We remind that, when comparing to the phonon annihilation on the photonic mode, the absorption of quanta does not provide any nonclassicality. However, the phonon subtraction can not be viewed as a linear absorption, but instead it serves as a direct source of the modulation of population distribution elements in the Jaynes-Cummings interaction (J-C).

In many ways, the experimental approach is similar as the one described in Chapter 5. However, the populations of generated motional states are fundamentally different. Generally, the states with lower mean energies are created, while having the similar or even slightly improved measures of non-classicality and quantum non-Gaussianity.

6.1 J-C dynamics of accumulation process

In order to theoretically describe the modulation process of motional states' probabilities, we refer to the similar description as the one described in Sec. 5.1. in Eq. 5.7 and Eq. 5.8. A generalized form of the J-C coupling on the arbitrary incoherent mixture of phonon number states distribution can be defined as [115, 116]

$$\rho_r(t) = \sum_{n=0}^{n_{max}} P(n)\left[\cos(gt\sqrt{n})\right]^2 |n\rangle\langle n| + \\ + \sum_{n=0}^{n_{max}} P(n)\left[\sin(gt\sqrt{n})\right]^2 |n-1\rangle\langle n-1| . \quad (6.1)$$

Here, the crucial property to form the non-classical modulation lies again in the pulse area gt.

We consider the example of motional state evolution following the Eq. 6.1 on the population being initially in the state $|g,1\rangle$. The interaction with pulse area $gt = \pi/2$ forms a perfect subtraction of single quantum to the ground state of motion, so that $|g,1\rangle \rightarrow |e,0\rangle$. A more interesting situation happens for $gt = \pi$. The population undergoes the whole cycle, so that $|g,1\rangle \rightarrow |e,0\rangle \rightarrow |g,1\rangle$, returning the same input state of the operation. For repetitive multiple operations with fixed $gt = \pi$, the population of $|g,1\rangle$ will still remain unchanged. The population of higher phonon states will gradually converge towards the state $|g,1\rangle$. In this way, it becomes possible to engineer the accumulation process similar with the one described in Chapter 5, where in the limit of high number of iterations, the population accumulates at the certain energy level n. Generally, the condition to engineer the number state 'filter' can be described with

$$gt\sqrt{n} = l\pi. \quad (6.2)$$

where l is an integer value. In order to focus the accumulation process on the number state n, we set the pulse area as $gt = l\pi/\sqrt{n}$ and apply the sufficient amount of repetitive interactions.

The scaling of solution gt from Eq. 6.2 with integer value of l leads to the accumulation also to higher motional states. Also, the solutions may acquire the similar results for different values of l and n. For the previously discussed example of $gt = \pi$, the solution of Eq. 6.2 returns discrete values of $n = 1, 4, 9, 16$ for $l = 1, 2, 3, 4$. The probability of occupation of these higher order motional states will rise with the increasing mean energy of the initial thermal state, because the higher states will be more populated. For states with low mean energy, the higher contributions can be neglected.

In Fig. 6.1, we depict the simulations of single and repetitive quantum subtractions with Jaynes-Cummings interactions for $gt = \pi$, for two different initial states. In Fig. 6.1 b) and e), we can see that the single subtraction leads to the enhancement of the population P_1 at the cost of higher probabilities P_3, P_4. In the limit of infinite iterations, shown in Fig. 6.1 c), f), the energy levels P_2, P_3 are emptied, and the higher populations converge to P_4, P_9 and P_{16}. At

the same time, the population probability P_0 is left untouched, as the coupling to red sideband does not exist for ground state of motion. We also see that the amount of population accumulated into the higher order number states increases with the energy, so that for higher energies, the operation forms a more complex statistical mixture, also enhancing it's non-classicality measures, which is proved in the measurement described in Sec. 6.2.

6.2 Experimental non-classical states in J-C interaction

We first characterize the state generated with the single subtraction in J-C interaction. Next, this step is repeated k-times. We reconstruct the measured populations of energy levels and compare them to the predicted behavior, which takes into account thermal energy acquired by the system within the sequence duration (see Sec. 3.12), the limited operation efficiency, and the heating by re-shuffling prior to the state readout (see Sec. 3.13).

The experimental sequence starts by preparation of the thermal motional state with energy $\overline{n} = 0.93 \pm 0.06$. The resulting populations are compared with ideal Bose-Einstein distribution reconstructed from the measured state's energy. The pulse area $gt = \pi$ is set by setting the pulse duration to $\tau = 272\ \mu$s. The pulse is applied on the 1^{st} red motional sideband. The phonon number statistics is reconstructed from the blue axial sideband with use of the Eq. 2.40. We repeat the phonon subtraction step up to $k = 5$ iterations, which is already sufficient for amplification of fundamental positive aspects of initial thermal energy.

For the experiment, ground state Rabi frequency was measured as $\Omega_0 = 2\pi \times (60.2 \pm 0.1)$ kHz, Lamb-Dicke parameter $\eta = (0.0611 \pm 0.0002)$ and ground state decay rate $\gamma_0 = 0.42 \pm 0.06$ kHz. A special attention is devoted for experimental estimation of pulse area gt, which has to be set to $gt = \pi$ with high accuracy. This value can be theoretically calculated from the measured Rabi frequency, however, due to the limiting offset in the response of employed electronic elements, the realistic length of the pulse is longer. Physically, the pulse area π corresponds to the whole period of the population transfer between the states $|g,1\rangle \rightarrow |e,0\rangle \rightarrow |g,1\rangle$ at red sideband, as depicted in Fig. 2.2. As the anti-Jaynes-Cummings interaction is described with the very same interaction strength $\eta\Omega_0$ when starting from the excited state, the similar process with exactly same interaction times is performed also on blue sideband as a cycle between the states $|g,0\rangle \rightarrow |e,1\rangle \rightarrow |g,0\rangle$. Therefore, the optimal interaction time $\tau = 272\ \mu$s corresponding to $gt = \pi$ pulse was estimated on the blue sideband and then applied to red sideband interaction from the state $|g,1\rangle$.

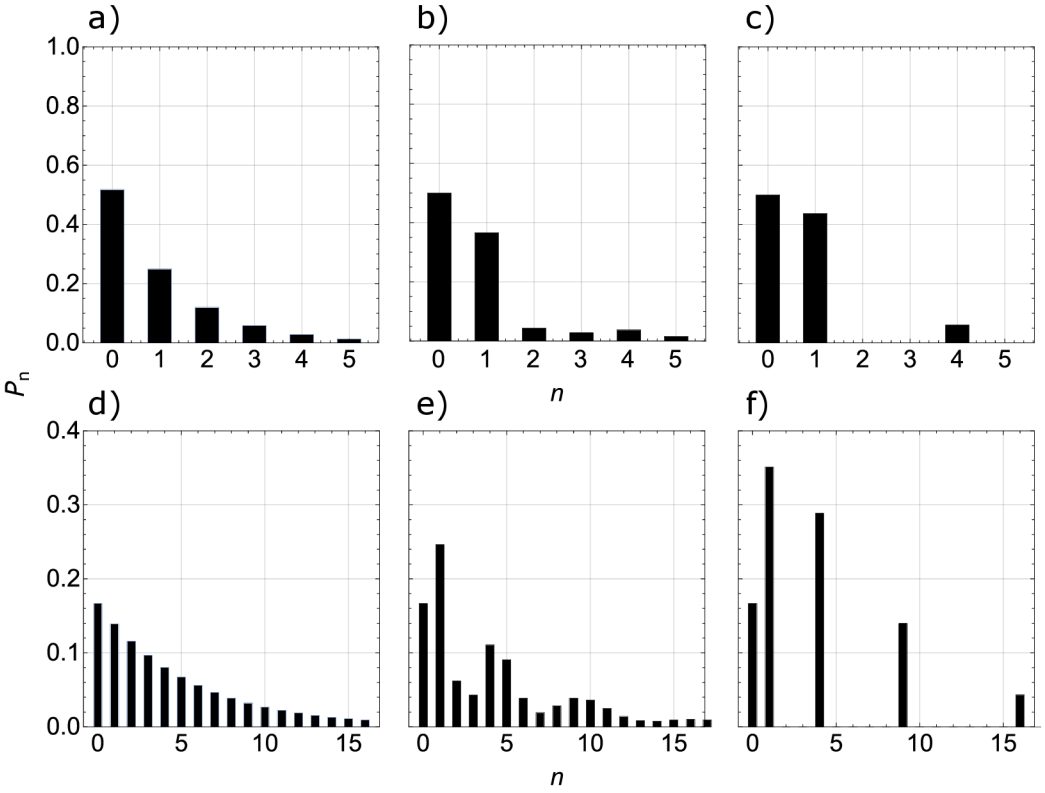

Figure 6.1: A simulation of the result of phonon absorption applied to red sideband with the coupling constant $gt = \pi$. a) shows a thermal distribution with $\overline{n} = 1$. b) plots the resulting state after the single interaction, showing already a significant enhancement in P_1. c) shows a modulation in limit of infinite accumulation steps, leading to accumulation of population at states $|1\rangle$ and $|4\rangle$. The similar scenario is shown in the second row, however now with the initial thermal energy corresponding to $\overline{n} = 5$, depicted in d). A single subtraction already returns the highly non-classical modulation with P_1 larger than P_0, as shown in e). The limiting case f) shows the convergence of populations into $|1\rangle, |4\rangle, |9\rangle, |16\rangle$ which are the results for indexes $l = 1, 2, 3, 4$ in the Eq. 6.2.

The probabilities are shown in Fig. 6.2 with blue columns. After the single interaction step, the process shows a significant enhancement of the population probability P_1. This effect is further amplified by repetitive interactions. The final measurement outcome after five iterations shows a clear convergence towards the states P_1 and P_4, which is in close agreement with a theoretical prediction. The most significantly populated states had probabilities $P_0 = 0.45 \pm 0.01, P_1 = 0.43 \pm 0.01$ and $P_4 = 0.08 \pm 0.02$. The third accumulation maximum, theoretically predicted at P_9, is not observable in this measurement due to the low initial energy. The error bars, corresponding to a single standard deviation, were statistically evaluated from five independent measurements of each state.

The black columns displayed together with the measured data in Fig. 6.2 refer to a theoretical prediction of dynamical process for the initial thermal state. The simulations also contains the known imperfections, describing heating process and imperfect efficiency corresponding to the limited Rabi flop contrast. The blue sideband Rabi flop contrast at the π pulse duration was measured as 95 %. In this case, we assume that 95 % of the initial state's population undergoes the interaction, while the remaining 5 % remains it's initial state. We also estimated that 5.8% of the excited state population undergoes diffusion to the neighboring motional states due to the photon recoils within the reshuffling and optical pumping (see Sec. 3.13). Finally, we assume the axial heating itself, adding the energy of $\Delta\overline{n} = 2.7$ phonons/s withing the time passed from the initialization of the input state. Taking into account all the experimental imperfections, the predicted evolution corresponds to the measured state on the scale of approximately 2 - 3 standard deviations, which is a satisfying result if taking into account the complex nature of the system and the number of free experimental parameters. The aim of this simulation was to merely confirm the conceptual behavior of the phonon number distributions rather than provide their accurate predictions.

The non-classical properties of the generated distributions are characterized by evaluation of entanglement potential (EP) of the generated states and Klyshko criteria. The observed clear increase of the EP with the number of appended accumulation pulses is depicted in Fig. 6.3. The blue points show values resulting from measurement with error bar corresponding to standard deviation retrieved from 5 consecutive measurement runs. The black line shows a theoretical prediction of expected value of EP. The accuracy of the simulation is to some extent limited with truncation of the distribution sum, which performed over all populations predicted to have more than 1 % of motional occupation, as described in Sec. 3.14.1. Theoretically, EP should equal zero for any thermal motional state, since such a state does not contain any non-classicality. The cut of the distribution sum at certain maximal level induces a small offset in entanglement potential.

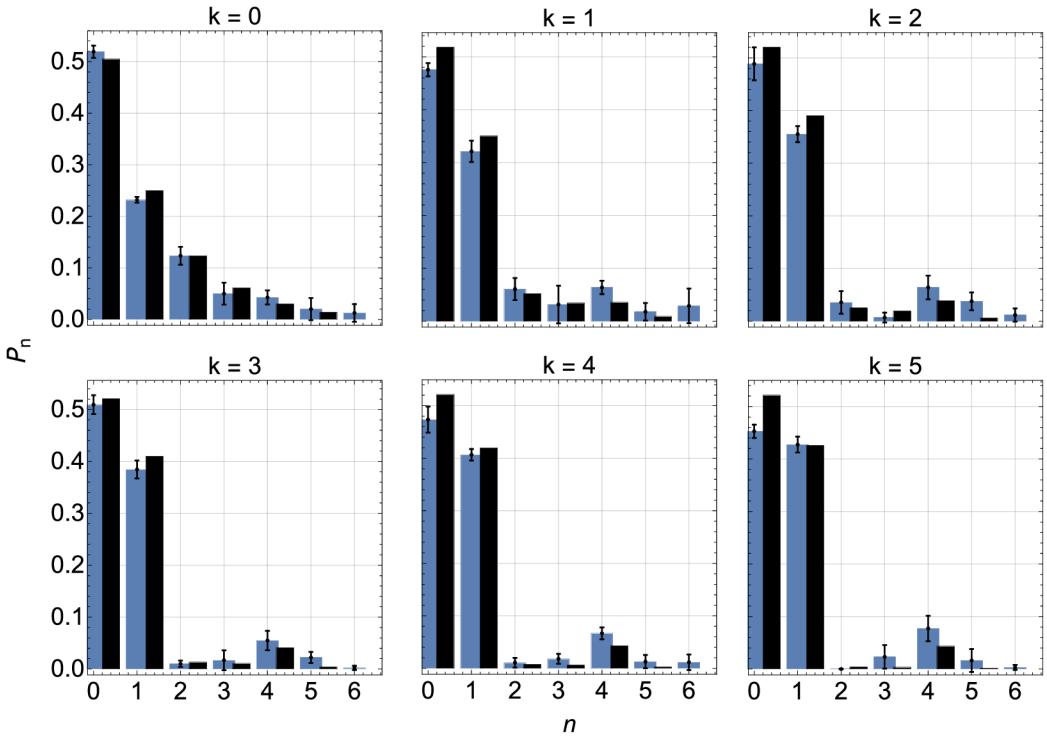

Figure 6.2: Reconstructed phonon distributions for initial thermal state with $\overline{n} = 0.93 \pm 0.06$ undergoing repetitive additions of energy $gt = \pi$ at red axial sideband. Here, n denotes the population level, P_n the occupation probability of the corresponding number state, and k describes the number of repetitive additions. Blue bars depict the measured data, black ones are values resulting from theoretical predictions.

However, the dominant limitation stems from the projection noise resulting from the finite number of experimental repetitions for estimation of the electron state population. To quantify this effect, we employ a Monte-Carlo routine to an ideal population distribution corresponding to thermal state with a given mean thermal energy, and generate an ideal pattern of Rabi oscillations corresponding to it's distribution. We assume that each of the points of this ideal flopping would be measured from 100 projections of a two-level system. In the next step, we variate each point of this flop with the Gaussian distribution, where the standard deviation is defined by the projection noise, similarly as in the experiments described in Chapter 4 and 5. The simulated Rabi oscillations are also used to estimate the expected error for the entanglement potential. For each of the 100 simulations, the EP is calculated and the error bars are taken from the minimal and maximal EP value. These are depicted as gray dashed lines in Fig. 6.3.

The measured data in Fig. 6.4 clearly demonstrate the increase of the EP with

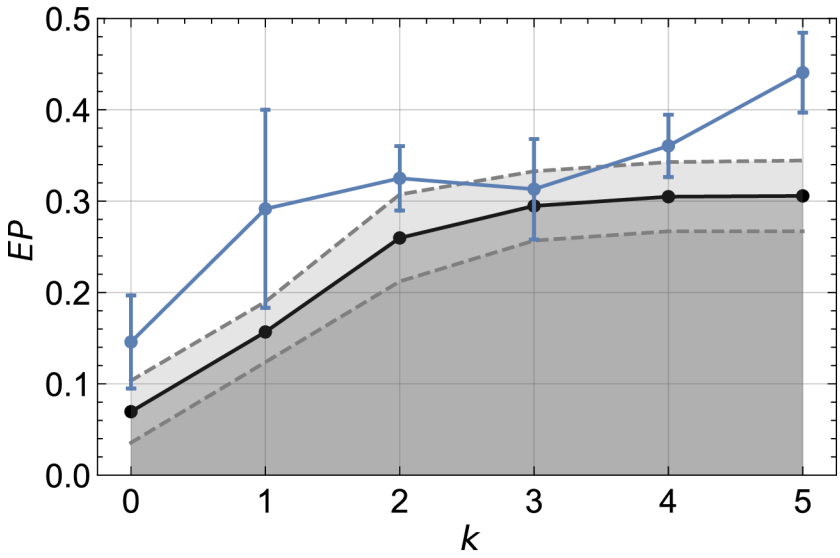

Figure 6.3: Measured and theoretically simulated value of entanglement potential for initial thermal state with $\overline{n} = 0.93 \pm 0.06$, undergoing up to $k = 5$ repetitive phonon subtractions. The measured error bar corresponds to a one standard deviation estimated from 5 independent measurements. The black line shows the predicted values, the gray dashed lines depict the lower and upper bound of the standard simulation error originating from the projection noise (see main text for details).

number of phonon subtractions k applied to the initial thermal state. We measure the values of EP follow the predicted behavior within one standard deviation.

We probe the possible non-classicality by evaluation of Klyshko's criteria of non-classicality, described by an Eq. 2.48 [71]. Such a criteria can form a hierarchy dependent on n, where for each n exists a specific Klyshko criteria. For the current measurement, we evaluate the hierarchy up to the order 7, and depict the result in Fig. 6.4. The values of K_1 and K_4 show a statistically significant amount of negativity. The negative value is apparent even after the single phonon subtraction, and gradually increases with the added accumulation steps. Physically, the negative value points to the fact that the occupation probabilities P_1 and P_4 are significantly larger than at least one of the neighboring oscillator states. The effect is much more pronounced for K_1, in agreement with the expectation of the dominant population of P_1 and suppressed population in P_2.

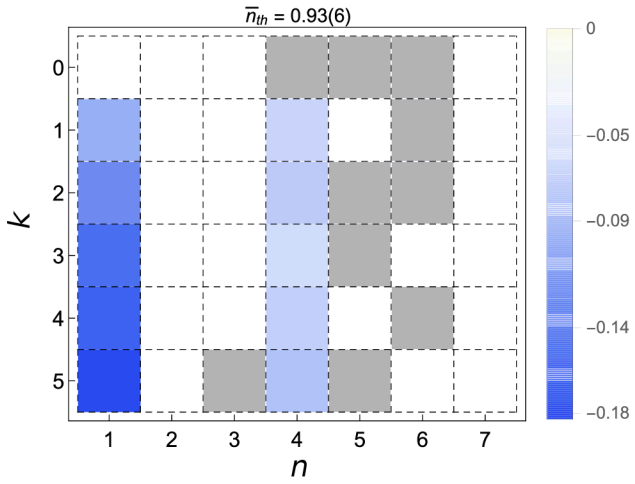

Figure 6.4: Evaluated hierarchy of Klyshko criteria K_n. The horizontal axis denotes the order of the Klyshko criteria n, the vertical line then number of accumulation pulses increasing from top to bottom. The columns related to P_1 and P_4 prove a clear non-classical nature of the generated states. The gray squares show the Klyshko parameter values, where we measured the negative values, but the negativity was smaller than single standard deviation. The white squares denote positions where the Klyshko parameter resulted positive.

6.3 Thermally induced non-classical features

We explore the effect of phonon subtraction and accumulation for states with various initial thermal energies. We prepare five additional thermal states, which together with the already described measurement (Sec 6.2) form a set of total six measurements. For each initial thermal state, we perform the sequence of five repetitive subtractions, which became sufficient for enhancement of the observability of the target phenomena relevant for thermally stimulated nonclassicality.

The plot chart in Fig. 6.5 depicts the dynamics for three initial thermal energies. The rows represent low $\overline{n} = 0.14 \pm 0.03$, intermediate $\overline{n} = 2.0 \pm 0.1$ and high $\overline{n} = 2.9 \pm 0.3$ initial thermal energy. The first column shows the measured thermal distributions, the second one states after single interaction, and the third the distribution after $k = 5$ repetitive interactions. The data processing and simulations were performed following the recipe described Sec. 6.2.

The overall comparison of dynamics occurring for various energies shows that the dynamics of accumulation process applied to states with increasing initial energies leads to generation of number states which correspond to filters

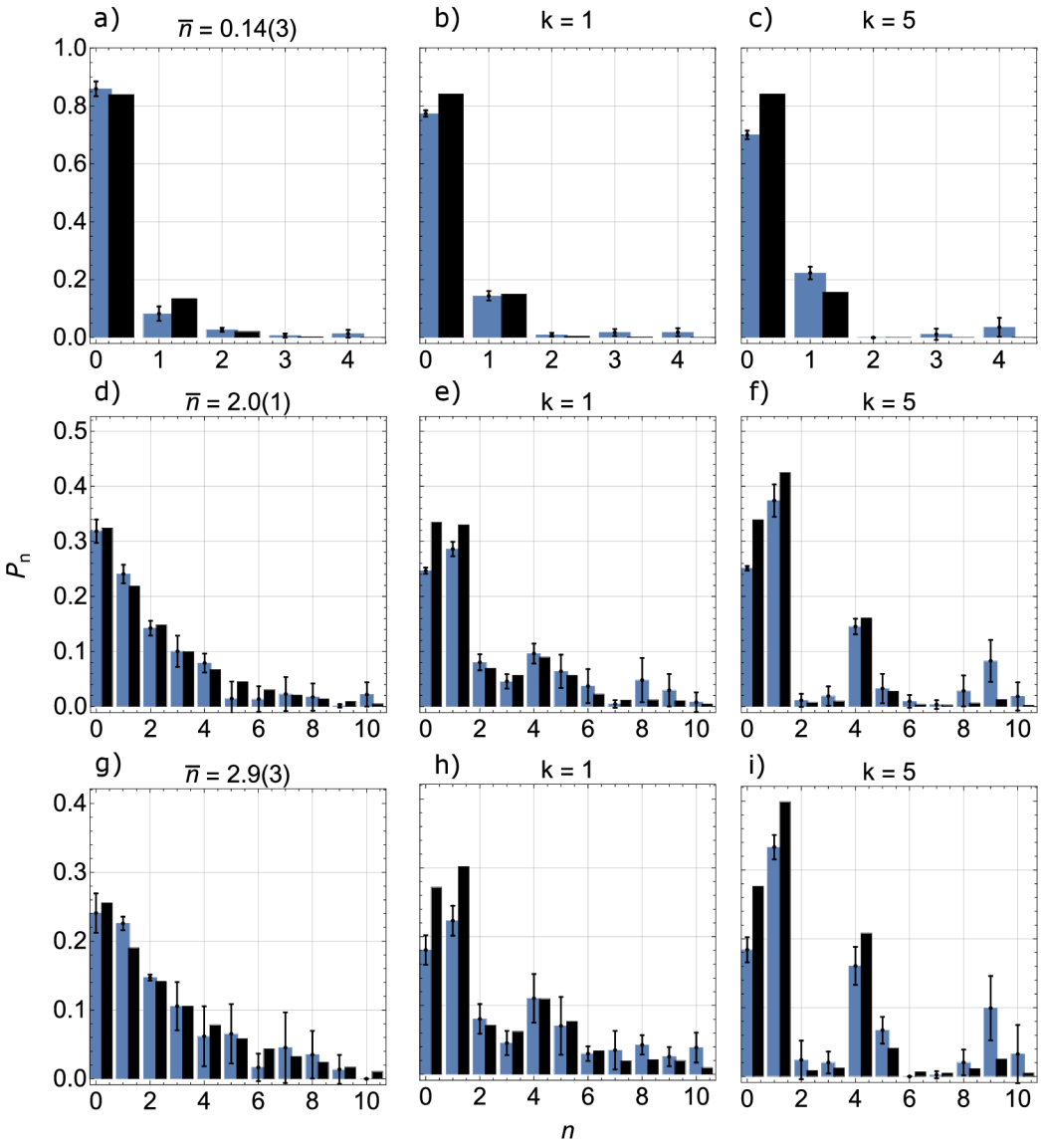

Figure 6.5: Measurement of the repeated phonon absorption for different input thermal energies for $gt = \pi$. States with increasing energy form a more pronounced non-classical modulations, where the solutions corresponding to higher multiples of $gt = l\pi$ become evident. The errors correspond to a single standard deviation resulting from statistical evaluation of five independent measurements. Theoretical simulation including the simulation of the effect of projection noise is depicted by black bars.

based on pulse areas gt of higher order multiplies of π. For the state with a low initial energy $\overline{n} = 0.14 \pm 0.03$, we see that the effect phonon absorption is generally very weak, performing in limiting case only around 10 % of population transfer into the state P_1, while significant part of this can be contributed to the effect of heating. For both of the additional measurements, initiating from thermal states $\overline{n} = 2.0 \pm 0.1$ and $\overline{n} = 2.9 \pm 0.3$, we were able to observe the convergence towards the state P_4 with a significant strength, see Fig. 6.5 f) and i). Moreover, we can observe a significant enhancement of probability P_1 even after the single interaction, unlike in case of low initial energy, as depicted in Fig 6.5 e), h). For the result in Fig. 6.5 f), we measure $P_1 = 0.37 \pm 0.03$ and $P_4 = 0.14 \pm 0.02$, and even the third maximum $P_9 = 0.08 \pm 0.04$. For a highest initial thermal energy, the state after five iterations shown in Fig. 6.5 i) returns $P_1 = 0.33 \pm 0.03, P_4 = 0.16 \pm 0.03$ and $P_9 = 0.10 \pm 0.05$. From the presented results, it is clearly apparent that the states with high initial thermal energy are able to form the more complex statistical mixtures than states with low $\overline{n}$.

In order to systematically evaluate the corresponding enhancement of nonclassical features of generated states, we evaluate the Klyshko hierarchy and entanglement potential measures. The hierarchy is depicted in the plot matrix in Fig. 6.6. The horizontal axis defines the order of the Klyshko criteria n which is under the probe. Vertical axis label refers to the initial thermal state $\overline{n}_{\mathrm{th}}$. The $k = 0$ refers to initial thermal states, $k = 1$ corresponds to a single absorption, and $k = 5$ to five cycles in total. The results show that for the increasing number of iterations, the negativity in Klyshko parameters K_1 and K_4 increases, pointing to the increasing non-classicality which is being accumulated in the system. The accumulation in particular states P_1 and P_4 also complies with the expected trend of convergence towards solutions of Eq. 6.2 where $gt = \pi$.

The estimated entanglement potential is displayed in Fig. 6.7 a). The results prove both the enhancement by number of accumulation steps and with increasing thermal energy. The red points in the Fig. 6.7 show the EP for thermal states, which grows with mean energy due to the finite measurement projection noise, as described in Sec. 6.2.

We simulate this effect with use of the Monte-Carlo simulation, similarly as for the previous measurement in Sec. 6.2, and find out that the measured offset in entanglement potential quantitatively agrees with a theoretical prediction.

The blue and yellow points in Fig 6.7 a) corresponding to states after $k = 1$ and $k = 5$ phonon subtractions, show the measured values of EP well beyond the numbers corresponding to thermal states. At the same time, estimated state energy for $k = 0, 1, 5$ iterations remains similar, as depicted in Fig 6.7 b), proving that the effect of non-classicality enhancement clearly originates from the performed interactions, and it is thus not an effect of increasing thermal state energy. Finally, the Fig. 6.7 proves the most crucial aspect, which is a the growth

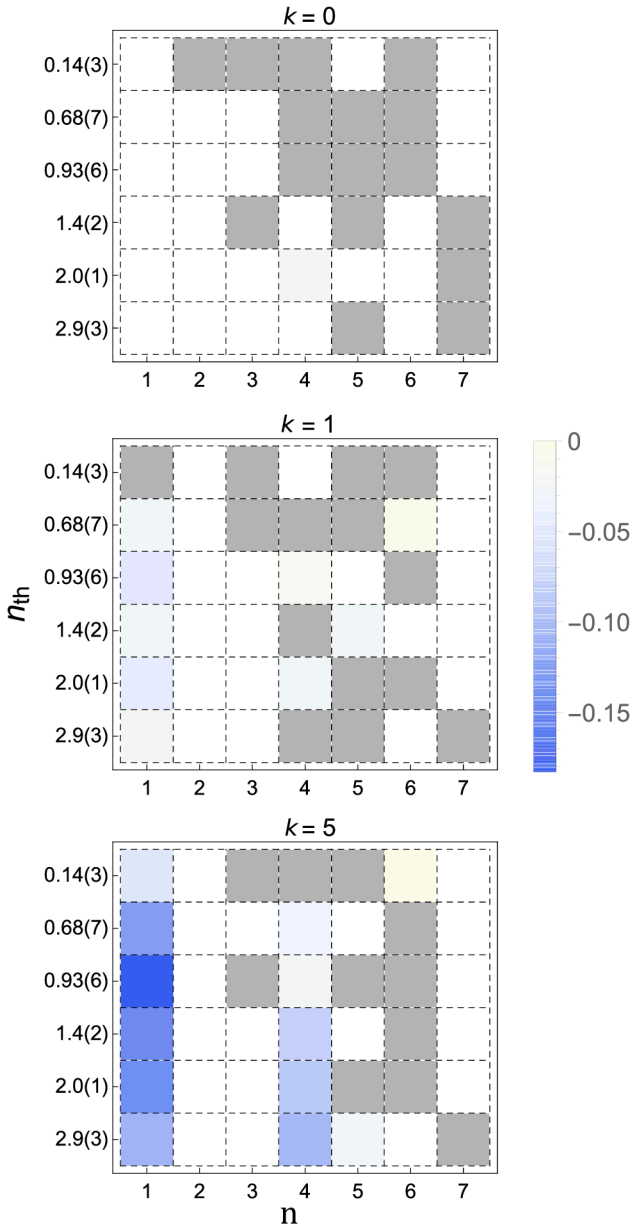

Figure 6.6: Matrices of estimated Klyshko non-classicality criteria. The vertical axis denotes the initial thermal energies of states $\overline{n}_{th}$. The horizontal variable n has a meaning of the Klyshko criteria order. From left to right, the plots show the results for initial thermal states ($k = 0$), distributions undergoing a subtraction of single phonon ($k = 1$), and finally the accumulation of five subtraction processes ($k = 5$). The grey squares show results, where small negative value was evaluated, which did not exceed the interval of a single standard deviation. For all the employed initial thermal states, except for the one with lowest energy, we observe the effect of non-classicality growth as a function o k. The increasing energy contributes especially to enhancement of the criteria K_4.

of EP with the increasing thermal energy of the input state. This is manifested as an increasing delta between measured EP corresponding to $k = 1$ and $k = 5$ datasets. For example, for the state with initial thermal energy $\overline{n} = 0.68(7)$ the $\Delta_{\mathrm{EP}} = 0.16$, but for the state with $\overline{n} = 2.9(3)$ it is already much higher, $\Delta_{\mathrm{EP}} = 0.42$.

We note that, results presented in this Chapter are preliminary, though sufficient enough to prove the validity of the states generation and it's usability to prove the quantum non-Gaussian properties. In order to provide the satisfactory comparison of the generated states with their theoretical prediction, the experiment has been currently instantiated with use of the new laser setup with improved coherence properties, stabilized magnetic field in the trap setup and other improvements.

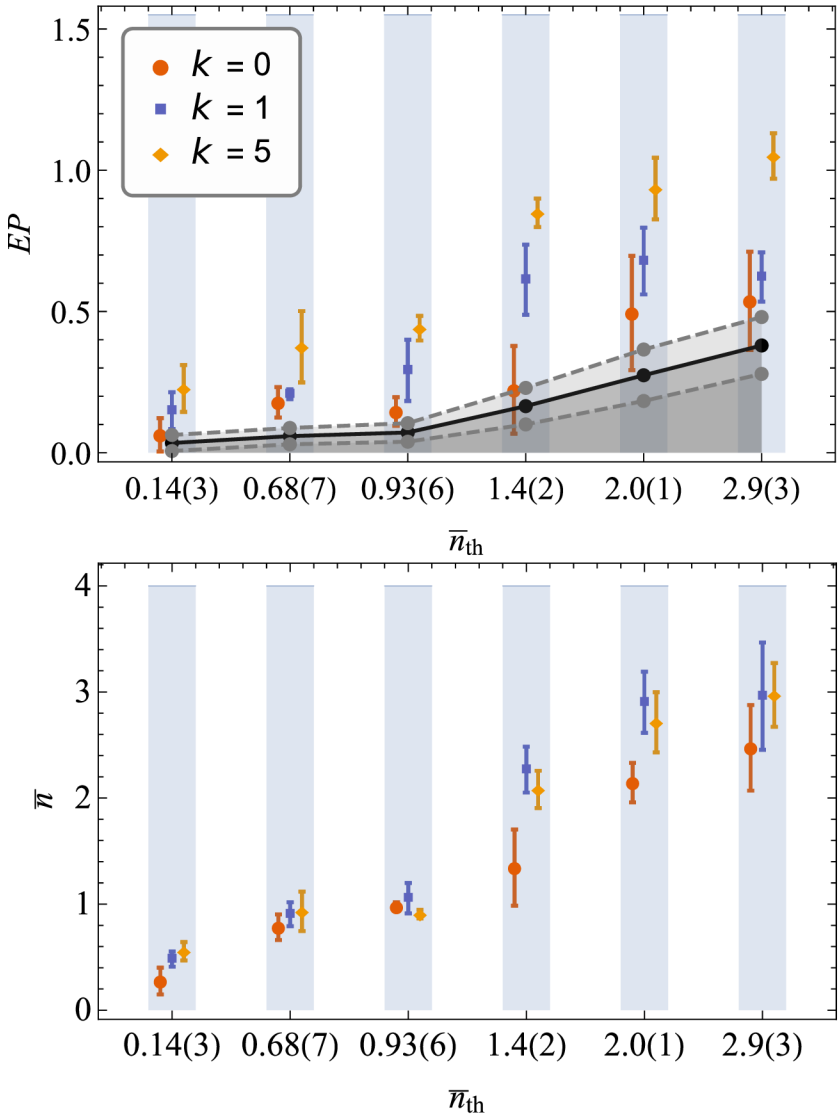

Figure 6.7: a) Entanglement potential and b) mean energies as $\overline{n} = \sum_n nP_n$ of the initial states (red) undergoing a single (blue) and five phonon absorption cycles (yellow). The trend in measured EP suggests the enhancement of non-classicality for both increasing energy and the number of iterations. At the same time, the energy difference between datasets of $k = 1$ and $k = 5$ (in b)) is relatively small, which proves that the enhancement of EP shown in a) indeed comes from the phonon subtraction, and it is thus not an artifact from an increasing Hilbert space size.

7. Conclusions

Further development of quantum technology and its applications depends on the quality, costs and robustness of experimental resources that must be conclusively proved. For bosonic implementations of quantum technology, including mechanical experiments with trapped ions, quantum non-Gaussian states of phononic oscillators are highly needed as resources. The Fock states are the most fundamental quantum non-Gaussian elements, challenging for many bosonic platforms but already providing tools for quantum force sensing beyond the standard quantum limit. Moreover, they are critical elements for building Fock state superpositions with much broader applications in quantum error correction, quantum sensing and interferometry, quantum simulations, and quantum thermodynamics.

The presented work provides a complex set of experimental measurements which focuses on generation and characterization of quantum states implemented on motional degree of freedom of the trapped ion system. We employed the broadly used method of phonon addition and subtraction at 1^{st} motional sidebands [19], and we extended it's application to create complex statistical mixtures. We have used the criteria of non-classicality and genuine quantum non-Gaussianity to characterize the quantum states and analyzed their robustness to the addition of thermal energy. We have further proved that initial thermal energy can be beneficial for the observable non-classical features, which is in contrast with conventional intuition on conditions for sources of nonclassicality to be well isolated from the surrounding environment.

We have focused on generation of high number states and we probed their properties while undergoing the controllable thermalization. We have applied the specifically developed hierarchy of quantum non-Gaussianity criteria [21, 23], which provides a tool to qualitatively express the amount of non-classical features which are being present in the phonon population distribution. We measured and evaluated the depth of the quantum non-Gaussian features, which characterizes the minimal amount of thermal energy added to the system to destroy the observability of quantum state's non-Gaussianity. We additionally performed the controllable experimental heating of ion to precisely calibrate this

effect on mechanical system. For the most robust state $|1\rangle$, we have measured the limiting energy preserving the non-Gaussian properties as $\overline{n} = 0.31$, while for increasing energy of measured number states, this gradually drops down to the energy of 0.02 phonons measured for number state $|10\rangle$. Still, despite the decreasing robustness with respect to the motional heating, we have estimated by calculation of Fisher information and evaluation of the metrological advantage, that employment of the higher order number states provides the potential enhancement of the accuracy of phase insensitive sensing of small coherent displacement. The highest metrological advantage was evaluated for the generated state $|8\rangle$, for higher state $|10\rangle$ was lost due to the large uncertainty in population distribution. Together, the presented routine of characterizing the motional states with genuine QNG criteria hierarchy proves to be a feasible tool for conclusive, hierarchical and sensitive evaluation of Fock state properties.

The second experiment extends the method of motional engineering to application of repetitive anti Jaynes-Cummings interactions. We have implemented the scheme, which was theoretically proposed already in 1995 by Blatt et. al. [96] and within the best of our knowledge, it was not experimentally verified up to date. We have shown that the repetitive application of fixed length pulse on the blue axial sideband leads to the dynamical accumulation of motional population into a particular number state, which can be controllably tuned by varying the length gt of the employed interaction pulse. Crucially, this generation method manages to overcome the fundamental requirement of majority of other protocols for preparation of Fock states, which is the minimization of the initial state entropy.

By evaluation of the Klyshko criteria and entanglement potential, we proved that the capability to detect non-classcial features increase with high energy of the initial thermal state, which becomes apparent even for the single added quantum (see Fig. 5.4). We probed the dynamics of repetitive phonon emission processes, which were measured for various pulse length, where each of the dynamics shows the convergence towards a different number state, particularly towards $|2\rangle, |3\rangle, |4\rangle$ for pulse areas $gt = 0.9 \times \pi/2, \pi/2$ and $1.1 \times \pi/2$. We also proved that the repetitive addition of energy enhances the measured amount of entanglement potential and the Fano factor which shows the convergence to the sub-Poissonian, thus non-classical statistics.

In the last presented experiment we demonstrated the accumulation of non-classicality by addressing the red motional sideband. The point of the demonstrated physics lies in the possibility to generate a non-classical quantum state even by the absorption of phonon, which is in striking contrast to photon annihilation process in photonic quantum systems. We have proved that the presence of non-classical and quantum non-Gaussian features is directly driven by increasing energy of initial thermal state. For various thermal distributions at

input, we estimated the resulting distributions after a single and five repetitive phonon absorptions, and we proved that estimated entanglement potential grows with the initial thermal energy. The estimated hierarchy of Klyshko criteria illustrated increase of non-classicality with thermal energy and number of iterations, and also shows the convergence of the distribution towards the number states $|1\rangle$ and $|4\rangle$, which corresponds to a theoretical prediction calculated for many phonon absorptions.

We foresee the application of the presented results mainly in improvement of methods used for quantum enhanced sensing [24]. The method of states's characterization using the genuine QNG criteria also provides a crucial milestone of experimental witnessing the intrinsic properties of highly non-classical states. Such states are broadly applicable in fields of optical frequency metrology [114, 117], quantum error correction [112] and test of quantum thermodynamical phenomena [118, 119]. Together with the recently published work demonstrating the number state generation approaching $|100\rangle$ on the same experimental platform, [25], the set of here demonstrated genuine QNG criteria will allow for the optimization and comparison of these quantum states across different experimental platforms [120, 121]. The realized experiments involving the motional accumulation by repetitive interactions demonstrates the unprecedented possibility to deterministically acquire the quantum non-Gaussian properties in thermal states, and thus promises a feasible bypass for no-go theorem for Fock states processing [122]. The experimental routine may be directly extended into non-linear couplings with solid-state mechanical oscillators [109, 123–125].

A space for potential improvement lies in the possible enhancement of the set trapping frequencies, which would allow to speed up the stage of the state preparation. Also, the increase in laser power leading to increase in Rabi frequency would decrease a period of probed Rabi oscillations. Together, these two effects would accelerate the motional dynamics, while at the same time suppressing the diffusion to higher energies induced by a thermal heating process. A crucial technical issue which limited all experimental processes lied in non-ideal contrast of the employed Rabi flops, and also in high damping of the Rabi oscillations under probe. The possible improved electronic intensity stabilization and the fiber noise cancellation method could reduce this decay, which could lead to higher flop contrast and thus to more deterministic phonon gates and also more precise estimation of phonon statistics. Additionally, we expect that the employment of the passive magnetic shielding in form of the external box will decrease the externally induced fluctuations of magnetic fields, which would also result towards increased coherence of the two-level system probe. During the preparation of the thesis, these improvements were partially implemented, which already led to improvement of the presented Ramsey

coherence times on $4S_{1/2} \rightarrow 3D_{5/2}$ transition to beyond 10 ms.

References

1 A. Einstein:
'Über einen die erzeugung und verwandlung des lichtes betreffenden heuristischen gesichtspunkt',
Annalen der Physik **322**, 132–148 (1905).

2 E. Schrödinger:
'An undulatory theory of the mechanics of atoms and molecules',
Phys. Rev. **28**, 1049–1070 (1926).

3 E. Schrödinger:
'Are there quantum jumps? part ii',
The British Journal for the Philosophy of science **3**, 233–242 (1952).

4 W. Paul and H. Steinwedel:
'Ein neues massenspektrometer ohne magnetfeld',
Zeitschrift für Naturforschung A **8**, 448–450 (1953).

5 A. L. Schawlow and C. H. Townes:
'Infrared and optical masers',
Phys. Rev. **112**, 1940–1949 (1958).

6 W. Neuhauser, M. Hohenstatt, P. Toschek and H. Dehmelt:
'Optical-sideband cooling of visible atom cloud confined in parabolic well',
Physical Review Letters **41**, 233 (1978).

7 D. J. Wineland, R. E. Drullinger and F. L. Walls:
'Radiation-pressure cooling of bound resonant absorbers',
Physical Review Letters **40**, 1639 (1978).

8 W. Neuhauser, M. Hohenstatt, P. Toschek and H. Dehmelt:
'Localized visible ba+ mono-ion oscillator',
Physical Review A **22**, 1137 (1980).

9 H. Jayakumar, A. Predojević, T. Huber, T. Kauten, G. S. Solomon and G. Weihs:
'Deterministic photon pairs and coherent optical control of a single quantum dot',
Physical review letters **110**, 135505 (2013).

10 J. M. Gambetta, J. M. Chow and M. Steffen:
'Building logical qubits in a superconducting quantum computing system',
npj Quantum Information **3**, 1–7 (2017).

11 R. Stárek, M. Miková, I. Straka, M. Dušek, M. Ježek, J. Fiurášek and M. Mičuda:
'Experimental realization of swap operation on hyper-encoded qubits',
Optics express **26**, 8443–8452 (2018).

12 S. Konno, W. Asavanant, K. Fukui, A. Sakaguchi, F. Hanamura, P. Marek, R. Filip, J.-i. Yoshikawa and A. Furusawa:
'Non-clifford gate on optical qubits by nonlinear feedforward',
arXiv preprint arXiv:2103.10644 (2021).

13 A. Sørensen and K. Mølmer:
'Quantum computation with ions in thermal motion',
Phys. Rev. Lett. **82**, 1971–1974 (1999).

14 L. Slodička:
'Single ion-single photon interactions in free space',
(2013).

15 A. D. Ludlow, M. M. Boyd, J. Ye, E. Peik and P. O. Schmidt:
'Optical atomic clocks',
Rev. Mod. Phys. **87**, 637–701 (2015).

16 C. D. Bruzewicz, J. Chiaverini, R. McConnell and J. M. Sage:
'Trapped-ion quantum computing: progress and challenges',
Applied Physics Reviews **6**, 021314 (2019).

17 J. Zhang, G. Pagano, P. W. Hess, A. Kyprianidis, P. Becker, H. Kaplan, A. V. Gorshkov, Z.-X. Gong and C. Monroe:
'Observation of a many-body dynamical phase transition with a 53-qubit quantum simulator',
Nature **551**, 601–604 (2017).

18 S. Wehner, D. Elkouss and R. Hanson:
'Quantum internet: a vision for the road ahead',
Science **362** (2018).

19 D. Leibfried, R. Blatt, C. Monroe and D. Wineland:
'Quantum dynamics of single trapped ions',
Reviews of Modern Physics **75**, 281 (2003).

20 R. J. Glauber:
'Coherent and incoherent states of the radiation field',
Physical Review **131**, 2766 (1963).

21 R. Filip and L. Mišta Jr:
'Detecting quantum states with a positive wigner function beyond mixtures of gaussian states',
Physical review letters **106**, 200401 (2011).

22 I. Straka, L. Lachman, J. Hloušek, M. Miková, M. Mičuda, M. Ježek and R. Filip:
'Quantum non-gaussian multiphoton light',
npj Quantum Information **4**, 1–5 (2018).

23 L. Lachman, I. Straka, J. Hloušek, M. Ježek and R. Filip:
'Faithful hierarchy of genuine n-photon quantum non-gaussian light',
Physical review letters **123**, 043601 (2019).

24 F. Wolf, C. Shi, J. C. Heip, M. Gessner, L. Pezzè, A. Smerzi, M. Schulte, K. Hammerer and P. O. Schmidt:
'Motional fock states for quantum-enhanced amplitude and phase measurements with trapped ions',
Nat. Commun. **10**, 1–8 (2019).

25 K. C. McCormick, J. Keller, S. C. Burd, D. J. Wineland, A. C. Wilson and D. Leibfried:
'Quantum-enhanced sensing of a single-ion mechanical oscillator',
Nature **572**, 86–90 (2019).

26 M. Gessner, A. Smerzi and L. Pezzè:
'Metrological nonlinear squeezing parameter',
Phys. Rev. Lett. **122**, 090503 (2019).

27 C. Flühmann, T. L. Nguyen, M. Marinelli, V. Negnevitsky, K. Mehta and J. P. Home:
'Encoding a qubit in a trapped-ion mechanical oscillator',
Nature **566**, 513 (2019).

28 M. H. Michael, M. Silveri, R. Brierley, V. V. Albert, J. Salmilehto, L. Jiang and S. M. Girvin:
'New class of quantum error-correcting codes for a bosonic mode',
Physical Review X **6**, 031006 (2016).

29 L. Hu, Y. Ma, W. Cai, X. Mu, Y. Xu, W. Wang, Y. Wu, H. Wang, Y. Song, C.-L. Zou et al.:
'Quantum error correction and universal gate set operation on a binomial bosonic logical qubit',
Nature Physics **15**, 503–508 (2019).

30 P. Campagne-Ibarcq, A. Eickbusch, S. Touzard, E. Zalys-Geller, N. E. Frattini, V. V. Sivak, P. Reinhold, S. Puri, S. Shankar, R. J. Schoelkopf et al.:
'Quantum error correction of a qubit encoded in grid states of an oscillator',
Nature **584**, 368–372 (2020).

31 A. Ghosh, W. Niedenzu, V. Mukherjee and G. Kurizki:
'Thermodynamic principles and implementations of quantum machines',
Thermodynamics in the Quantum Regime: Fundamental Aspects and New Directions, edited by F. Binder, LA Correa, C. Gogolin, J. Anders, and G. Adesso (Springer International Publishing, Cham, 2018) pp, 37–66 (2018).

32 G. Maslennikov, S. Ding, R. Hablützel, J. Gan, A. Roulet, S. Nimmrichter, J. Dai, V. Scarani and D. Matsukevich:
'Quantum absorption refrigerator with trapped ions',
Nature communications **10**, 1–8 (2019).

33 M.-L. Cai, Z.-D. Liu, W.-D. Zhao, Y.-K. Wu, Q.-X. Mei, Y. Jiang, L. He, X. Zhang, Z.-C. Zhou and L.-M. Duan:
'Observation of a quantum phase transition in the quantum rabi model with a single trapped ion',
Nature communications **12**, 1–8 (2021).

34 L. Podhora, T. Pham, A. Lešundák, P. Obšil, M. Čížek, O. Číp, P. Marek, L. Slodička and R. Filip:
'Unconditional accumulation of nonclassicality in a single-atom mechanical oscillator',
Advanced Quantum Technologies **3**, 2000012 (2020).

35 L. Podhora, L. Lachman, T. Pham, A. Le šundák, O. Číp, L. Slodi čka and R. Filip:
'Quantum non-gaussianity of multiphonon states of a single atom',
Phys. Rev. Lett. **129**, 013602 (2022).

36 S. M. Brewer, J.-S. Chen, A. M. Hankin, E. R. Clements, C.-w. Chou, D. J. Wineland, D. B. Hume and D. R. Leibrandt:
'Al+ 27 quantum-logic clock with a systematic uncertainty below 10- 18',
Physical review letters **123**, 033201 (2019).

37 B. A. C. O. N. B. Collaboration:
'Frequency ratio measurements at 18-digit accuracy using an optical clock network',
Nature **591**, 564–569 (2021).

39 J. Meija, T. B. Coplen, M. Berglund, W. A. Brand, P. D. Bièvre, M. Gröning, N. E. Holden, J. Irrgeher, R. D. Loss, T. Walczyk and T. Prohaska:
'Isotopic compositions of the elements 2013 (iupac technical report)',
Pure and Applied Chemistry **88**, 293–306 (2016).

40 N. Stone:
'Nuclear magnetic dipole and electric quadrupole moments: their measurement and tabulation as accessible data',
Journal of Physical and Chemical Reference Data **44**, 031215 (2015).

41 P. Barakhshan, A. Marrs, B. Arora, R. Eigenmann and M. S. Safronova,
Portal for High-Precision Atomic Data and Computation (version 1.0). University of Delaware, Newark, DE, USA. URL: `https://www.udel.edu/atom` [January 2021].

42 M. Hettrich, T. Ruster, H. Kaufmann, C. F. Roos, C. T. Schmiegelow, F. Schmidt-Kaler and U. G. Poschinger:
'Measurement of dipole matrix elements with a single trapped ion',
Phys. Rev. Lett. **115**, 143003 (2015).

43 Z. Meir, M. Sinhal, M. S. Safronova and S. Willitsch:
'Combining experiments and relativistic theory for establishing accurate radiative quantities in atoms: the lifetime of the $^2P_{3/2}$ state in $^{40}Ca^+$',
Phys. Rev. A **101**, 012509 (2020).

44 A. Kreuter, C. Becher, G. P. T. Lancaster, A. B. Mundt, C. Russo, H. Häffner, C. Roos, W. Hänsel, F. Schmidt-Kaler, R. Blatt and M. S. Safronova:
'Experimental and theoretical study of the $3d\ ^2D$–level lifetimes of $^{40}Ca^+$',
Phys. Rev. A **71**, 032504 (2005).

45 D. A. Steck:
Quantum and atom optics,
2007.

46 M. O. Scully and M. S. Zubairy:
Quantum optics,
1999.

47 M. A. Nielsen and I. Chuang:
Quantum computation and quantum information,
2002.

48 C. Roos:
'Controlling the quantum state of trapped ions',
PhD thesis (2000).

49 M. Guggemos:
'Precision spectroscopy with trapped 40ca+ and 27al+ ions',
PhD thesis (2017).

50 P. Obšil:
'Nonclassical and coherent emission from trapped ion crystals',
PhD thesis (2021).

51 A. Lešundák:
'Distance measurements with mode-filtered frequency comb and analysis of fluorescence from trapped ion at modulated dark state',
PhD thesis (2019).

52 J. J. Sakurai and E. D. Commins:
Modern quantum mechanics, revised edition,
1995.

54 C. Blockley, D. Walls and H. Risken:
'Quantum collapses and revivals in a quantized trap',
EPL (Europhysics Letters) **17**, 509 (1992).

55 F. Schmidt-Kaler, J. Eschner, G. Morigi, C. Roos, D. Leibfried, A. Mundt and R. Blatt:
'Laser cooling with electromagnetically induced transparency: application to trapped samples of ions or neutral atoms',
Applied Physics B **73**, 807–814 (2001).

56 D. J. Wineland, J. Dalibard and C. Cohen-Tannoudji:
'Sisyphus cooling of a bound atom',
JOSA B **9**, 32–42 (1992).

57 C. Monroe, D. Meekhof, B. King, S. R. Jefferts, W. M. Itano, D. J. Wineland and P. Gould:
'Resolved-sideband raman cooling of a bound atom to the 3d zero-point energy',
Physical review letters **75**, 4011 (1995).

58 J. Eschner, G. Morigi, F. Schmidt-Kaler and R. Blatt:
'Laser cooling of trapped ions',
JOSA B **20**, 1003–1015 (2003).

59 D. Leibfried, D. Meekhof, B. King, C. Monroe, W. M. Itano and D. J. Wineland:
'Experimental determination of the motional quantum state of a trapped atom',
Phys. Rev. Lett. **77**, 4281 (1996).

60 P. Zeeman:
'Xxxii. on the influence of magnetism on the nature of the light emitted by a substance',
The London, Edinburgh, and Dublin Philosophical Magazine and Journal of Science **43**, 226–239 (1897).

61 A. Landé:
'Über den anomalen zeemaneffekt (teil i)',
Zeitschrift für Physik **5**, 231–241 (1921).

62 C. Hempel:
'Digital quantum simulation, schrödinger cat state spectroscopy and setting up a linear ion trap',
PhD thesis (2014).

63 P. Müller and J. Eschner:
'Single calcium-40 ion as quantum memory for photon polarization: a case study',
Applied Physics B **114**, 10.1007/s00340-013-5681-1 (2013).

64 D. F. James:
Quantum dynamics of cold trapped ions with application to quantum computation,
tech. rep. (1997).

65 F. M. Leupold:
'Bang-bang control of a trapped-ion oscillator',
PhD thesis (ETH Zurich, 2015).

66 R. Bonifacio, S. Olivares, P. Tombesi and D. Vitali:
'Model-independent approach to nondissipative decoherence',
Physical Review A **61**, 053802 (2000).

68 L. Davidovich:
'Sub-poissonian processes in quantum optics',
Reviews of Modern Physics **68**, 127 (1996).

69 U. Chabaud, D. Markham and F. Grosshans:
'Stellar representation of non-gaussian quantum states',
Physical Review Letters **124**, 063605 (2020).

70 U. Fano:
'Ionization yield of radiations. ii. the fluctuations of the number of ions',
Physical Review **72**, 26 (1947).

71 D. Klyshko:
'Observable signs of nonclassical light',
Physics Letters A **213**, 7–15 (1996).

72 J. K. Asbóth, J. Calsamiglia and H. Ritsch:
'Computable measure of nonclassicality for light',
Physical Review Letters **94**, 173602 (2005).

73 G. Vidal and R. F. Werner:
'Computable measure of entanglement',
Phys. Rev. A **65**, 032314 (2002).

74 W. Vogel and J. Sperling:
'Unified quantification of nonclassicality and entanglement',
Physical Review A **89**, 052302 (2014).

75 C. T. Lee:
'Measure of the nonclassicality of nonclassical states',
Physical Review A **44**, R2775 (1991).

76 C. Gehrke, J. Sperling and W. Vogel:
'Quantification of nonclassicality',
Physical Review A **86**, 052118 (2012).

77 M. B. Plenio:
'Logarithmic negativity: a full entanglement monotone that is not convex',
Physical review letters **95**, 090503 (2005).

78 G. Araneda:
'Experiments with single photons emitted by single atoms',
PhD thesis (2019).

79 P. Obšil, A. Lešundák, T. Pham, G. Araneda, M. Čížek, O. Číp, R. Filip and L. Slodička:
'Multipath interference from large trapped ion chains',
New Journal of Physics **21**, 093039 (2019).

80 P. Obšil, L. Lachman, T. Pham, A. Lešundák, V. Hucl, M. Čížek, J. Hrabina, O. Číp, L. Slodička and R. Filip:
'Nonclassical light from large ensembles of trapped ions',
Physical review letters **120**, 253602 (2018).

81 D. Berkeland, J. Miller, J. C. Bergquist, W. M. Itano and D. J. Wineland:
'Minimization of ion micromotion in a paul trap',
Journal of applied physics **83**, 5025–5033 (1998).

82 N. Herschbach, K. Pyka, J. Keller and T. E. Mehlstäubler:
'Linear paul trap design for an optical clock with coulomb crystals',
Applied Physics B **107**, 891–906 (2012).

83 L. A. Zhukas, M. J. Millican, P. Svihra, A. Nomerotski and B. B. Blinov:
'Direct observation of ion micromotion in a linear paul trap',
Physical Review A **103**, 023105 (2021).

84 J. Keller, H. Partner, T. Burgermeister and T. Mehlstäubler:
'Precise determination of micromotion for trapped-ion optical clocks',
Journal of Applied Physics **118**, 104501 (2015).

85 R. H. Brown and R. Q. Twiss:
'Lxxiv. a new type of interferometer for use in radio astronomy',
The London, Edinburgh, and Dublin Philosophical Magazine and Journal of Science **45**, 663–682 (1954).

86 G. Cerchiari, G. Araneda, L. Podhora, L. Slodička, Y. Colombe and R. Blatt:
'Measuring ion oscillations at the quantum level with fluorescence light',
Physical Review Letters **127**, 063603 (2021).

87 G. Cerchiari, L. Dania, D. Bykov, R. Blatt and T. Northup:
'Position measurement of a dipolar scatterer via self-homodyne detection',
Physical Review A **104**, 053523 (2021).

88 T. Sauter, W. Neuhauser, R. Blatt and P. Toschek:
'Observation of quantum jumps',
Physical review letters **57**, 1696 (1986).

89 D. Wineland and H. Dehmelt:
'Proposed 1014$\delta\nu/\nu$ laser fluorescence spectroscopy on tl+ mono-ion oscillator iii (side band cooling)',
Bull. Am. Phys. Soc **20**, 637–637 (1975).

90 C. Roos, T. Zeiger, H. Rohde, H. Nägerl, J. Eschner, D. Leibfried, F. Schmidt-Kaler and R. Blatt:
'Quantum state engineering on an optical transition and decoherence in a paul trap',
Phys. Rev. Lett. **83**, 4713 (1999).

91 G. Morigi, J. Eschner and C. H. Keitel:
'Ground state laser cooling using electromagnetically induced transparency',
Physical review letters **85**, 4458 (2000).

92 A. Ritboon, L. Slodička and R. Filip:
'Sequential phonon measurements of atomic motion',
Quantum Science and Technology **7**, 015023 (2022).

93 F. Diedrich, J. Bergquist, W. M. Itano and D. Wineland:
'Laser cooling to the zero-point energy of motion',
Physical review letters **62**, 403 (1989).

94 B. Srivathsan, M. Fischer, L. Alber, M. Weber, M. Sondermann and G. Leuchs:
'Measuring the temperature and heating rate of a single ion by imaging',
New Journal of Physics **21**, 113014 (2019).

95 K. Vahala, M. Herrmann, S. Knünz, V. Batteiger, G. Saathoff, T. Hänsch and T. Udem:
'A phonon laser',
Nature Physics **5**, 682–686 (2009).

96 R. Blatt, J. Cirac and P. Zoller:
'Trapping states of motion with cold ions',
Physical Review A **52**, 518 (1995).

97 D. Kienzler, H.-Y. Lo, V. Negnevitsky, C. Flühmann, M. Marinelli and J. P. Home:
'Quantum harmonic oscillator state control in a squeezed fock basis',
Phys. Rev. Lett. **119**, 033602 (2017).

98 Q. A. Turchette, B. King, D. Leibfried, D. Meekhof, C. Myatt, M. Rowe, C. Sackett, C. Wood, W. Itano, C. Monroe et al.:
'Heating of trapped ions from the quantum ground state',
Physical Review A **61**, 063418 (2000).

99 J. Řeháček, Z. Hradil and M. Ježek:
'Iterative algorithm for reconstruction of entangled states',
Physical Review A **63**, 040303 (2001).

100 S. Schneider and G. J. Milburn:
'Decoherence in ion traps due to laser intensity and phase fluctuations',
Phys. Rev. A **57**, 3748 (1998).

101 M. Murao and P. Knight:
'Decoherence in nonclassical motional states of a trapped ion',
Phys. Rev. A **58**, 663 (1998).

102 A. Budini, R. de Matos Filho and N. Zagury:
'Localization and dispersivelike decoherence in vibronic states of a trapped ion',
Phys. Rev. A **65**, 041402 (2002).

103 S. Fujiwara and S. Hasegawa:
'Estimation of the heating rate of ions due to laser fluctuations when implementing quantum algorithms',
Quantum Information & Computation **7**, 573–583 (2007).

104 L. Lachman:
'Advanced identification of quantum properties of the light',
Ph. D. Thesis (2020).

105 D. Meekhof, C. Monroe, B. King, W. M. Itano and D. J. Wineland:
'Generation of nonclassical motional states of a trapped atom',
Phys. Rev. Lett. **76**, 1796 (1996).

106 K. Toyoda, R. Hiji, A. Noguchi and S. Urabe:
'Hong–ou–mandel interference of two phonons in trapped ions',
Nature **527**, 74 (2015).

107 S. Ding, G. Maslennikov, R. Hablützel, H. Loh and D. Matsukevich:
'Quantum parametric oscillator with trapped ions',
Phys. Rev. Lett. **119**, 150404 (2017).

108 J. Zhang, M. Um, D. Lv, J.-N. Zhang, L.-M. Duan and K. Kim:
'Noon states of nine quantized vibrations in two radial modes of a trapped ion',
Phys. Rev. Lett. **121**, 160502 (2018).

109 Y. Chu, P. Kharel, T. Yoon, L. Frunzio, P. T. Rakich and R. J. Schoelkopf:
'Creation and control of multi-phonon fock states in a bulk acoustic-wave resonator',
Nature **563**, 666–670 (2018).

110 K. Duivenvoorden, B. M. Terhal and D. Weigand:
'Single-mode displacement sensor',
Physical Review A **95**, 012305 (2017).

111 M. Brownnutt, M. Kumph, P. Rabl and R. Blatt:
'Ion-trap measurements of electric-field noise near surfaces',
Rev. Mod. Phys. **87**, 1419 (2015).

112 B. De Neeve, T.-L. Nguyen, T. Behrle and J. P. Home:
'Error correction of a logical grid state qubit by dissipative pumping',
Nature Physics **18**, 296–300 (2022).

113 I. Straka, A. Predojević, T. Huber, L. Lachman, L. Butschek, M. Miková, M. Mičuda, G. S. Solomon, G. Weihs, M. Ježek and R. Filip:
'Quantum non-gaussian depth of single-photon states',
Phys. Rev. Lett. **113**, 223603 (2014).

114 Y. Wan, F. Gebert, J. B. Wübbena, N. Scharnhorst, S. Amairi, I. D. Leroux, B. Hemmerling, N. Lörch, K. Hammerer and P. O. Schmidt:
'Precision spectroscopy by photon-recoil signal amplification',
Nat. Commun. **5**, 1–6 (2014).

115 L. Slodička, P. Marek and R. Filip:
'Deterministic nonclassicality from thermal states',
Optics express **24**, 7858–7870 (2016).

116 P. Marek, L. Lachman, L. Slodička and R. Filip:
'Deterministic nonclassicality for quantum-mechanical oscillators in thermal states',
Physical Review A **94**, 013850 (2016).

117 C. Hempel, B. Lanyon, P. Jurcevic, R. Gerritsma, R. Blatt and C. Roos:
'Entanglement-enhanced detection of single-photon scattering events',
Nature Photonics **7**, 630–633 (2013).

118 M. F. Gely, M. Kounalakis, C. Dickel, J. Dalle, R. Vatré, B. Baker, M. D. Jenkins and G. A. Steele:
'Observation and stabilization of photonic fock states in a hot radio-frequency resonator',
Science **363**, 1072–1075 (2019).

119 D. Gelbwaser-Klimovsky and G. Kurizki:
'Work extraction from heat-powered quantized optomechanical setups',
Scientific reports **5**, 1–6 (2015).

120 W. Gorecki, S. Zhou, L. Jiang and R. Demkowicz-Dobrzański:
'Optimal probes and error-correction schemes in multi-parameter quantum metrology',
Quantum **4**, 288 (2020).

121 A. Kubica and R. Demkowicz-Dobrzański:
'Using quantum metrological bounds in quantum error correction: a simple proof of the approximate eastin-knill theorem',
Physical Review Letters **126**, 150503 (2021).

122 D. Berry and A. Lvovsky:
'Linear-optical processing cannot increase photon efficiency',
Physical review letters **105**, 203601 (2010).

123 D. A. Golter, T. Oo, M. Amezcua, K. A. Stewart and H. Wang:
'Optomechanical quantum control of a nitrogen-vacancy center in diamond',
Physical review letters **116**, 143602 (2016).

124 Y.-I. Sohn, S. Meesala, B. Pingault, H. A. Atikian, J. Holzgrafe, M. Gündoğan, C. Stavrakas, M. J. Stanley, A. Sipahigil, J. Choi et al.:
'Controlling the coherence of a diamond spin qubit through its strain environment',
Nature communications **9**, 1–6 (2018).

125 J. Gieseler, A. Kabcenell, E. Rosenfeld, J. Schaefer, A. Safira, M. J. Schuetz, C. Gonzalez-Ballestero, C. C. Rusconi, O. Romero-Isart and M. D. Lukin:
'Single-spin magnetomechanics with levitated micromagnets',
Physical review letters **124**, 163604 (2020).